DEVELOPMENT OF MONOLITHIC ACTIVE PIXEL SENSORS (MAPS) DETECTOR FOR TRACK RECONSTRUCTION IN PROTON COMPUTED TOMOGRAPHY

ARNON SONGMOOLNAK

A Thesis Submitted in Partial Fulfillment of the Requirements for the
Degree of Doctor of Philosophy in Physics
Suranaree University of Technology
Academic Year 2022

การพัฒนาหัววัดอนุภาคแบบ Monolithic Active Pixel Sensors (MAPS) สำหรับการหาเส้นทางในเครื่องสร้างภาพตัดขวางจากโปรตอนโดยอาศัยคอมพิวเตอร์

นายอานนท์ สงมูลนาค

วิทยานิพนธ์นี้เป็นส่วนหนึ่งของการศึกษาตามหลักสูตรปริญญาวิทยาศาสตรดุษฎีบัณฑิต
สาขาวิชาฟิสิกส์
มหาวิทยาลัยเทคโนโลยีสุรนารี
ปีการศึกษา 2565

DEVELOPMENT OF MONOLITHIC ACTIVE PIXEL SENSORS (MAPS) DETECTOR FOR APPLICATIONS IN PROTON COMPUTED TOMOGRAPHY

Suranaree University of Technology has approved this thesis submitted in partial fulfillment of the requirements for the Degree of Doctor of Philosophy.

Thesis Examining Committee

____
(Assoc. Prof. Dr. Panomsak Meemon)
Chairperson

____
(Asst. Prof. Dr. Chinorat Kobdaj)
Member (Thesis Advisor)

____
(Dr. Kritsada Kittimanapun)
Member

____
(Asst. Prof. Dr. Christoph Herold)
Member

____
(Dr. Wanchaloem Poonsawat)
Member

____
(Assoc. Prof. Dr. Yupaporn Ruksakulpiwat)
Vice Rector for Academic Affairs
and Quality Assurance

____
(Prof. Dr. Santi Maensiri)
Dean of Institute of Science

อานนท์ สงมูลนาค : การพัฒนาหัววัดอนุภาคแบบ Monolithic Active Pixel Sensors (MAPS) เพื่อประยุกต์ใช้ในเครื่องสร้างภาพตัดขวางจากโปรตอนโดยอาศัยคอมพิวเตอร์ (DEVELOPMENT OF MONOLITHIC ACTIVE PIXEL SENSORS (MAPS) DETECTOR FOR APPLICATIONS IN PROTON COMPUTED TOMOGRAPHY). อาจารย์ที่ปรึกษา : ผู้ช่วยศาสตราจารย์ ดร.ชิโนรัตน์ กอบเดช, 105 หน้า.

คำสำคัญ: หัววัดอนุภาค/ เครื่องสร้างภาพตัดขวาง/ ลำอนุภาคโปรตอน/ การหาเส้นทางอนุภาค

เครื่องสร้างภาพตัดขวางจากโปรตอนด้วยคอมพิวเตอร์เป็นเครื่องมือสร้างภาพ 3 มิติทางการแพทย์ เพื่อใช้ในการวินิจฉัยผู้ป่วยเพื่อเตรียมเข้ารับการรักษาด้วยโปรตอน ในการถ่ายภาพรายละเอียดของผู้ป่วยด้วยวิธีนี้ ความถูกต้องในการวัดเส้นทางและพลังงานของอนุภาคโปรตอนเป็นสิ่งสำคัญอย่างมาก ในงานวิจัยนี้ โปรแกรม GATE ที่เป็นโปรแกรมสำหรับการจำลองแบบวิธีมอนติคาร์โล ซึ่งสร้างมาจากชุดเครื่องมือของโปรแกรม GEATN4 ถูกใช้เพื่อจำลองการทดลองหัววัดอนุภาคเพื่อเตรียมการสำหรับการสร้างเครื่องมือทดลอง จากผลลัพธ์ของความถูกต้องของเส้นทางอนุภาคที่คำนวณได้พบว่ามีค่าลดลงเมื่อเพิ่มจำนวนของอนุภาคปฐมภูมิ ดังนั้นการจำลองจึงบ่งบอกได้ว่าความเข้มข้นของแหล่งกำเนิดอนุภาคที่มีปริมาณน้อยมีความเหมาะสมกับเครื่องทดลองสร้างภาพตัดขวางจากโปรตอนด้วยคอมพิวเตอร์ อย่างไรก็ตาม ลำอนุภาคโปรตอนที่ใช้ในการรักษาผู้ป่วยเพื่อกำจัดเซลล์มะเร็งนั้นมีความเข้มข้นสูงถึง 1 พันล้านอนุภาคต่อวินาที เพื่อที่จะให้หัววัดโปรตอนวัดสัญญาณของโปรตอนจำนวนขนาดนี้ได้นั้น หัววัดต้องมีความเร็วมากพอ ในการทดลองนี้ FPGA trigger สร้างสัญญาณเพื่อส่งไปยังหัววัดผ่านทาง DAQ บอร์ดแผ่นแรก สัญญาณความถี่ที่ใช้ให้ถูกตั้งไว้ที่ 9.5 กิโลเฮิรตซ์ เพื่อใช้ขีดสุดของอัตราการอ่านของหัววัด โดยที่แหล่งกำเนิดโปรตอนที่ใช้คือระบบ ProBeam™ ตั้งอยู่ที่โรงพยาบาลจุฬาลงกรณ์ สภากาชาดไทย กรุงเทพมหานคร ประเทศไทย และแท่งอะคริลิค collimator ถูกใช้เพื่อลดจำนวนอนุภาคโปรตอน สัญญาณพื้นหลังและสัญญาณรบกวนถูกวัดในระบบห้องมืด อนุภาคที่ถูกวัดได้ในบริเวณพื้นที่ 2 ซิกมา ซึ่งเป็นบริเวณที่ถูกคำนวณด้วยการแจกแจงแบบเกาส์เซียน จะถูกนำมาวิเคราะห์เพื่อหาเส้นทางของอนุภาคนั้น ๆ ในงานวิจัยนี้ค่าพลังงานของแหล่งกำเนิดโปรตอนถูกใช้ที่ 70 เมกะอิเล็กตรอนโวลต์ สำหรับค่าพลังงานต่ำสุดของเครื่องให้กำเนิดโปรตอน และ 200 เมกะอิเล็กตรอนโวลต์ ซึ่งเป็นค่าที่เหมาะสมกับเครื่องสร้างภาพตัดขวางจากโปรตอนด้วยคอมพิวเตอร์ ถูกเลือกใช้ในการคำนวณหาเส้นทางของอนุภาคโปรตอน โดยจากผลการทดลองพบว่าในช่วงพลังงานทั้งคู่มีค่าความถูกต้องในการหาเส้นทางประมาณร้อยละ 70 และยังแสดงให้เห็นได้อีกว่า การทดลองของหัววัดอนุภาคแบบ MAPS นี้ สามารถนำไปพัฒนาเป็นเครื่องต้นแบบของเครื่องสร้างภาพตัดขวางจากโปรตอนด้วยคอมพิวเตอร์ได้

สาขาวิชาฟิสิกส์ ลายมือชื่อนักศึกษา ____________

ปีการศึกษา 2565 ลายมือชื่ออาจารย์ที่ปรึกษา ชิโนรัตน์ กอบเดช

ARNON SONGMOOLNAK : DEVELOPMENT OF MONOLITHIC ACTIVE PIXEL SENSORS (MAPS) DETECTOR FOR APPLICATIONS IN PROTON COMPUTED TOMOGRAPHY. THESIS ADVISOR : ASST. PROF. CHINORAT KOBDAJ, Ph.D. 105 PP.

Keyword: telescope/ computed tomography/ proton beam/ track reconstruction

Proton computed tomography (pCT) is a three-dimensional medical imaging device used for diagnosing patients prior to proton therapy. Accurate tracking of proton paths and measuring their energy are crucial for reconstructing detailed diagnostic images. In this work, the Gate software, which is the Monte Carlo (MC) simulation and built from the GEANT4 toolkit, was used to model the telescope simulation and achieve the experimental construction. The correctness of reconstructed tracks in the simulation is decreased by increasing number of primaries. So, the simulation suggests that a low-intensity particle source is suitable for a pCT experiment. However, proton beam therapy, which delivers a precise beam of protons to destroy tumor cells, typically operates at a beam rate of around 10^9 protons/s. For identifying proton tracks from this pencil beam, the readout system of a proton detector must be fast enough to distinguish proton hit signals because of high beam rate. In this experiment, a field-programmable gate array (FPGA) trigger generated 9.5 kHz of trigger frequency to the telescope through the first data acquisition (DAQ) board. The proton beam scanning (PBS) from the ProBeam™ system at King Chulalongkorn Memorial Hospital (KCMH) in Bangkok, Thailand, served as the proton source, and an acrylic collimator was used to reduce the number of protons in the treatment beam. Background and noise were measured in the dark test for noise removal in detected signal. Track analysis was done on activated pixels within a 2-sigma area of a Gaussian beam model to find possible tracks in the apertured part. The study investigated the lowest treatment beam at 70 MeV and the transmission beam for pCT imaging at 200 MeV. In both cases, approximately 70% of the tracks were successfully completed. The experimental reconstruction results demonstrate the feasibility of developing the monolithic active pixel sensor (MAPS) telescope as a pCT prototype.

School of Physics

Academic Year 2022

Student's Signature ____________

Advisor's Signature C. Kobdaj

ACKNOWLEDGEMENTS

I have a passion for understanding how computers work and communicating with them through coding and programming languages. During my bachelor's studies, I focused on material analysis of Hard Disk Drives (HDDs). Upon completing my bachelor's degree, I desired to further explore semiconductor devices such as Random Access Memory (RAM) and Solid State Drives (SSDs). This led me to pursue a doctoral degree at Suranaree University of Technology (SUT) with a scholarship from the Development and Promotion of Science and Technology Talents Project (DPST) as a physicist. During the first year of my Ph.D., I didn't join any specific research group within the School of Physics as I wanted to explore various research fields to find the best fit for my interests. In my second year, my friend Thanachot Nasawad, who was conducting research for his master's degree in the Nuclear and Particle Physics group, informed me about their semiconductor development project for particle detection devices. Eventually, I became a member of the Nuclear and Particle Physics group. In 2016, I spent six months at the Thai Microelectronics Center (TMEC) in Chachoengsao, studying Technology Aid Design (TCAD), a commercial software used for semiconductor device simulation. My work focused on simulating gamma ray sensors for particle sensor development. After returning from TMEC, I joined the A Large Ion Collider Experiment (ALICE) at the European Organization for Nuclear Research (CERN). As an ALICE member, I had the opportunity to attend workshops on ALICE ITS Upgrade, MFT, and O2 Asia, where I was inspired by Dieter Röhrich's presentation on proton computed tomography using ALPIDE sensors. This innovative use of semiconductor devices in clinical research caught my attention, and I discussed the possibility of studying their work at the University of Bergen (UiB) with Professor Röhrich during the workshop. In 2020, I spent six months in Bergen as part of the pCT group, programming C++ code to communicate with Xilinx VCU118 FPGA via Transmission Control Protocol (TCP). The VCU118 board was used for reading/writing ALPIDE data and interfacing with the user. Additionally, I formed a pCT research team at SUT with the aim of replicating the pCT experiment conducted by the Bergen team. However, due to the challenges posed by COVID-19 and the situation in Ukraine, we encountered difficulties in procuring ALPIDE sensors for the pCT prototype. As an alternative, we decided to utilize a telescope consisting of six ALPIDEs for pCT development and test it with treatment proton beams at King Chulalongkorn Memorial Hospital in Thailand.

I’d like to thank TMEC for my TCAD studies. I’d like to thank CERN for including me as an ALICE member. I’d like to thank Professor Dieter Röhrich for inspiring me to work on the pCT project. I’d want to thank the pCT Bergen team for including me in their group. I’d like to thank Asst. Prof. Dr. Christoph Herold for his assistance in designing the track reconstruction algorithm. I would also want to thank Dr. Narongrit Ritjoho, Dr. Phongnared Boontueng, Mr. Passakorn Phumara, Mr. Lattawat Charoonratana, Mr. Natthawut LaoJamnongwong, and Miss. Yaowaluk Buanill from the pCT SUT team.

I would like to thank the Development and Promotion of Science and Technology Talents Scholarship (DPST) and the Thailand Center of Excellence in Physics (ThEP-61-PHM-SUT4) for their financial assistance. I’d like to thank King Chulalongkorn Memorial Hospital in Thailand for providing us with the proton source. I’d like to thank KCMH members, especially Assistant Professor Dr. Taweap Sanghangthum, for operating a proton beam line and allocating beam time. As my advisor and co-adviser, I would like to thank Asst. Prof. Dr. Chinorat Kobdaj and Dr. Todsaporn Fuangrod for guiding me on how to complete this study. I’d like to thank Suranaree University of Technology (SUT) for their assistance with this research.

I’d want to express my gratitude to my family for their encouragement and assistance in obtaining my Ph.D. My parents’ success in their careers has pushed me to work hard in my Ph.D. program. I’d like to thank my colleagues from SUT’s Nuclear and Particle Physics Group for their assistance with my experiments. Finally, I am tremendously proud of myself for finishing my Ph.D. By the way, I believe I need to improve in order to be an excellent researcher in the future.

Arnon Songmoolnak

CONTENTS

CONTENTS (Continued)

CONTENTS (Continued)

CONTENTS (Continued)

LIST OF TABLES

LIST OF FIGURES

LIST OF FIGURES (Continued)

LIST OF FIGURES (Continued)

LIST OF FIGURES (Continued)

LIST OF FIGURES (Continued)

LIST OF FIGURES (Continued)

LIST OF FIGURES (Continued)

LIST OF FIGURES (Continued)

LIST OF FIGURES (Continued)

LIST OF FIGURES (Continued)

Figure **Page**

LIST OF FIGURES (Continued)

LIST OF ABBREVIATIONS

pCT	Proton Computed Tomography
PT	Proton Therapy
CT	Computed therapy
DTC	Digital Tracking Calorimeter
PSD	Positioned Sensitive Detector
RED	Residual Energy Detector
YAG:Ce	Yttrium aluminum garnet activated by cerium
NaI(Tl)	Thallium-activated sodium iodide
CsI(Tl)	Thallium-activated cesium iodide
Si strip	Silicon Strip Detector
Sci Fi	Scintillating Fiber
MAPS	Monolithic Active Pixel Sensor
ALPIDE	ALICE Pixel Detector
ALICE	A Large Ion Collider Experiment
ITS	Inner Tracking System
KCMH	King Chulalongkorn Memorial Hospital
FPGA	Field-programmable gate array
MeV	Mega Electron Volt
MC	Monte Carlo
CMOS	Complementary Metal Oxide Semiconductor
PBS	Pencil Beam Scanning
PDG	Particle Data Group
DAQ	Data Acquisition
QA	Quality Assurance
MU	Monitor Unit
GUI	Graphical User Interface

CHAPTER I
INTRODUCTION

Particle therapy refers to the medical application of ion beams, either protons or heavier ions, to treat individuals with either cancerous or noncancerous tumors. It is considered the most advanced type of radiotherapy. Although it may be slightly more expensive compared to traditional X-rays, ion beam therapy offers a great chance for significant advancements in the treatment and study of cancer. Over the past ten years, more than 20 clinical centers have been established in European countries, providing easier access to this cutting-edge therapy for European patients. Since 1952, over 190,000 patients have received proton therapy, while 28,000 have been treated with carbon ions (www.ptcog.ch). Currently, there are 80 proton therapy centers worldwide, about 30% of those located in Europe. The number of European proton therapy clinics is rapidly growing, with 15 operational facilities in 2017 and expected 31 proton therapy centers in clinical operation by the end of 2020 (Figure 1.1).

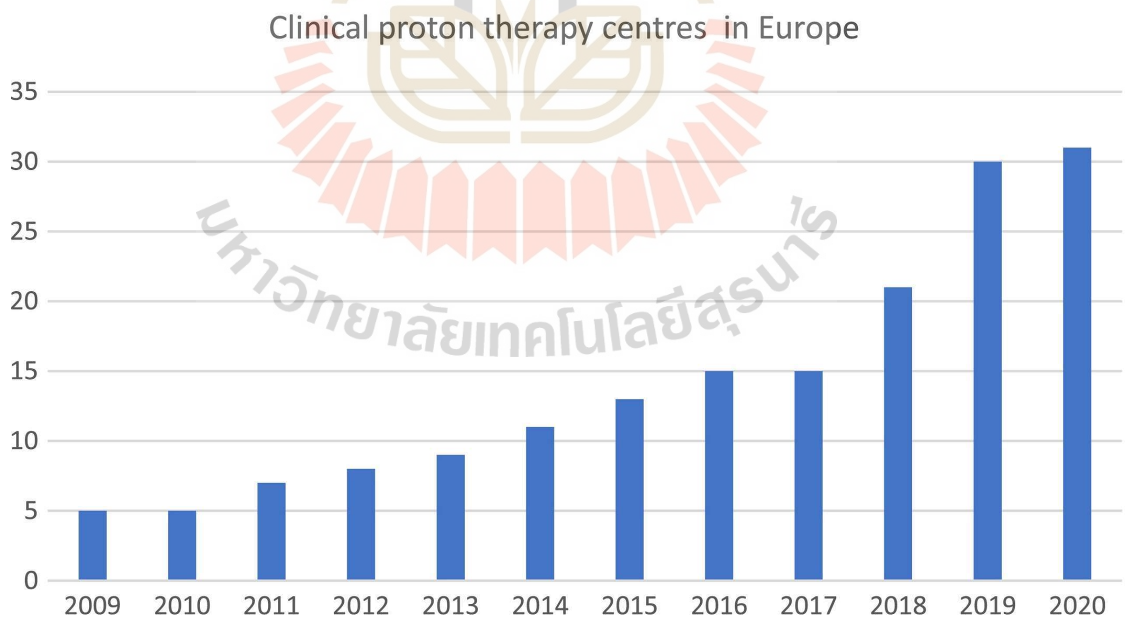

Figure 1.1 The number of clinical proton therapy centers in Europe 2009–2020. Source: www.ptcog.ch.

Proton therapy uses positive charged particles or protons to treat tumor cells. This has an advantage over using X-ray beam since it is possible to spare the surrounding tissues near the tumor cells due to the Bragg peak. X-ray Computed Tomography (CT) is still used in proton treatment centers to find tumor cells and figure out how much radiation to give. For the real treatment with a proton beam, the doctor and the medical physicist in charge of planning the treatment have to change the shape of the x-ray CT unit into the shape of the proton unit. This conversion causes uncertainty in the tumor position due to systematic errors. Using the proton beam for CT instead of X-ray can minimize this systematic error issue and help doctors to connect with the proton treatment planning by enabling tumor position verification directly (Schulte et al., 2005a). The solution of measuring and reconstructing the proton RSP distribution have been proposed with more precise in coversion technique (Schneider et al., 1996).

In 1976, Cormack and Koehler construct the prototype of Proton Computed Tomography (pCT) for testing at the Harvard Cyclotron Laboratory (Cormack and Koehler, 1976). A scintillator is mounted on a photomultiplier to detect residual energy from collimated proton beam at 158 MeV of energy. A two-dimensional (2D) tracking system can be included in the prototype to determine proton direction from the pre- and post-patient (Schulte et al., 2004).

The aim of this work is to develop a Monolithic Active Pixel Sensors (MAPS) telescope with proton beam at King Chulalongkorn Memorial Hospital (KCMH) to establish the position-sesitive detector (PSD) for pCT. Monte Carlo simulations and experimental data are used to reconstruct to be proton tracks. According to the high intensity of the operational beam, the number of protons from KCMH cyclotron source is reduced by collimator and Polymethyl Methacrylate (PMMA) degrader. The track following algorithm is applied to find the proton trajectory in 6 ALPIDE sensors as stacked layers. The result shows that the telescope can be constructed as tracker and MAPS telescope can be developed as part of a pCT prototype.

CHAPTER II
RESEARCH BACKGROUND

2.1 Concept and design of proton computed tomography

Proton therapy uses positively charged protons to treat tumor cells. This has the advantage over using X-ray beams since it is possible to spare the surrounding tissues near tumor cells due to the Bragg peak (see figure 2.1). In the existing proton treatment centers, X-ray computed tomography (CT) is still being used for locating tumor cells and performing dose calculations. But when it comes to the real treatment using the proton beam, the doctor and the medical physicist, who are responsible for the treatment planning, have to convert the formation obtained from the X-ray CT unit into the corresponding proton unit. This conversion causes uncertainty in the tumor's position due to systematic errors. Using the proton beam for CT instead of X-rays can reduce this systematic issue and help doctors better connect with proton treatment planning by directly verifying tumor position verification (Schulte et al., 2005b).

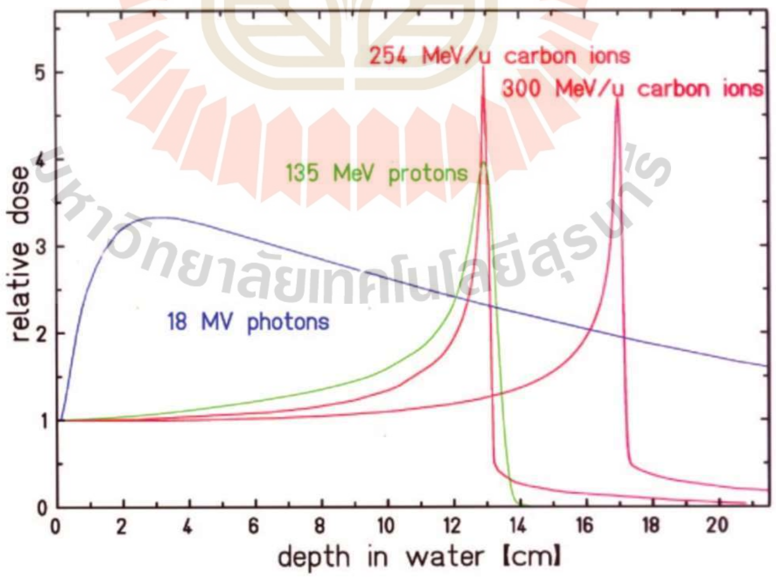

Figure 2.1 Depth-dose profiles of radiotherapy beams like photons, protons, and carbon ions (Weber et al., 2009).

The pCT system, which is the main focus of this thesis, was first described by Schulte et al. in 2004 (Schulte et al., 2004). Originally designed for high-energy physics, the detector system features two 2D silicon tracking modules situated before and after the patient, which enables the system to measure the positions and directions of individual protons both before and after passing through the patient. In the initial models, each tracking module was composed of orthogonally-oriented, single-sided silicon strip detectors. The residual energy detector, located after the tracking modules, was a segmented scintillation crystal calorimeter, with each crystal individually wrapped and coupled with a silicon photodiode. Figure 2.2 illustrates the head imaging system.

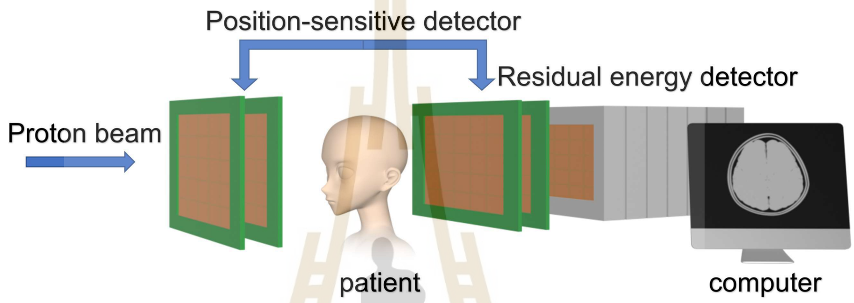

Figure 2.2 The design of the proton computed tomography system is shown in a conceptual manner. The system includes two 2D sensitive proton tracking modules placed before and after the patient, and a segmented crystal calorimeter that records residual energy.

2.1.1 Position-sensitive detector

In pCT, protons are used to create images of the internal structure of the body by measuring the energy deposited by the protons as they pass through the patient's tissue. Position-sensitive detector (PSDs) are placed upstream and downstream of the patient to measure the position and direction of the protons before and after passing through the patient, allowing for more accurate reconstruction of the patient's internal structure.

Silicon pixel sensors can be used for tracking the trajectory of a proton in the incident proton direction before and after entering a patient. The sensors should have a large active area with a sub-mm pixel size, a fast frame rate, and a multiple-bit signal depth. Moreover, their read-out electronics should be able to resolve multiple protons in a single image frame. To meet the above requirements, image sensors such as the Complementary Metal Oxide Semiconductor (CMOS) (Poludniowski et al., 2014) and the charge-coupled devices (CCDs) are being considered as suitable candidates.

The Monolithic Active Pixel Sensors (MAPS) named ALPIDE which is described in Section 2.4 appeared in the Digital Tracking Calorimeter Prototype of pCT Bergen collaboration(Alme et al., 2020). The 50 μm ALPIDEs were used for being PSD part. The tracker layers are constructed by mounting nine ALPIDEs per flex cable called a string. The size of a sensitive layer area is 27 cm × 15 cm which consists of twelve strings in two half layers as shown in Figure 2.3.

2.1.2 Residual energy detector

A Residual Energy Detector (RED) is a particle detector used in proton computed tomography (pCT) to estimate the energy of protons that escape the body after passing through tissue. The RED is located downstream of the pCT system's particle tracking component, which detects the position and direction of individual protons before and after the patient. Protons lose energy as they transit through the patient's body and deposit part of it in the tissue. The RED monitors the leftover energy of protons as they leave the patient's body, which is then used to rebuild the proton's starting energy and quantify tissue density along the proton's journey. The RED is typically made up of a segmented scintillation crystal calorimeter, with each crystal separately wrapped and connected to a silicon photodiode. The use of RED is critical in pCT because it allows the machine to assess the stopping power of protons flowing through tissue, which is critical for correct image reconstruction.

PSDs are used in combination with other types of detectors, such as residual energy detectors, to measure the energy of the protons before and after passing through the patient. The combination of these detectors allows for the reconstruction of high-resolution, three-dimensional images of the patient's internal structure, which can be used for diagnosis and treatment planning in radiation therapy.

The absorber layers and 100 μm ALPIDEs were used to construct the calorimeter layers of the Digital Tracking Calorimeter (DTC) for proton residual energy detection. The absorber material is aluminum (Al 99.5), which is a commercial alloy with an aluminum content greater than 99%. The calorimeter has 41 layers, each of which is made up of several elements. As shown in Figure 2.3, a single layer consists of 1mm thick aluminum carriers, a half layer of sensors not directly facing the proton beam, a 2mm air gap maintained by 2mm thick aluminum spacers, a half layer of sensors facing the proton beam, 1mm thick aluminum carriers that support the sensors, and a 1.5mm thick aluminum absorber plate (Alme et al., 2020) as shown in Figure 2.3.

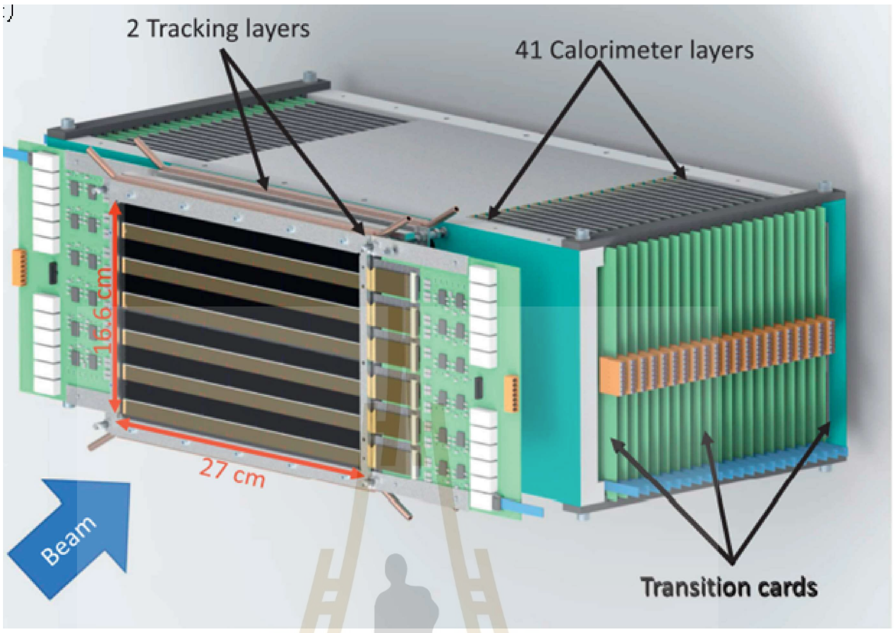

Figure 2.3 The Digital Tracking Calorimeter (DTC) device which is designed by Bergen pCT collaboration. The 50 μm ALPIDEs are mounted as tracking layers and 100 μm ALPIDEs combined with absorbing material act as calorimeter (Alme et al., 2020).

2.1.3 Image reconstruction

The detector system employed in this pCT contains two distinct components: one for particle tracking and the other for residual energy measurement. As a result, the process of creating an image will be divided into two parts. The utilization of individual protons to rebuild the image is a major aspect of this pCT method. This means that the image space line integrals correspond to the trajectories of individual protons, which are approximated using data from silicon tracking modules. While straight line routes are useful for simple and quick reconstructions, earlier pCT experiments have demonstrated that they reduce spatial resolution (Cormack and Koehler, 1976; Hanson, 1979; Hanson et al., 1981; Hanson et al., 1982; Zygmanski et al., 2000). Alternatively, the measured entry and departure directions of the protons and a cubic spline approximation of the proton path can be used.

Although the most likely path (MLP) technique provides superior accuracy in predicting the path of protons (Li et al., 2006), it does not account for the physical characteristics on which multiple Coulomb scattering (MCS) depends. The MLP method is currently the most precise method available (Schneider and Pedroni, 1994; Williams, 2004; Schulte et al., 2008). This method takes into account the energy loss of protons as they pass through an object and integrates material-specific factors into the MCS simulation. As a result, a mathematical formula that calculates the lateral displacement and angular divergence of the highest probability at any given depth in the patient using just the exterior measurements gathered by the silicon tracking modules is obtained.

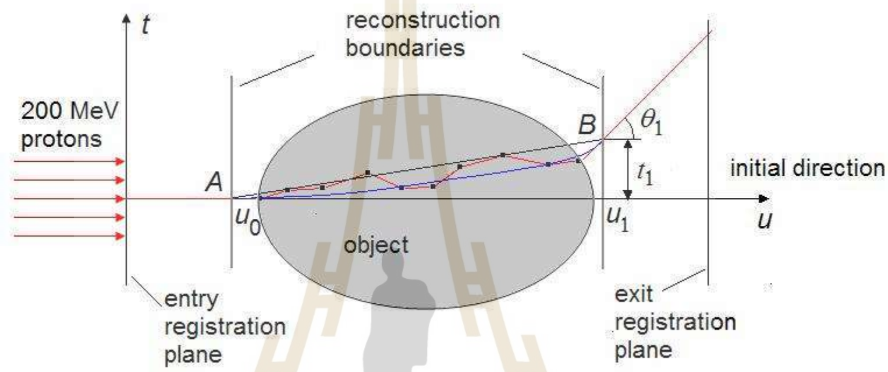

Figure 2.4 The trajectory of protons as they traverse an object is influenced by multiple scattering events, causing their path to zigzag (depicted in red). The entry and exit positions and directions of the protons are recorded. With knowledge of the object's boundary, the points where the proton intersects with the object (points A and B) can be determined. Although these intersection points are sufficient for estimating the straight-line path (shown in black) of the proton, additional information regarding the entry and exit directions enables the estimation of the most probable path (represented by the blue line) (Li et al., 2006).

All of the preceding approaches for calculating the path can be simply utilized in 2D geometry. Estimation in 3D reconstructions is accomplished by projecting the 3D path onto two perpendicular planes and computing the 2D components individually. Because the probability distributions of MCS in a uniform material are isotropic, this approach is justified.

The integral relative stopping power (RSP) is calculated using residual energy measurements after the path estimation method. The Bethe-Bloch theory (Bethe, 1930) accurately describes the stopping power of protons in the appropriate energy range for pCT (20-250 MeV). The density effect and shell adjustments are minimal in this energy range (Leo and Haase, 1990) and can be ignored. As a result, the stopping power of a proton with energy E at a certain point r can be represented as Equation 2.5 of Bethe-Bloch approximation.

$$-\frac{dE}{dx}(E,\mathbf{r}) = \frac{4\pi}{m_e c^2}\frac{\eta(\mathbf{r})}{\beta^2(E)}\left(\frac{e^2}{4\pi\epsilon_0}\right)^2\left[\ln\frac{2m_e c^2}{I(\mathbf{r})}\frac{\beta^2(E)}{1-\beta^2(E)}-\beta^2(E)\right] \tag{2.1}$$

Here, The variable m represents the mass of an electron, η represents the density of electrons, β is the velocity of the proton relative to the speed of light c, e represents the charge of an electron, ϵ_0 represents the permittivity of free space, and I is the average excitation potential of the absorber.

A critical approximation is used in the computation of integral RSP. The non-uniform material's mean excitation potential, $I(\mathbf{r})$, is assumed to be constant and equivalent to a reference material. Water is used in pCT reconstructions because depth-dose curves for treatment planning are typically derived in water. Because of the logarithmic dependency of stopping power on I and the small variation of I among tissues encountered in the human body, this approximation is valid. According to other research, this estimate may result in a maximum inaccuracy of 2%, either overestimating or underestimating the stopping power values of compact bone and adipose tissue (Schulte et al., 2005b). This inaccuracy, however, is minor for most soft tissues, including muscle tissue.

By making this approximation, it becomes possible to RSP solely in terms of the relative electron density. As a result, the spatial distribution of patient stopping powers (S_p) can now be described as

$$S_p(E,\mathbf{r}) \cong \eta_{rel}(\mathbf{r})\, S_{water}(E)\,, \tag{2.2}$$

where η_{rel} represents the patient's electron density at position **r** relative to water. S_{water} represents the stopping power of water at the proton's energy E, which can be determined by applying Equation 2.5 using the relevant water parameters. To calculate the integral RSP (P_{rel}), the terms that depend on both position and energy are separated out as

$$\int_L \rho_{rel}(r)\,dr = \int_L \eta_{rel}(r)\,dr = \int_{E_{out}}^{E_{in}} \frac{dE}{S_{water}(E)}, \tag{2.3}$$

where L represents the length of the estimated proton path. The entry and exit energies of the proton to the image space, E_{in} and E_{out}, respectively. The exit energy is measured using a crystal calorimeter, while the energy of individual protons needs to be predicted from calibration measurements. The accuracy of this prediction depends on the energy spread of the beam from the accelerator and whether or not a scattering system is utilized to produce a wide beam of protons.

2.1.4 Progression of pCT

Table 2.1 presents a summary of the aforementioned systems, which is an attempt to provide an up-to-date overview of the field. It is important to note that many of these systems are still under development, and that the summary is not exhaustive. Additionally, there are other examples that have not been included in the summary, such as a range telescope composed of nuclear emulsions that has been demonstrated in a therapy facility as a proof-of-principle(Braccini et al., 2010). Another example is the use of magneto-optics and collimation to enable pRG by adjusting the relationship between object thickness and flux at a distant detector, which has demonstrated high spatial resolution images using relativistic protons at 800 MeV (Durante and Stöcker, 2012).

2.2 Proton interaction with matter

2.2.1 Interaction mechanisms

Many interactions between protons and atoms or nuclei, such as Coulombic interactions with atomic electrons, Coulombic interactions with the atomic nucleus, nuclear processes, and Bremsstrahlung are occurred when a proton beam is irradiated to matter as shown in Figure 2.5. Protons continuously lose kinetic energy due to frequent inelastic Coulombic interactions with atomic electrons. Because protons are 1832 times heavier than electrons, they normally travel in a straight line. However, if a proton comes close to the atomic nucleus, it experiences a repulsive elastic Coulombic interaction that deflects it from its initial course due to high mass of the nucleus and

Table 2.1 A brief overview of recent and present prototypes for proton CT (pCT).

Collaboration	Size (cm^2)	PSD technology	Resdidual energy detector technology
LLU/UCSC/NIU (Sadrozinski et al., 2013)	17.4 × 9.0	Si strip	CsI (Tl) calorimeters
LLU/UCSC/CSUSB (Aplin et al., 2012)	36.0 × 9.0	Si strip	Plastic scintillator hybrid telescope
PRIMA I (Scaringella et al., 2014)	5.1 × 5.1	Si strip	YAG:Ce calorimeter
PRIMA II (Scaringella et al., 2014)	20.0 × 5.0	Si strip	YAG:Ce calorimeter
INFN (Presti et al., 2014)	30.0 × 30.0	Sci Fi	YAG:Ce calorimeter
NIU/FNAL (Uzunyan et al., 2016)	9 × 9	Sci Fi	Plastic scintillator hybrid telescope
Niigata University (Saraya et al., 2014)	9 × 9	Si strip	NaI calorimeter
QBeRT (Naimuddin et al., 2016)	9 × 9	Sci Fi	Sci Fi range counter
PRaVDA (Taylor et al., 2015)	9.5 × 95	Si strip	CMOS APS telescope
pCT-Bergen (Alme et al., 2020)	27.0 × 16.6	ALPIDE	DTC

charge. Inelastic nuclear reactions between protons and the atomic nucleus are less common, but they can have a greater impact on the individual proton. During a nuclear reaction, an incoming proton enters the atomic nucleus, causing the nucleus to emit a proton, deuteron, triton, or a heavier ion, as well as one or more neutrons. While proton Bremsstrahlung is theoretically possible, it is insignificant at the energy levels of proton beams employed in medical treatments.

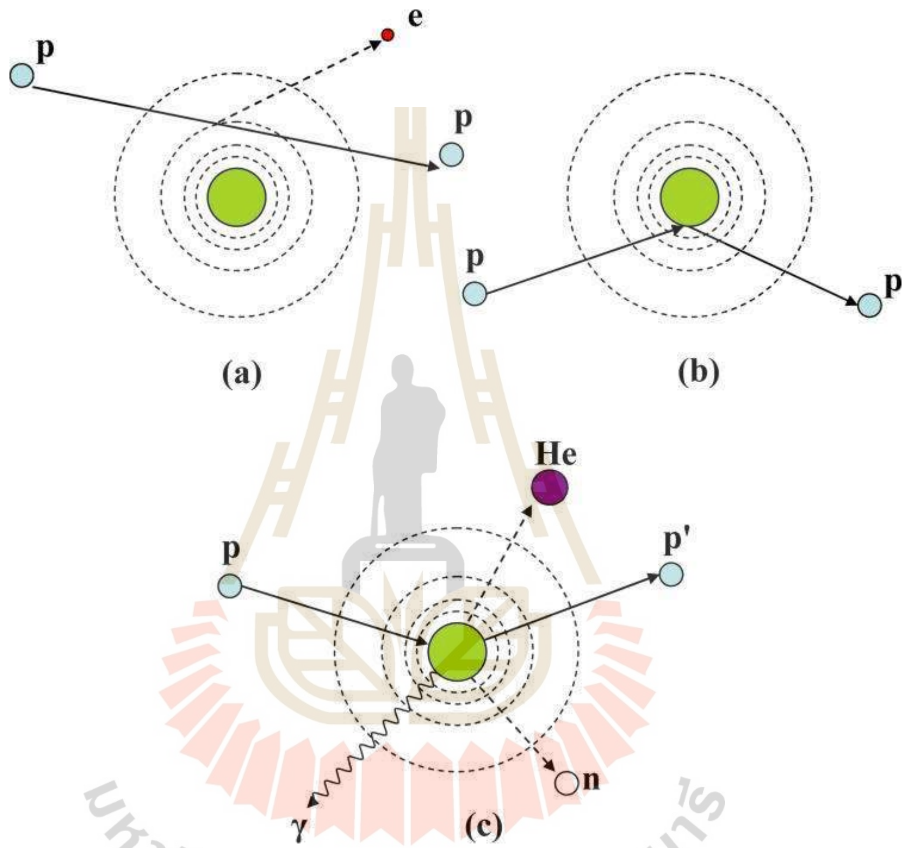

Figure 2.5 The figure displays the primary methods in which protons interact with matter. First, as illustrated in (a), they lose energy through Coulombic interactions. Second, as shown in (b), when protons pass near an atomic nucleus, repulsive Coulombic scattering produces a modification in their initial track. Finally, in (c), the initial proton is eliminated, and non-elastic nuclear interactions produce secondary particles such as neutrons, electrons, helium, and gamma rays (Newhauser and Zhang, 2015).

2.2.2 Energy loss

The linear stopping power of ions, also known as the energy loss rate, is calculated by dividing the change in energy (dE) by the change in distance (dx), where E represents energy and x represents distance. It is frequently represented in a way that is not reliant on mass density to make it more convenient. This is known as the mass stopping power, which is represented as

$$\frac{S}{\rho} = -\frac{dE}{\rho dx} \tag{2.4}$$

This statement is commonly stated in terms of mass density, which is denoted by ρ. It should be emphasized that stopping power is defined for a beam rather than for a single particle.

In 1915, Bohr devised a theory that takes into account the momentum impulse of an unbound electron as well as the impact parameter (Bohr, 1915). Bethe and Bloch later created a more precise equation that takes quantum mechanical effects into account (Bethe, 1930; Bloch, 1933). This equation is written as

$$\frac{S}{\rho} = -\frac{dE}{\rho dx} = 4\pi N_A r_e^2 m_e c^2 \frac{Z}{A}\frac{z^2}{\beta^2}\left[\ln\frac{2m_e c^2\gamma^2\beta^2}{I} - \beta^2 - \frac{\delta}{2} - \frac{C}{Z}\right] \tag{2.5}$$

where several variables are at play. These variables are z (projectile charge), Z (atomic number of the absorbing material), N_A (Avogadro's number), A (atomic weight of the absorbing material), r_e is the classical electron radius, m_e is the mass of an electron, c is the speed of light, $\beta = v/c$ where v is the velocity of the projectile, $\gamma = (1-\beta^2)^{1/2}$, I is the mean excitation energy of the absorbing material, C is shell correction item for low energy protons near the velocity of atomic electrons, δ represents the density correction item due to shielding of remote electrons by close electrons. Both correction elements necessitate the use of relativistic theory and quantum mechanics, particularly for high and low energy proton calculations. Equation 2.5 is used to calculate proton stopping power in water as a function of proton energy in Figure 2.6. It should be noted that Equation 2.5 determines the proton stopping power for a beam rather than an individual particle.

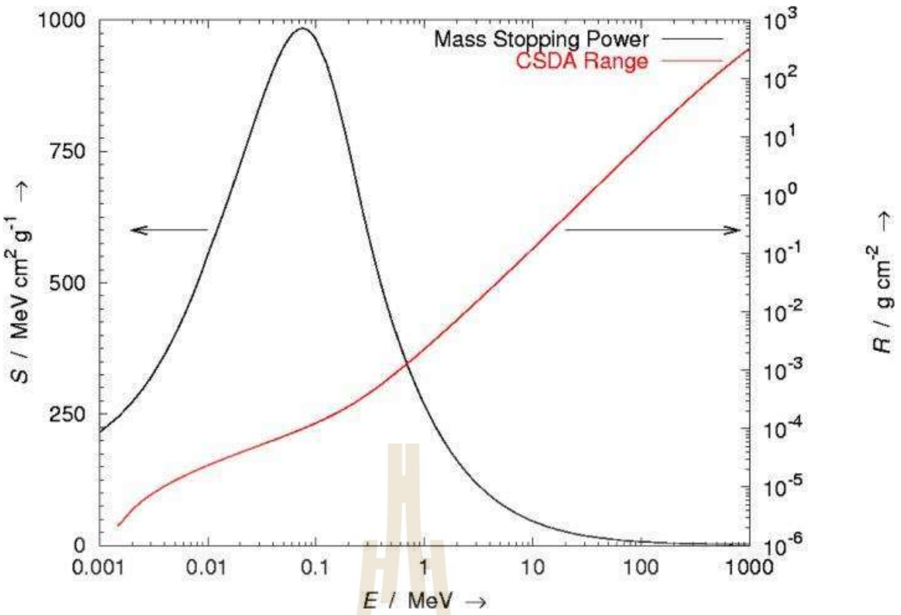

Figure 2.6 This graph illustrates the relationship between protons' mass stopping power (S) and energy (E) in liquid water. The graph also shows the range (R), which is produced by taking the S values and applying the continuous slowing down approximation (CSDA) (Newhauser and Zhang, 2015).

2.2.3 Proton range

The range of protons is the distance corresponding to the depth at which half of the protons in the medium have stopped, as shown in Figure 2.7 by the range-number curve. Although individual protons incur slight changes in energy loss, known as range straggling, the range is normally defined for a beam rather than for individual particles. It is typically described as the distance at which half of the incident protons are halted, while in some situations it may refer to the distance at which half of the protons have reached the limit of their range, excluding those removed by nuclear processes.

The association between the logarithm of the range and the logarithm of the energy is practically a straight line, according to section 2.7. This is fortunate since it means that the range is governed by a simple power law, as Bragg and Kleeman (Bragg and Kleeman, 1905) and other researchers recognized in the early twentieth century. As a result, the BK rule, or equation 2.6, can be used to determine a proton's range.

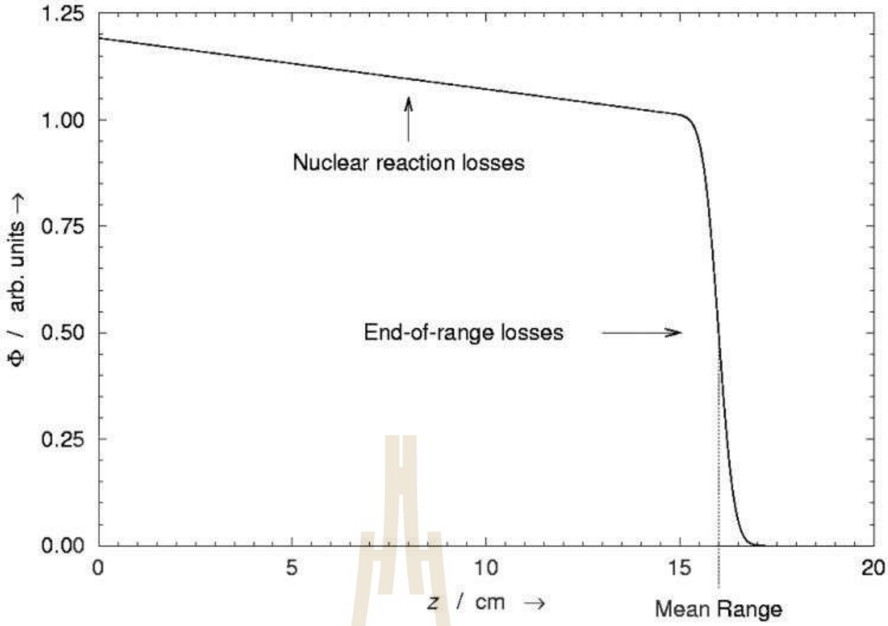

Figure 2.7 This graph demonstrates the proportion of fluence Φ in a broad beam of protons that persists at various depths z in water. Because of nuclear processes, the quantity of protons in the water reduces progressively as they enter. Protons rapidly lose energy and are absorbed by the medium near the end of their range, resulting in a fast decrease in their number. The sigmoid shape of the curve towards the range's end is caused by range straggling or random fluctuations in the energy loss of individual protons (Newhauser and Zhang, 2015).

$$R(E) = \alpha E^{p}, \tag{2.6}$$

where the constant α is material dependent, while E indicates the proton beam's starting energy. The exponent p accounts for the proton's energy or velocity dependence.

The accuracy of proton range measurement is affected by a variety of circumstances. For example, the precision and accuracy of the measuring tool, as well as the experimenter's competence, are important factors of range measurement uncertainty. One major source of worry in clinical proton therapy is the imprecision in calculated range while establishing the settings for a patient's treatment on the treatment equipment. This inaccuracy in range measurement may be influenced by knowledge of proton beam energy distribution as well as the properties of all absorbing materials encountered by the beam. This includes mass density, elemental composition, and linear stopping power. Furthermore, the linear stopping powers calculated from computed tomography (CT) images are subject to a number of additional errors, including problems in CT scanner calibration, partial volume effects, and aberrations caused by motion and streaks.

2.2.4 Energy and range straggling of proton

In previous sections, we assumed that ion slowing occurred in a smooth and continuous way, and the approximation of the energy loss rate by examining the mean energy loss rate and ignoring differences in the energy loss rates of individual protons. While these approximations are frequently adequate for clinical calculations, they fail to account for the accumulation of minor fluctuations in energy loss, known as energy straggling or range straggling, which is one of the physical processes that has a significant impact on the form of a proton Bragg curve. As a result, understanding range straggling is critical for understanding the characteristics of proton dose distributions.

Figure 2.8 presents probability density function (PDF) graphs for the relative energy loss of protons travelling through different thicknesses of water. These curves have been adjusted to aid comprehension. Thin absorbers have asymmetric curves with modes less than the mean and long tails with significant energy losses, whereas thick absorbers have symmetric energy loss distributions. While numerical methods can theoretically compute straggling PDFs, they are generally computed theoretically in practice. Three such regularly utilized theories will be discussed later in the section.

2.2.5 Multiple Coulomb scattering

When a proton approaches a nucleus, the nucleus's repulsive force deflects or scatters it. Although the proton does not lose much energy during this form of scattering, even a little modification in its route can be critical. Coulomb scattering must be considered when designing beamlines and treatment heads (Gottschalk, 2010), as well as when calculating dose distributions for phantoms or patients, such as using treatment planning systems (Hong et al., 1996; Pedroni et al., 2005; Schaffner, 2008; Koch and Newhauser, 2010).

A parameter called scattering power, represented as T, measures the degree of deflection generated by scattering in a beam as in equation 2.7.

$$T = d\langle \theta^2 \rangle / dx \tag{2.7}$$

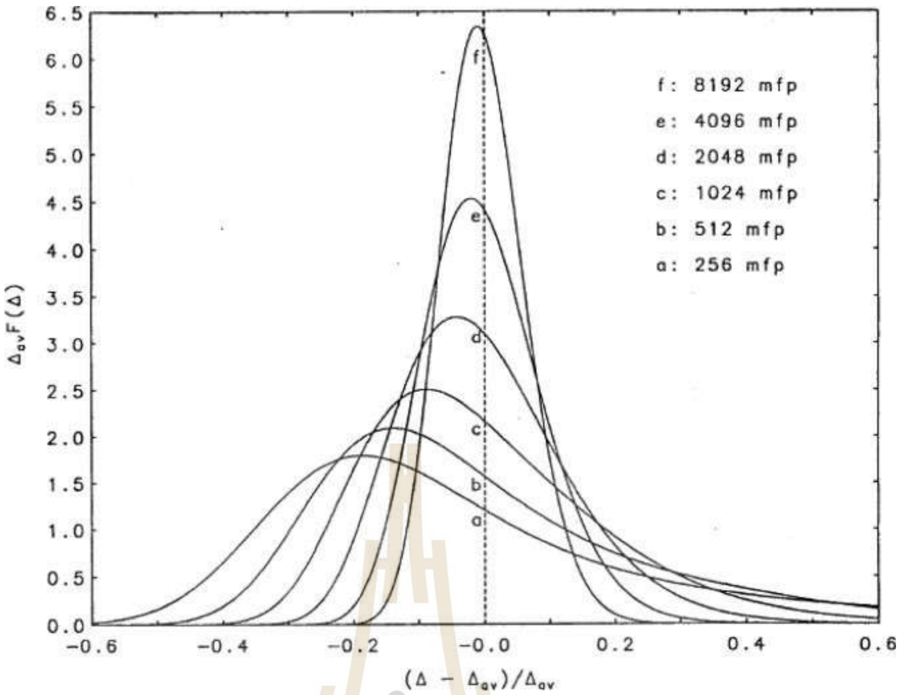

Figure 2.8 Energy loss probability density functions (PDFs) for water absorbers of various thicknesses. The absorber thickness is indicated in mean free path (mfp) units, and the PDFs have been scaled on both the x- and y-axes for clarity. The PDFs represent the energy lost by a single event as a proportion of the total energy lost across the absorber's thickness, or $(\Delta - \Delta av)/\Delta av$. Each PDF was normalized so that the integral over all energy losses was the same. The PDFs for thin absorbers (curves a-e) are asymmetric and wider, and are modeled using the Vavilov (Vavilov, 1957) or Landau (Landau, 1944) theories. The PDF for thick absorbers (curve f) is symmetric and well approximated by Bohr's theory, which is a Gaussian distribution (Bohr, 1915; International Commission on Radiation Units and Measurements, 1993).

where x is the thickness of the absorber through which the proton travels, and $\langle\theta^2\rangle$ is the average of the square of the scattering angle. Furthermore, the mass scattering power can be determined by dividing the stopping power (T) by the absorber material's mass density (ρ). Because scattering is symmetric about the central axis and the mean scattering angle is zero, the definition of scattering power employs the square of the scattering angle. Furthermore, the scattering power value is affected by the thickness of the absorber under consideration, which is affected by the material qualities and dimensions of the absorber.

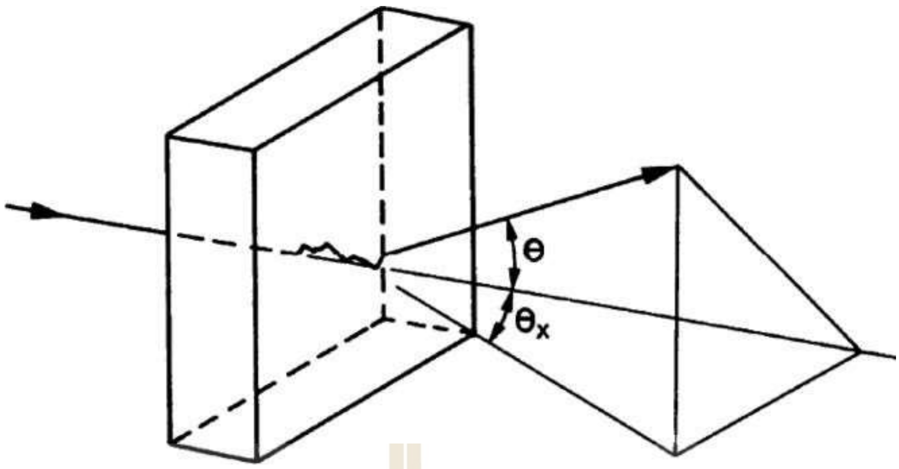

Figure 2.9 This illustration shows the passage of a proton through many Coulomb scattering events. The graphic additionally labels the scattering angle's root mean square (rms), denoted as θ, and the projected scattering angle, denoted as θx (Leo, 1994).

2.2.6 Nuclear interactions

Protons can induce non-elastic nuclear processes in which the nucleus is irrevocably altered. In the (p,n) reaction, for example, a proton is absorbed by the nucleus and a neutron is released. Such events occur inside the therapeutic region of a proton field and primarily result in a slight reduction of the absorbed dose due to the elimination of initial protons. However, the release of secondary protons and other ions compensates for this loss.

To better understand reaction mechanisms, we look at a range-number curve (Figure 2.7), which depicts the residual number of protons in an absorber as the beam ceases. The elimination of protons from nuclear processes is responsible for the depletion of protons from the entry to near the end of the range. The sudden decrease in the amount of protons near the end of the range is caused by ions that have run out of energy and are absorbed by the medium. The sigmoid shape of the falloff is caused by range straggling or stochastic fluctuations in the individual proton energy loss.

2.3 Track reconstruction

Track reconstruction is the technique of reconstructing the trajectories of charged particles created in high-energy and particle physics. When these particles pass through a detector, they leave traces or ”hits” in the sensitive materials of the detector, such as silicon or gas chambers. The goal of track reconstruction is to use these impacts to retrace the particle’s path and identify its momentum, charge, and, in some cases, identity.

Pattern recognition, track fitting, and vertexing are part of the track reconstruction process. The technique of detecting hits in the detector that belong to the same type of particle is known as pattern recognition. The process of identifying the best-fit track that passes through all of the identified hits is known as track fitting. Vertexing is the process of determining the point at which two or more tracks meet, which is frequently a signal of fascinating physics, such as the creation of a new particle.

2.3.1 Track finding

The LHC experiments include situations in which many measurements are either meaningless noise or from irrelevant low-energy particles. As a result, researchers must investigate several hypotheses in order to find a collection of promising track candidates, which can be a time-consuming and laborious operation. The processing speed is critical, and the choice of algorithms may be influenced by it. The track model, which describes how charged particles flow in the detector’s bulk, is typically used to find tracks. If time is of the essence, simplified track models may be used. Simplified track models are especially beneficial for triggering applications, when locating interesting events online is part of the approach. This study is not about triggering applications, but rather approaches for offline data analysis, or analyzing data saved in a mass storage.

Track detection systems are classified into two types: global and local. Global approaches examine all measurements at once, whereas local methods examine measurements sequentially. Conformal mapping, Hough transform, and Legendre transform are examples of global methods, whereas track road and track following are examples of local methods.

Track following

The track following method begins with a track seed, which is often a short track section constructed from a few measurements. The seed could be forced to point to the interaction region. Seeds can form in the tracking detector's inner region, where readings are generally quite exact, or in the outside region, where track density is lower. After establishing a seed, the track is projected to the next detector layer with a measurement. The measurement that is closest to the anticipated track is then added to the track candidate, and the procedure is repeated until either too many detector layers with missing readings are encountered, or the detector system reaches its limit.

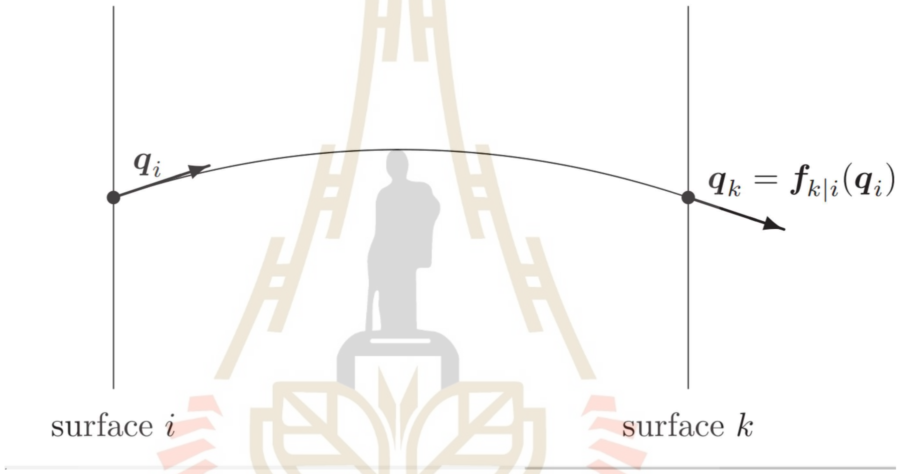

Figure 2.10 This picture shows the concepts underlying the track model and propagation. The track propagator is the function $f_{k|i}$, which advances the track from surface i to surface k. The mathematical form of this function is determined by the track model, which is the solution to the equation of motion in the detector's magnetic field (Koch and Newhauser, 2010).

2.3.2 Track fitting

Based on the data received from the track candidate, the primary goal of the track fit is to find a group or series of properties that describe the motion of a charged particle. However, the measurements gathered are probabilistic in nature and have related uncertainties, making the estimating procedure statistical. In the form of a covariance matrix, the track fit also offers information on the uncertainty of the predicted parameter values. Many estimating methods are made up of core building blocks that can be disassembled into simpler components.

2.4 Monolithic Active Pixel sensors

Monolithic Active Pixel Sensors (MAPS) are image sensors that incorporate both the read-out circuitry and the sensors onto a single silicon substrate. These sensors were first introduced as part of an upgrade to the inner detector of the Solenoidal Tracker (STAR) at the Relativistic Heavy Ion Collider (RHIC) for use in high-energy particle investigations. The goal was to increase vertex resolution accuracy (Dorokhov et al., 2011; Schambach et al., 2015; Kittimanapun et al., 2017). During the research and development phase, the MAPS was subjected to extensive testing with both radiation sources and high-energy particle beams to ensure that it satisfied all of the essential standards. The STAR experiment successfully used the first MAPS, known as the ULTIMATE sensor (Mager, 2016).

2.4.1 Semiconductor physics

A semiconductor is a substance with electrical conductivity between that of a conductor (such as copper or gold) and that of an insulator (such as rubber or glass). A semiconductor's conductivity can be controlled and varied by introducing impurities, a process known as "doping", which affects the quantity of electrons or holes (positive charge carriers) in the material. Because of this feature, semiconductors are valuable for electrical devices like transistors, diodes, and integrated circuits, which are the foundation of contemporary electronics. Silicon is the most often used semiconductor material, however germanium and gallium arsenide can also be utilized.

A monolithic active pixel sensor is a semiconductor device used to detect incoming light sources or particles. The materials used in the construction of MAPS are semiconductor impurities.

Silicon electronics structure

A silicon atom is made up of 14 protons and 14 electrons. The atom's first energy level contains two electrons, while the second energy level contains eight electrons, leaving only four electrons at the outermost level. This outermost level should ideally have eight electrons, as seen in the image below.

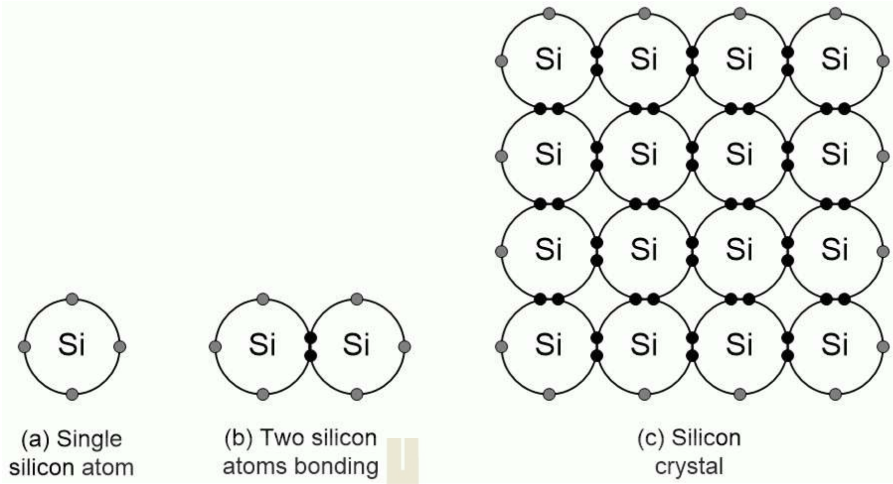

Figure 2.11 (a) - The outermost shell of a silicon atom contains four electrons. (b) - A valence bond is formed when two silicon atoms come together, with each atom contributing one of its valence electrons. (c) - The silicon atoms continue to assemble to create a silicon crystal. With the exception of the atoms on the crystal's outer borders, each silicon atom establishes valence bonds with its four neighboring atoms. (Source: Max Maxfield)

A n-type silicon is a conductive kind of silicon that has been doped with phosphorus gas. Normally, a silicon atom has four electrons in its outer shell and bonds firmly with four surrounding silicon atoms to produce a crystal matrix with eight electrons in the outer shells. When phosphorus is added to silicon, the fifth electron becomes a "free" electron, allowing it to travel freely within the crystal when a voltage is applied. The word "n-type" alludes to a negative charge because these charge carriers are electrons.

A p-type silicon, on the other hand, is generated by adding boron gas to silicon, resulting in a conductive material that can easily receive electrons under a voltage. Boron contains three electrons in its outer shell, therefore it can only connect with three of the four adjacent silicon atoms, leaving one silicon atom's outer shell empty. This is known as a "hole", and it can easily accept an electron. A p-type silicon is positively charged because the charge carriers are holes.

When band theory is applied to impurity-doped semiconductors, it reveals that extra energy levels have been introduced. In the case of n-type semiconductors, energy levels towards the top of the band gap make electrons travel easily to the

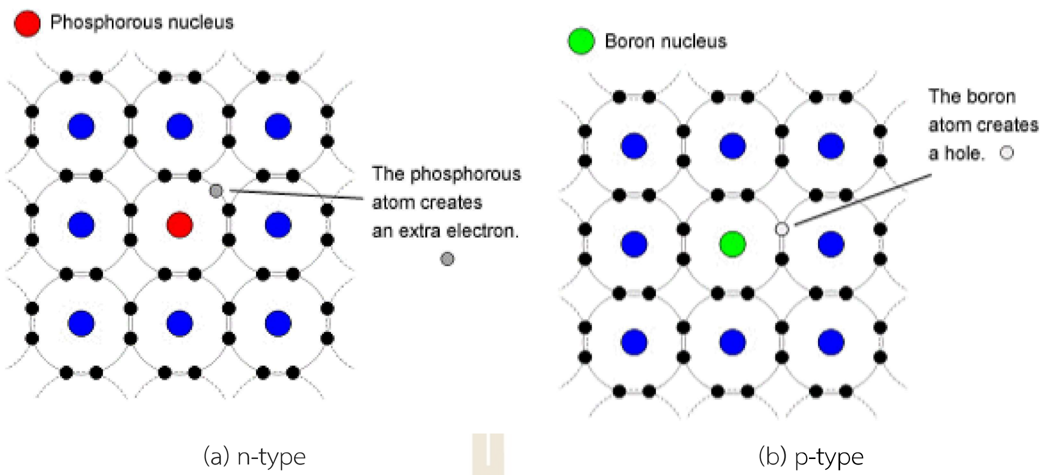

Figure 2.12 The mental representation of n-type and p-type atomic structures of doped silicon. (Source: http://www.answers.com/topic/n-type-silicon-technology)

conduction band. Extra holes in the band gap in p-type semiconductors can assist the migration of valence band electrons, resulting in mobile holes in the valence band.

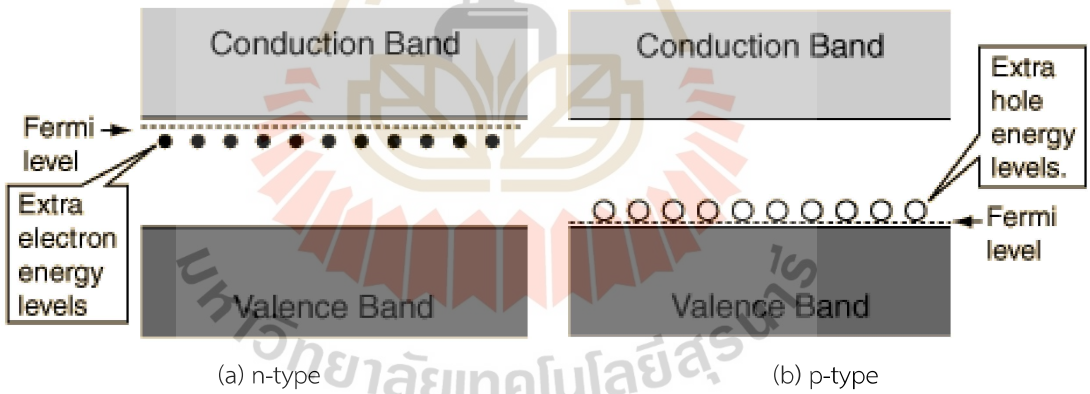

Figure 2.13 The illustration of n-type and p-type doped semiconductor band structures. (Source: http://hyperphysics.phy-astr.gsu.edu)

Depletion region

A thin layer occurs at the junction of p-type and n-type semiconductors, forming the depletion area. The word "depletion" region refers to the fact that this region is depleted of mobile charge carriers. The depletion region arises as a result of charge carrier diffusion across the junction, which results in the formation of an electric field that precludes further diffusion. The zone is an insulator because the positive and negative ions within it are immobile, forming a potential barrier that resists current flow. The doping concentration and the voltage applied across the junction influence the width of the depletion region.

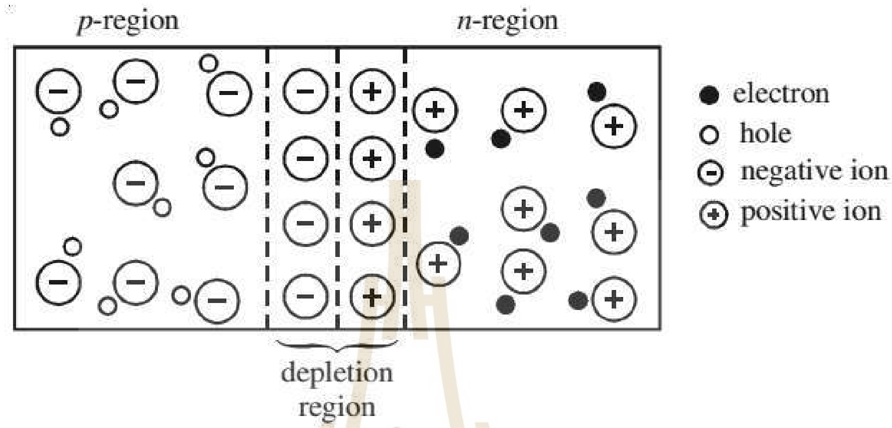

Figure 2.14 The illustration of a depletion region formed by linking n-type and p-type semiconductors. (Source: https://www.studypage.in/physics/formation-of-a-p-n-junction)

The electric field, potential, and width of the depletion zone can all be calculated by solving the one-dimensional Poisson equation, as shown below,

$$W = x_n + x_p = \sqrt{\frac{2\mathcal{E}_0\mathcal{E}_{Si}}{e}\left(\frac{1}{N_A} + \frac{1}{N_D}\right)(V + V_{bi})}, \tag{2.8}$$

where the depletion zone in a semiconductor is the area that lacks mobile charges due to the junction of p-type and n-type materials. x_n is an n-type region, whereas x_p is a p-type zone. W represents the width of this zone, which is determined by the concentration of donors and acceptors (N_D and N_A), the bias voltage (V_{bi}), and the externally applied voltage (V). The junction of a silicon sensor is normally formed by implanting a shallow and highly doped p^+ implant in a low-doped bulk material.

Charge generation

MAPS detects particles by interacting with high-energy particles via a semiconductor sensor. As a particle passes through the sensor, it generates electron-hole pairs. These electrons spread out until they reach the depletion region, where they are drawn towards and captured by the electrode. As shown in Figure 2.15 , the electrode generates a signal that is picked up by an electrical circuit for further processing. (Greiner et al., 2011).

The 180 nm CMOS Imaging Process from TowerJazz has been chosen as the technology for the ALICE Inner Tracking System (ITS) update, which includes ALICE Pixel Detector (ALPIDE) and MISTRAL-O. The ALPIDE design makes the best advantage of the process characteristics, particularly the high integration density provided by six metal layers and the compact structural size. Furthermore, the deep p-well plays an important role in enabling the production of PMOS transistors on a p-type epitaxial layer without compromising charge collection. As seen in Figure 2.15, this is accomplished by effectively concealing the n-well from the epitaxial layer. The incorporation of significant CMOS hardware within the pixel matrix allows for a change in read-out paradigm, moving away from the traditional rolling shutter readout commonly used in MAPS. Instead, more energy-efficient methods can now be put in place (Mager, 2016).

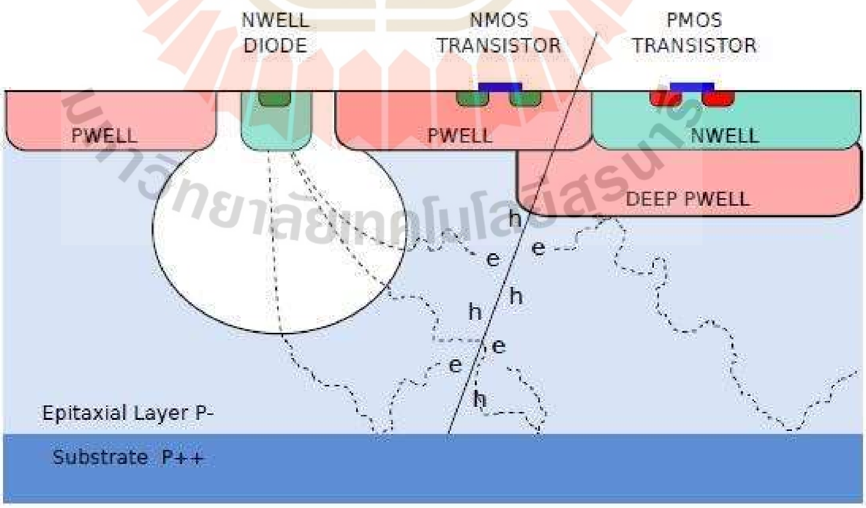

Figure 2.15 Schematic cross section of a MAPS pixel (Kofarago, 2015).

2.4.2 The ALICE detector

The ALICE experiment is a key component of CERN's Large Hadron Collider (LHC), designed to study heavy-ion collisions of Pb-Pb nuclei at a center of mass energy of 5.5 TeV per nucleon pair, with a focus on studying the properties of Quark-Gluon Plasma (QGP), a state of matter thought to have existed shortly after the Big Bang. The ALICE experiment intends to modify the Inner Tracking System (ITS) to improve measurement precision and event readout rate. The new ITS installation took place during the LHC's second lengthy outage (LS2) in 2019-2020. (Satz, 2011; ALICE Collaboration, 2008; ALICE Collaboration, 2012; ALICE Collaboration, 2014)

Figure 2.16 depicts a graphic representation. This apparatus is 26 meters long and 16 meters tall, and it is made up of eighteen sub-detector systems built for specialized applications. These systems are typically used for vertex reconstruction, particle identification (PID), and tracking.

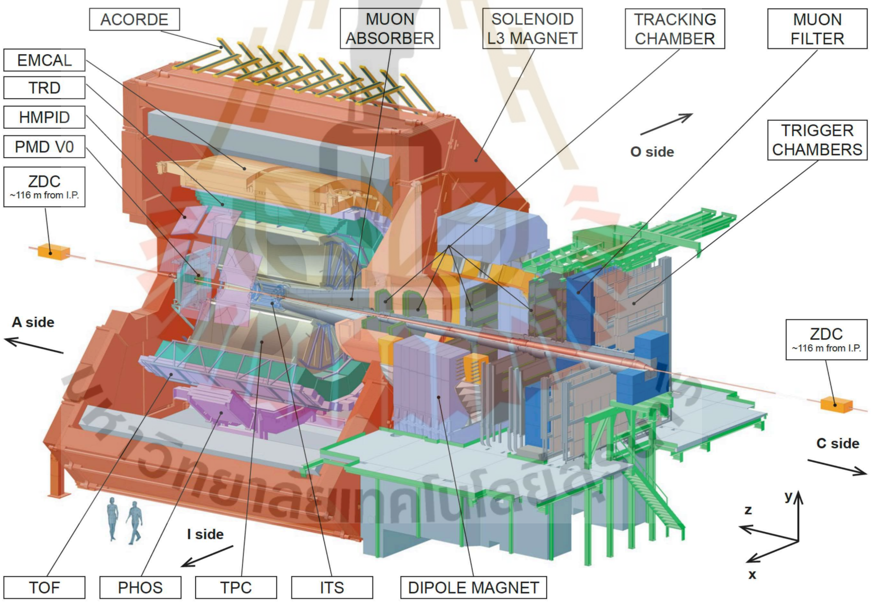

Figure 2.16 A schematic illustrating the ALICE experiment (ALICE Collaboration, 2008).

2.5 Cyclotron

A cyclotron is a type of particle accelerator that employs a magnetic and an electric field to accelerate charged particles like protons to extremely high energy.

Ernest O. Lawrence and his colleagues at the University of California, Berkeley invented it in the 1930s. Charged particles are fed into a pair of hollow chambers known as the "dees" in a cyclotron and subjected to a high magnetic field, which causes them to move in circular orbits. The dees are subjected to an oscillating electric field, which accelerates the particles each time they pass through the space between the dees. The particles' energy grows with each pass until they reach the appropriate amount, as shown in Figure 2.17. Cyclotrons are employed in a wide range of scientific and medical purposes, including nuclear physics research, isotope manufacturing, and cancer treatment with proton therapy.

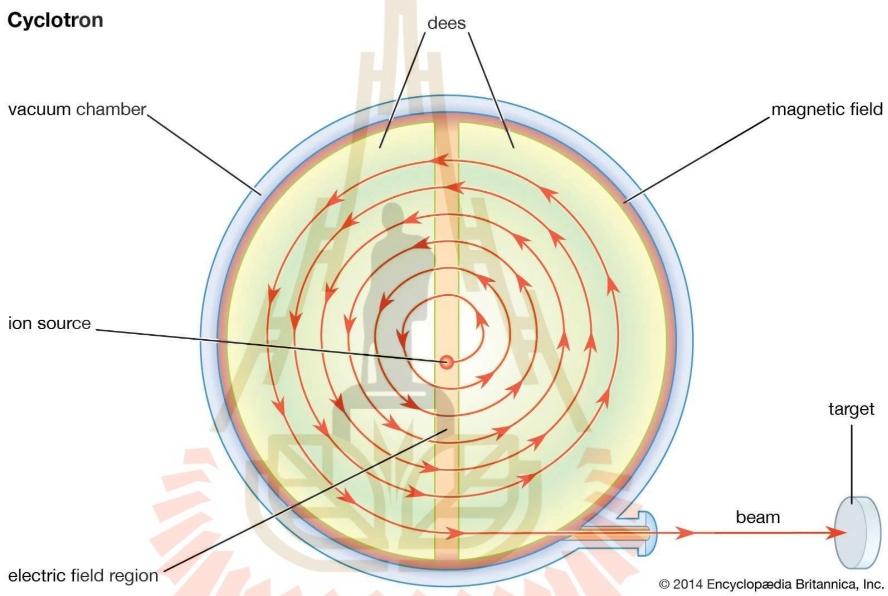

Figure 2.17 A plan view of a cyclotron containing a cylindrical chamber with a centrally positioned ion source. The chamber is vacuum-packed and sandwiched between the poles of an electromagnet, which provides a uniform magnetic field perpendicular to the chamber's flat faces. The voltage is generated by an oscillator that operates at a frequency equal to the rotational frequency of the particles in the magnetic field. The accelerated particles travel in semicircular trajectories with increasing radius (Britannica The Editors of Encyclopaedia, 2024).

2.5.1 King Chulalongkorn Memorial Hospital Proton Center

The King Chulalongkorn Memorial Hospital (KCMH) now features a proton cyclotron (Varian ProBeam Compact Therapy System). The Energy Selection System

(ESS) is part of the beam transport system and is depicted in Figure 2.18 at the system's commencement. It is used to convert the cyclotron's fixed energy of 250 MeV to the therapeutic energy range of 74 to 245 MeV. This energy range corresponds to a water depth of around 4 to 37 cm. The ESS picks the desired therapy energy and directs it to the patient's treatment room.

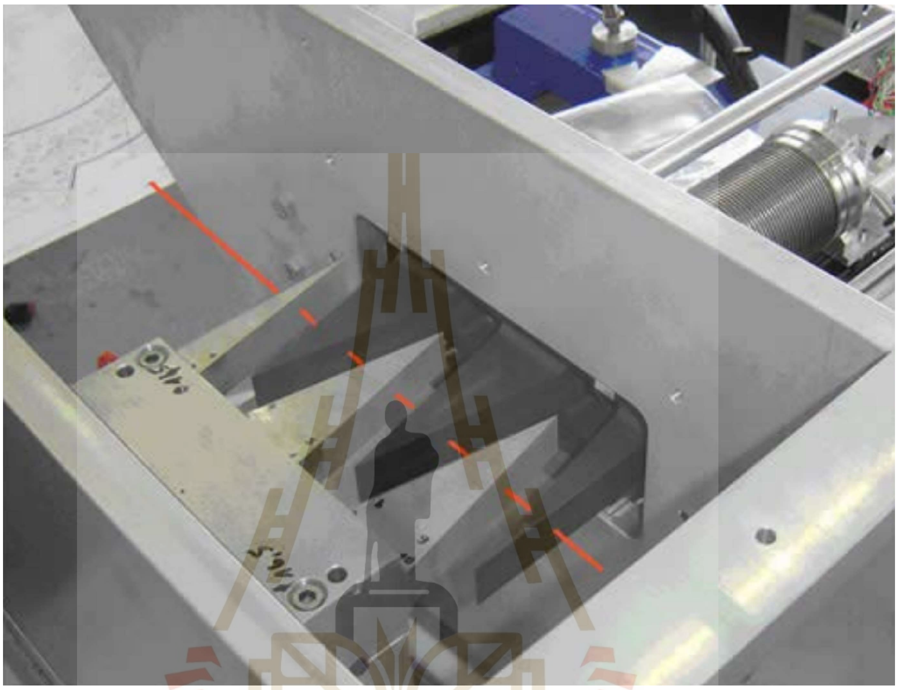

Figure 2.18 The figure of ESS by using multi-wedge graphite absorbers. The absorbers are positioned from opposing sides of the beam route, and when they move into the path, they modify the energy by forming a uniform layer of carbon, ensuring uniformity (Source: Varian medical systems).

CHAPTER III
PROTON TRACK RECONSTRUCTION: MONTE CARLO SIMULATION AND ANALYTICAL MODELS

This chapter describes the Monte Carlo simulation of the MAPS telescope. The track reconstruction is applied to the results to benchmark the telescope for proton computed tomography.

3.1 Introduction

Geant4 is a software toolkit specifically developed to simulate the interaction between particles and matter. It offers a comprehensive set of functionalities, such as tracking particles, representing geometries, modeling physics phenomena, and recording particle interactions. The toolkit covers a wide range of physics processes, including electromagnetic, hadronic, and optical processes, as well as an extensive collection of materials, elements, and long-lived particles. Geant4 is implemented in C++ and has been widely utilized in diverse fields, including particle physics, nuclear physics, accelerator design, space engineering, and medical physics.(Agostinelli et al., 2003)

The GATE software, which is an adaptation of the Geant4 toolkit, serves as a Monte Carlo simulation platform specifically designed for nuclear medicine applications (Agostinelli et al., 2003). In GATE, the simulation process has been simplified by executing it through a macro file, eliminating the need for compilation. Additional functionalities have been incorporated into the detector options, allowing for easier construction of geometries, readout operations, and trigger mechanisms. A Monte Carlo simulation was performed on the entire detector system using the GATE 9.2.0 program, which is based on Geant4 version 11.0.0. (Jan et al., 2004)

3.2 Material and method

The distance between the nozzle and the isocenter measures 42.1 cm, and the first layer of sensors is positioned at the isocenter. The telescope comprises six ALPIDE sensor planes that are spaced 25 mm apart from each other. The initial sensor plane is located precisely at the isocenter point. This telescope design is reminiscent of the beam test facility (BTF) at Siam Research Light Institute (SLRI), which utilizes five sensor planes for characterizing ALPIDE with an electron beam (Kaewjai et al., 2019). In the case-of KCMH, an additional layer has been added to the telescope, bringing the total to six layers.

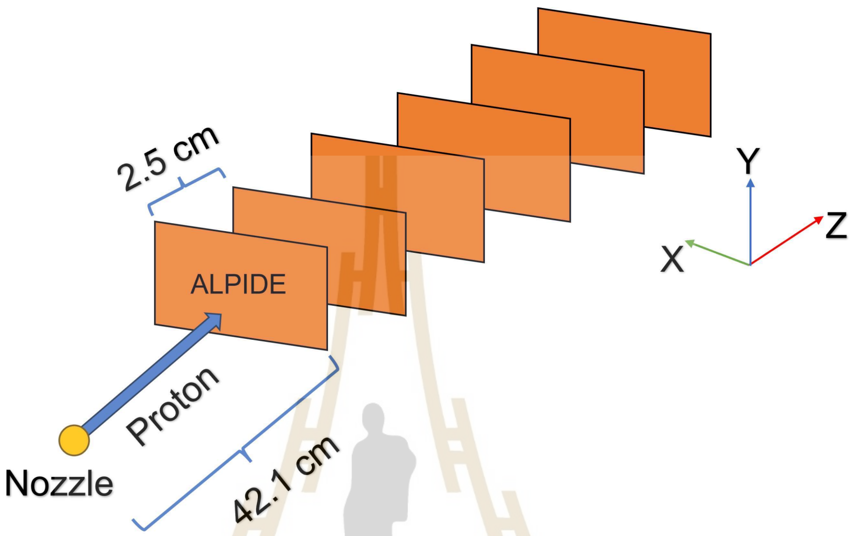

Figure 3.1 The detector geometry of MAPS telescope in GATE simulation which has 2.5 cm of air gap between each ALPIDE. The distance between nozzle and isocenter is about 42.1 cm that the first ALPIDE is located at the isocenter.

3.2.1 Layer material properties

The latest version of the ALPIDE chip is fabricated using a 180-nm CMOS imaging process and is constructed on substrates with a high-resistivity epitaxial layer, which has been thinned down to 25 μm. The chip itself has dimensions of 15 mm x 30 mm and consists of a matrix composed of 512 x 1024 pixel cells. Each pixel cell measures 26.88 μm x 29.24 μm and is read in a binary manner, indicating either a hit or no-hit (Aglieri Rinella, 2017; Yang et al., 2019), as depicted in Figure 3.2. The peripheral region of the chip, spanning 1.2 mm x 30 mm, incorporates analog biasing, control, hit-driven readout, and interfacing functionalities. The sensitive area of the chip covers 13.8 mm $\times$ 30 mm. Additionally, there exists an 11 μm metal layer positioned above the epitaxial layer, serving as the in-pixel circuitry, and facilitating the transmission of signals and biases from the peripheral region of the chip.

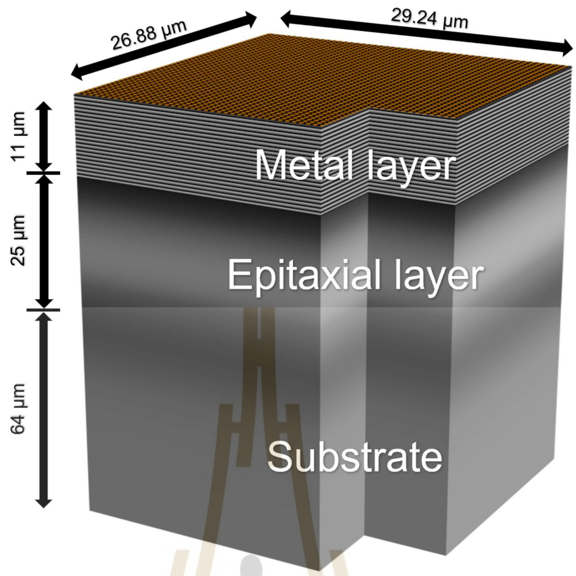

Figure 3.2 Schematic cross-section of ALPIDE.

The sensitive detector function of the epitaxial layer is achieved by incorporating the crystalSD. This crystalSD serves the purpose of monitoring interactions that take place within the volumes linked to a scanner, including crystals or collimators. It collects pertinent data regarding these interactions, such as the deposited energy, interaction location, particle source (emission vertex), type of interaction (name of the involved physical processes), and more. The attachment of a crystalSD is limited to volumes belonging to a specific system, and once attached, it remains associated with that system. The attachment process is carried out using the attachCrystalSD command. While scintillating elements (crystals) are typically the volumes to which this sensitive detector is attached, it is also possible to attach it to non-scintillating components such as collimators, shields, or septa.

3.2.2 Beam modelling

Pencil beam scanning (PBS) is an advanced technique employed in radiation therapy to precisely and accurately target tumors during treatment. Unlike traditional radiation therapy, which administers a uniform radiation dose to both the tumor and surrounding tissue, PBS utilizes a narrow beam of radiation that is shaped and scanned layer by layer across the tumor. By adjusting the intensity and shape of the beam, medical professionals have the ability to finely control the radiation dose delivered to the tumor while minimizing exposure to healthy tissue. This approach enables the administration of higher radiation doses to the tumor, potentially enhancing treatment effectiveness while reducing side effects. PBS is typically performed using a particle accelerator like a synchrotron or cyclotron and finds frequent application in treating cancers in sensitive areas such as the brain and spine.

The Lynx PT device from IBA dosimetry is used to measure the proton beam at KCMH, as depicted in Figure 3.3. To generate this beam, the GATE PBS PencilBeam source package is employed. The primary particle type is set to protons, and their energy is measured in MeV. The distribution of particle energies within the beam can vary depending on the source and is often represented by statistical distributions such as Gaussian or uniform distributions. The pencil beam shape itself is Gaussian, and the spot sigma can be adjusted for the X-Y plane shape and angles.

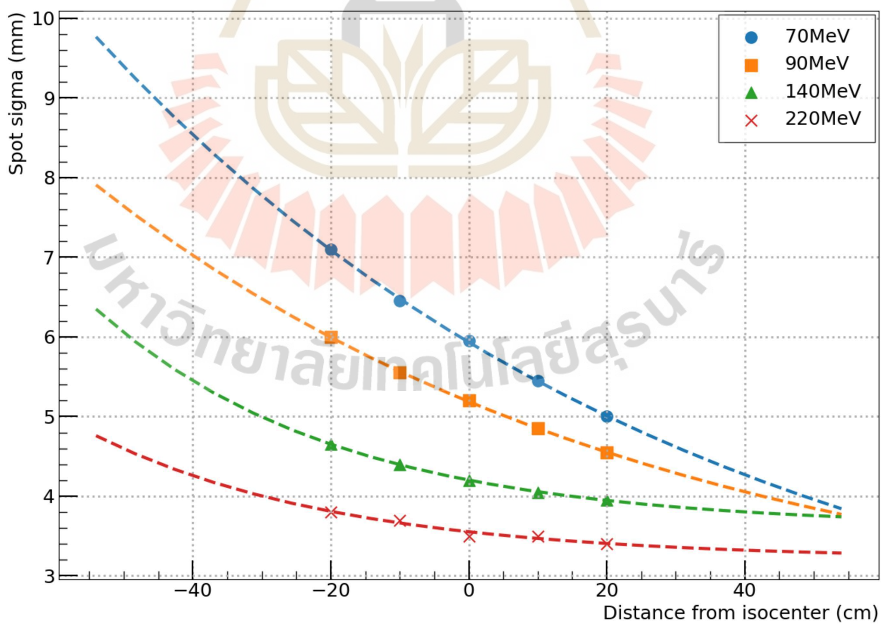

Figure 3.3 The measurement of KCMH proton beam at distance from isocenter.

3.2.3 Physics list

A physics list comprises a collection of models that describe the behavior of particles during their interactions with matter. It outlines the specific physics processes used to simulate the movement of particles through different materials, encompassing electromagnetic, hadronic, and optical processes. The physics list plays a vital role in determining various aspects of particle-matter interactions, such as energy loss, generation of secondary particles, and absorption.

Within the GATE framework, a physics list can be customized to meet the requirements of different applications. The toolkit provides a wide range of predefined physics lists tailored for various scenarios, including low-energy and high-energy physics. Users have the flexibility to select the appropriate physics list that suits their needs or even create their own custom physics list by choosing the necessary models and configuring them accordingly.

In this specific work, the simulation models employ the QGSP_BIC_EMY physics list, which includes G4EmStandardPhysics_option3 for simulating medical applications.

3.2.4 Data collection and conversion

GATE offers various output formats that can be enabled according to requirements. In this particular study, the root format is chosen. By default, the root file stores Hits Tree information, allowing event-by-event output (Brun and Rademakers, 1997). For SPECT systems, the root file contains two trees labeled as Hits and Singles. For PET systems, it includes three trees: Coincidences, Hits, and Singles. Each tree stores multiple variables relevant to the simulation.

The Hits tree encompasses numerous simulation properties that are utilized in preprocessing data for analysis in the track reconstruction algorithm. The following parameters are employed in this process.

- eventID - an identification allocated to a particular event or collision. When high-energy particles collide, a significant number of particles are produced, which are detected and recorded by a variety of detector elements such as tracking detectors, calorimeters, and muon chambers. Each recorded event provides data on the particles created by the collision, such as their momenta, energy, and other attributes.

- PDGEncoding - a unique integer value of each particle species in the Particle Data Group (PDG) particle listings. The PDG is a multinational cooperation that gathers and summarizes all known particle parameters, such as masses, lifetimes, and decay modes.

- trackID - a unique identifier of each charged particle identified in an experimental device or simulated in a computer simulation. A track is essentially a reconstruction of a trajectory in charged particle via a detector or simulation.

- parentID - an identification assigned to the parent particle that created a specific particle in a simulation or experimental measurement. This is often employed in particle collision analysis, where a high-energy particle collides with another particle, resulting in a cascade of progeny particles.

- edep - the quantity of energy deposited by a particle as it travels through a substance or a detector is referred to as energy deposition. When a particle interacts with matter, some or all of its kinetic energy is transferred to the surrounding substance. This energy deposition can have a variety of impacts on the material, such as ionization, excitation, or heating.

- posX, posY, posZ - the position of a particle in a detector or simulation along the X, Y, and Z axes. When a charged particle passes through a detector, it can generate signals in a variety of detector elements, including wire chambers, silicon detectors, and drift chambers. Physicists can reconstruct the trajectory of the particle and calculate its position and momentum by measuring the position of these signals along each axis.

- level1ID - the identifier assigned to a particle contender at the first level of trigger mechanism from a particle detector. The first level in this simulation referred to layer number of the telescope. When high-energy particles collide, a vast number of particles are produced, many of which are irrelevant to the physics study being done. Detectors often employ trigger systems to identify events of interest, which apply a series of selection criteria to detector signals to identify events of interest.

For this study, a Python script was employed to examine the conversion of raw data to root file format, allowing the collection of every event as multiple root files. Both experimental and simulation data were transformed into Pandas DataFrames to facilitate the analysis of object-oriented data, following established conventions (McKinney, 2010). Additionally, ID properties were added to the simulation data after preprocessing to identify the particle hits for each event across all detector layers.

3.2.5 Particle track reconstruction

Particle track reconstruction is the procedure of utilizing detector data to reconstruct the paths traversed by particles through a material. It encompasses the identification and amalgamation of signals from various detector elements to reconstruct the trajectory of a particle. This is typically achieved by fitting the collected data to a mathematical model. The objective of particle track reconstruction is to precisely determine the properties of the particles, including their energy, momentum, and type, through the analysis of the detector data.

Track following algorithm

Track following is a technique widely used in particle physics to simulate the movement of particles as they traverse a detector. It entails tracing the path of the particle while it interacts with the detector material, considering deflections or changes in direction caused by scattering or other interactions. This information is crucial for reconstructing particle path and determining additional properties such as energy and charge. Sophisticated computer algorithms are typically employed for track following, taking into account various physical processes and detector characteristics. These algorithms can analyze MC simulation data to capture proton tracks from the telescope.

By utilizing 3D hit data from the telescope, it becomes feasible to reconstruct multiple particle tracks occurring simultaneously within a single data readout cycle. In a particular study, Pettersen et al. (Pettersen et al., 2020) presented algorithms for track reconstruction in a Double-Tree Cluster (DTC) detector. The approach involves a track-following and track-splitting scheme that starts from the end of the detector and progresses towards the front end, following the methodology proposed by Strandlie and Frühwirth (Strandlie and Frühwirth, 2010). The algorithm demonstrated high accuracy in detecting tracks. Further details of the algorithm are provided below.

1. Choose a hit located in the initial layer of the telescope as a seed (represented by hits in layer 0 in Subfigure (A) of Figure 3.4), potential track candidates can be

identified by searching through the remaining hits from the seed until reaching the final layer of the telescope.

2. A cone shape is employed to determine the angle between the track direction of the previous layer and the vectors connecting the previous hit and the current hit. The cone angle is evaluated using a cumulative value, S_{max}, which assesses each search angle from all potential candidates. If the cone angle is too large, the current candidates are discarded, while a smaller cone angle includes the candidate as a track (as depicted in Subfigure (B) of Figure 3.4).

3. Compute the angular deviation for each possible option in the subsequent layer and evaluate it: $S_n = \sqrt{\sum_{layer}^{n} (\Delta\theta_{layer})^2}$ (as illustrated in Subfigure (B) of Figure 3.4), where n represents the number of layers in the telescope.

4. Gather the hits where the calculated value of S_n is less than S_{max}, designating them as part of the track (as shown in Subfigure (C) of Fig. 2.8). If multiple hits are detected, the candidate with the lowest S_n value is selected as the new segment of the track (depicted in Subfigure (D) of Figure 3.4).

5. Repeat the aforementioned procedure and continue tracking all candidates using a recursive algorithm (as depicted in Subfigure (E) of Figure 3.4) until the final layer is reached during the search process.

6. Remove the hit members of the fully reconstructed track from the hit data and repeat the process of selecting a seed from layer 0 once more (as shown in Subfigure (G) of Figure 3.4). Run the track reconstruction algorithm again to obtain new tracks until there are no more seeds remaining on the first layer (depicted in Subfigure (H) of Figure 3.4).

Searching cone

As outlined in previous subsection, the region for searching and collecting track candidates is specified as the intersection between a cone shape and the plane of the detector. This process is visually represented in Figure 3.5, where the estimated position can be precisely determined.

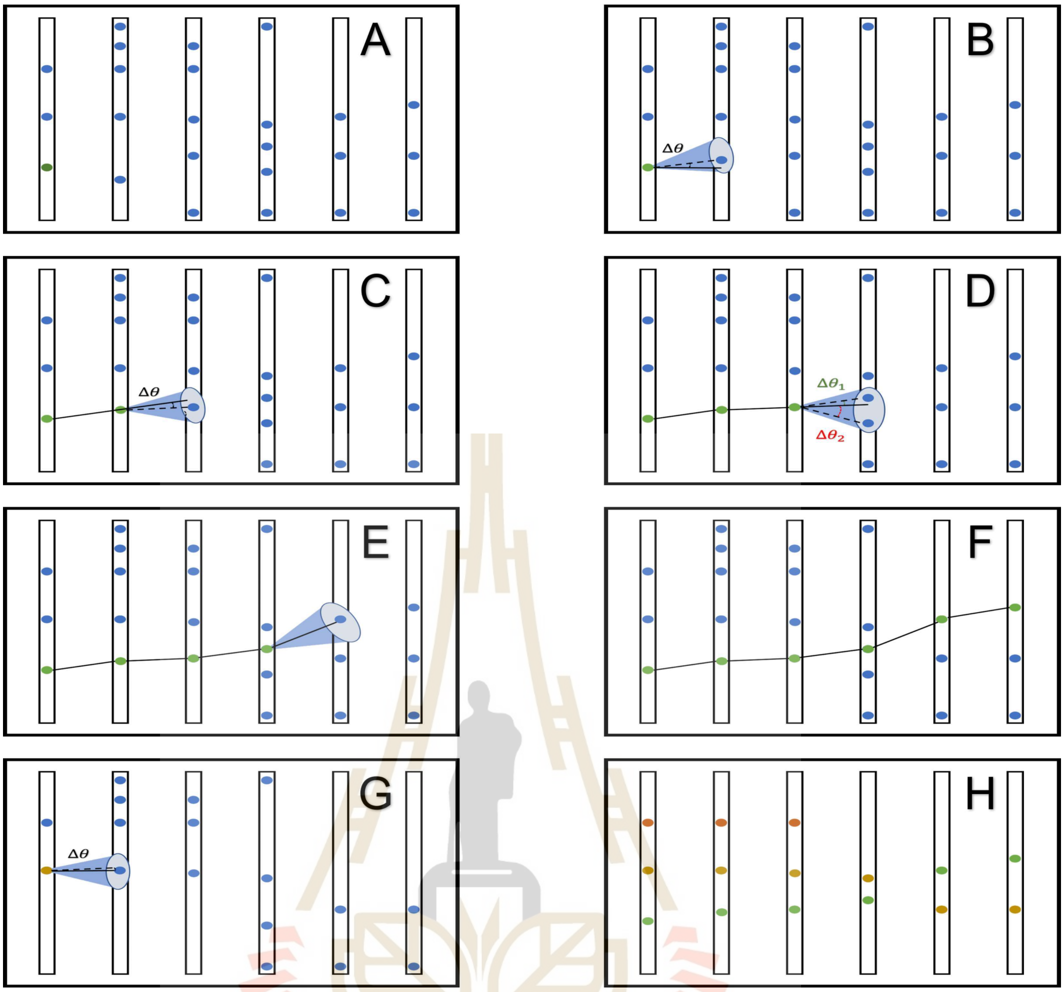

Figure 3.4 The diagram illustrates the sequence of steps in the tracking algorithm. Hits in different layers of the detector are depicted as blue dots. The process begins by selecting the first hit of a track (highlighted in green) from the first layer (A). Next, candidates for the track are searched using a cone defined by S_{max} (B). If the calculated S_n for a new candidate is lower than S_{max}, the hit is added to the track (C). If multiple hits are identified, the candidate with the lowest S_n value is selected (D). These steps are repeated for the subsequent layers (E) until the last layer of the detector is reached (F). Afterward, hits belonging to this track are removed from the pool of hits, and the reconstruction of the next track begins (G). The algorithm continues until all identified tracks are successfully reconstructed (H).

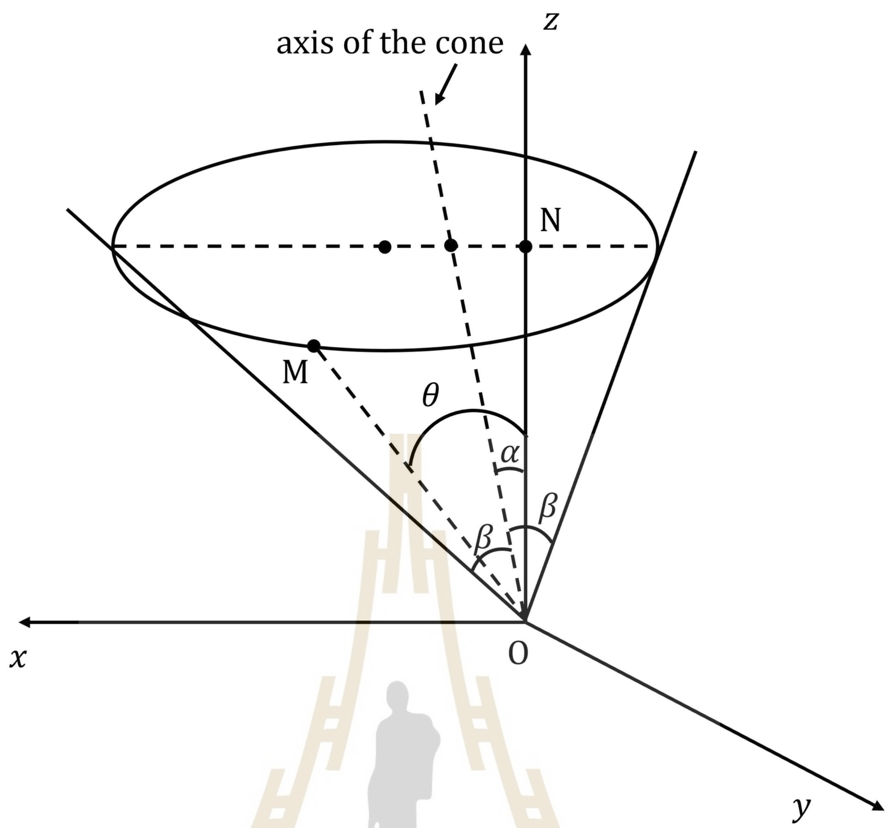

Figure 3.5 The cone intersects C(0,0;α,δ,θ) with a horizontal plane where z > 0, the resulting shape is an ellipse. The major axis of the ellipse aligns with the x-axis, while the minor axis aligns with the y-axis. (Maxim et al., 2009).

$$\begin{cases} x = z\dfrac{\sin\alpha\cos\alpha}{\cos^2\alpha - \sin^2\beta} + \dfrac{\sin\beta\cos\beta}{\cos^2\alpha - \sin^2\beta}\cos\varphi \\ y = z\dfrac{\sin\beta}{\sqrt{\cos^2\alpha - \sin^2\beta}}\sin\varphi \\ z = z \end{cases} \tag{3.1}$$

where:

- z $\geq$ 0 indicates to detector layer

- β corresponds to the the expected proton scattering. The Box-Muller transform

(Box and Muller, 1958) is used to calculate this value, that generated by a standard normal distribution with $\sigma = \theta_0$ from Higland equation (Eq. 3.4) as the equation require the information of material layer described in chapter 3.2.1.

- $\varphi \in [0, 2\pi)$ is represented as the intersection between the cone C(0,0;α, 0,β) and the flat plane including M point.

- α is defined as the angle between previous direction and Oz vector: $\alpha = \cos^{-1}\left(\frac{dz}{x^2 + y^2 + dz^2}\right)$ where dz represented to the gap between layers, in this case, 25 mm.

For the remaining sensor layers, the cone will be denoted as C(0,0;α,σ,β), with σ representing the angle between the major axis of the ellipse and the Ox axis, as depicted in Figure 3.6.

Consequently, x and y of new coordinate system of equation3.1 with cone rotation should be replaced by x' and y' respectively as below.

$$\begin{cases} x' = x\cos\sigma + y\sin\sigma \\ y' = -x\sin\sigma + y\cos\sigma \\ z = z \end{cases} \tag{3.2}$$

A new cone C(0,0;α,σ,β) is computed for every layer to determine the x and y coordinates of the particle at each interaction until the final layer is reached.

Scattering angle

The track reconstruction algorithm, illustrated in Figure 3.4, involves regenerating the search cone each time a new candidate is found. In the algorithm, the S_{max} value remains constant to determine which hits are considered as candidates. The square root of the sum of squared angles between the current hit and the previous hit is calculated as

$$S_n = \sqrt{\Sigma_{layer}^{n}\left(\Delta\theta_{layer}\right)^2}, \tag{3.3}$$

where n is the total number of detector layers, and $\Delta\theta_{layer}$ represents the angle between the track direction on the current layer and previous direction of this track.

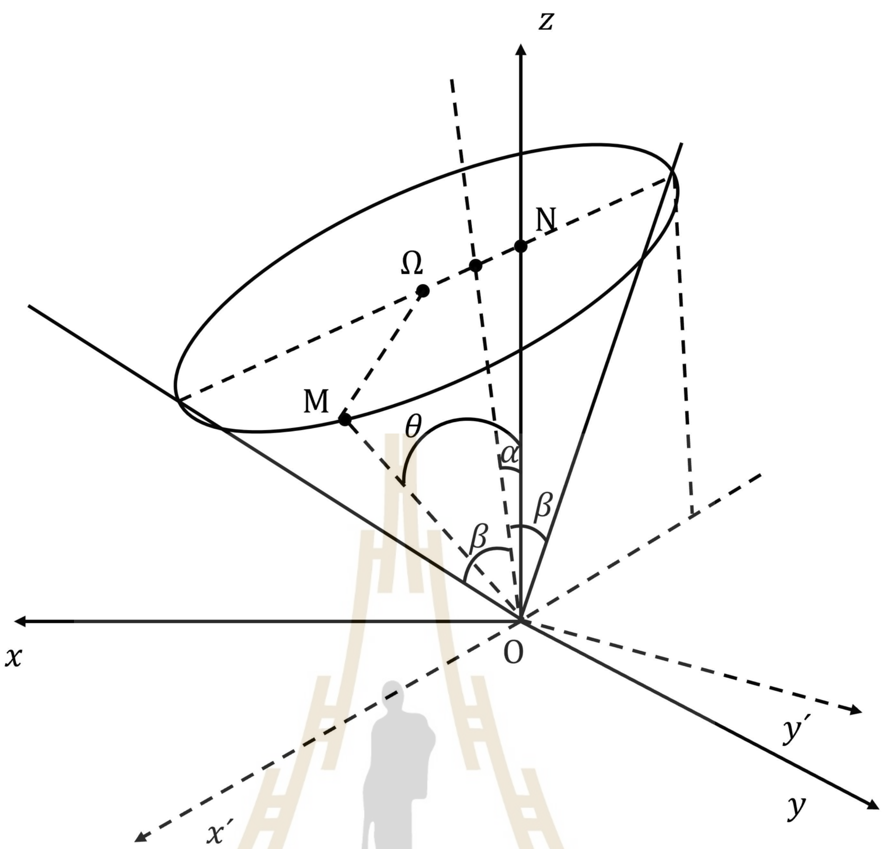

Figure 3.6 The angular parameters, α and σ, define the arbitrary direction of the cone axis, while β represents the cone opening. The intersection between the cone and a horizontal plane with z > 0 forms an ellipse $E(z; \alpha, \sigma, \beta)$. The major axis of the ellipse is inclined at an angle to the 0x axis (Maxim et al., 2009).

According to Equation 3.3, a hit that provides S_n value smaller than S_{max} is account to a track candidates. The $\Delta\theta$ in the track algorithm can be estimated Gaussian approximation by calculating the sigma value of Highland's equation (Highland, 1975) as

$$\sigma_{\theta_0} = \frac{14.1\text{MeV}}{\text{pv}}\sqrt{\frac{\text{x}}{\text{X}_0}}\left(1 + \frac{1}{9}\log_{10}\frac{\text{x}}{\text{X}_0}\right), \quad (3.4)$$

where p is particle momentum, v is particle velocity, X represents material thickness, and X_0 represents radiation length.

Radiation Length

Radiation Length is the distance over which the energy of a high-energy particle is reduced to 1/e (about 37%) of its initial value due to bremsstrahlung. Bremsstrahlung is the electromagnetic radiation emitted by a charged particle when it is accelerated by another charged particle or a nucleus. The radiation length is a material parameter that is affected by the substance that the particle is travelling through. It is denoted as X_0 which is typically calculated using the following equation:

$$X_0 = \frac{716.4A}{z(z+1)\ln\left(\frac{287}{\sqrt{z}}\right)} g/cm^2 \tag{3.5}$$

where A represents the atomic mass of the material and Z represents the atomic number. In high-energy physics research, X_0 is a significant parameter as it determines the amount of energy deposited by a high-energy particle as it traverses a material. Typically, X_0 values for most materials range from millimeters to centimeters. In composite materials, the radiation length can be computed using the following method:

$$\frac{W_0}{X_0} = \sum \frac{W_i}{X_i}, \tag{3.6}$$

where W_0 is total mass of the sample in $g \cdot cm^2$, X_0 is combined radiation length of the sample in $g \cdot cm^2$, and W_i represents radiation length of the individual component in $g \cdot cm^2$.

The ALPIDE sensor is composed of multiple material layers, including aluminum (Al) for the metal layer, silicon (Si) for the epitaxial and substrate layers. Table 3.1 provides the radiation length property for each of these material layers in the ALPIDE sensor (source:http://pdg.lbl.gov/2009/AtomicNuclearProperties/). The radiation length of composite layers can be determined using Equation 3.6. Additionally, the radiation length of the ALPIDE sensor with a thickness of 50 μm can be obtained from the work by (Abelev and ALICE Collaboration, 2014).

Linked list structure

The track reconstruction approach is developed using linked lists for recursion programming and resource conservation in object oriented programming. Each hit data in a sensor layer is linked together as a linked list. The representation of hits data is

Table 3.1 The radiation length of material layers of ALPIDE sensor.

Layer	Material	Thickness (μm)	X_0 (cm)
Metal	Al	11	8.897
Epitaxial	Si	25	9.370
Substrate	Si	64	9.370
ALPIDE	Al + Si	100	9.307
*ALPIDE (50 μm)		50	9.369

referred to as a node. Each node holds the information provided in section 3.2.4 , and additive data is computed for insertion into the hit node. As shown in Figure 3.7, the in-layer linked lists of 6 layers are layered in the detector linked list, which binds the first hit in the current layer to the first of the next layer. The additional information is provided below.

- ID - the unique integer value that is assigned to every hits. In the reconstruction algorithm, the searching process observes every hits at a time. So, the ID is defined to help the search identifying individual hit.

- S_n - the value that is calculated by $S_n = \sqrt{\sum_{\text{layer}}^{n} (\Delta\theta_{\text{layer}})^2}$ to compare with S_{max} value to cut off candidates.

- dvector - the different angle between search cone and the vector of current hit and next hit.

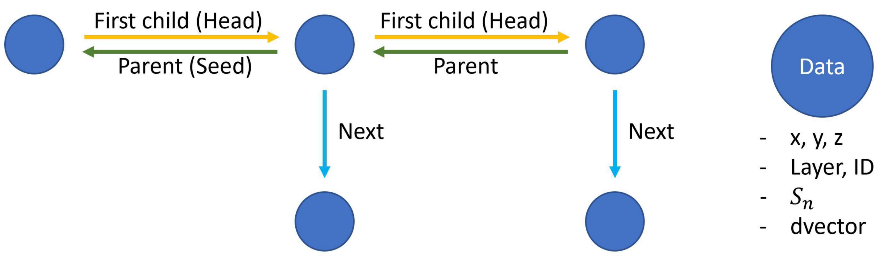

Figure 3.7 The linked list structure of the track reconstruction which used for recursive algorithm and low resources consumption.

The physical location of data pieces in memory is not used to arrange them in a linear collection. Instead, each piece refers to the one preceding it. This data structure is known as a linked list, and it is made up of nodes that form a series. Each node in the sequence carries data as well as a reference (or link) to the next node in the sequence. This structure, in its most basic version, allows for the efficient addition or removal of items from any place in the sequence. More complex forms may incorporate more links, allowing for even faster insertion and removal at arbitrary points.

Track efficiency

In order to assess the effectiveness of reconstructing a charged particle in a Monte Carlo (MC) simulation, the hits generated in the silicon tracker are utilized for track reconstruction. This reconstructed track is then compared with the original track to determine the success of the reconstruction. The overall efficiency is divided into acceptance and reconstruction efficiency for the purpose of this study. Acceptance refers to the probability that a charged particle will produce a sufficient number of hits in the tracker, allowing it to be successfully reconstructed by the track-finding algorithm. On the other hand, reconstruction efficiency measures the probability that these hits will be utilized to accurately reconstruct a track with parameters similar to those of the original particle. Acceptance takes into consideration factors such as detector geometry, material properties, and the performance of the silicon sensors. Efficiency is influenced by the specific track-finding algorithm employed and the hit occupancy, which is affected by the presence of low-momentum particles that are challenging to precisely simulate (CMS, 2010). The track efficiency is calculated as

$$\text{eff} = \mathcal{A} \cdot \epsilon = \frac{N_{\text{reco,iso}}}{N_{\text{gen}}} \cdot \frac{N_{\text{reco,embed}}}{N_{\text{reco,iso}}}, \tag{3.7}$$

where N_{gen} represents the total number of tracks simulated, $N_{\text{reco,iso}}$ represents the count of simulated tracks that are correctly reconstructed, and $N_{\text{reco,embed}}$ represents the count of tracks correctly reconstructed both in the data and the simulation. The primary criterion for determining the successful reconstruction of a track in this study is based on a threshold of 100% hit association between the reconstructed track and the simulated charged particle for the telescope used.

3.3 Results and discussion

3.3.1 Beam profile

As stated in section 3.2.2, the primary source utilized in this simulation consists of Gaussian beams with energy levels of 70 MeV and 200 MeV. As the proton beam travels through the air, it spreads, resulting in an increased sigma spot and modified beam shape. The telescope detector is employed in this simulation to observe the beam profile. The analysis reveals that the size of the beam spot grows at intervals of 2.5 cm between each sensor. The findings presented in this section illustrate the beam profile of both the 70 MeV and 200 MeV pencil proton beams as detected by the telescope detector.

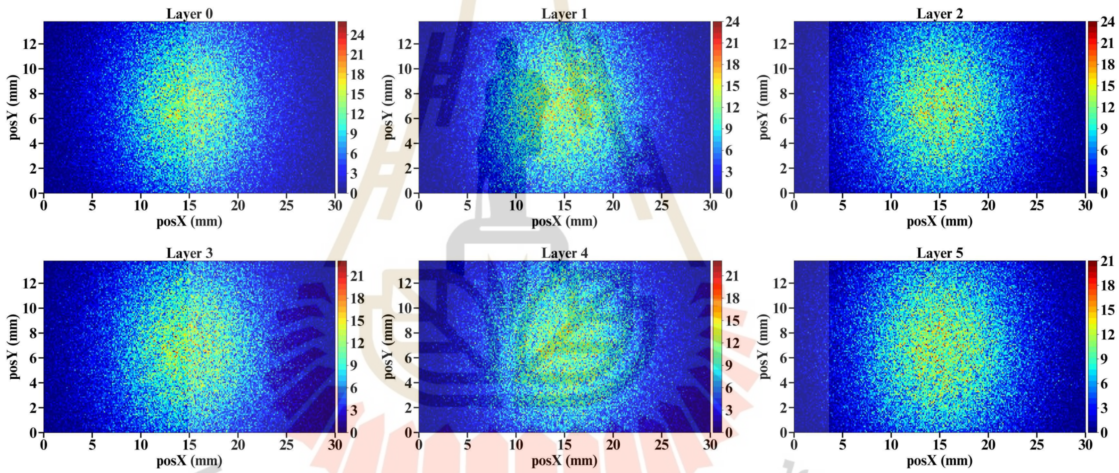

Figure 3.8 The beam profile of 70 MeV pencil proton beam in 200000 events. The color bar of the histogram shows the entries of proton hit on specific point of ALPIDE sensor.

According to figure 3.8 and table 3.2, the spot beam profile of 70 MeV shows that the center of the beam is in the center of every detector layer. The sigma in X direction is comparable to KCMH beam measurement that has described in section 3.3, but the Y axis indicates the inconsistency of sigma because of oversized beam on that axis. So, by using the beam characteristics for modeling beam profile in Gaussian model, the ideal beam profile can be represented as in figure 3.9.

Based on the information provided in Figure 3.10 and Table 3.3, the Gaussian beam profile of 200 MeV beam can be calculated similar to 70 MeV source. But, the

Table 3.2 The simulated beam characteristics of 70 MeV pencil proton beam.

Plane no.	Mean X (mm)	Mean Y (mm)	sigma X (mm)	sigma Y (mm)
0	0.029228	-0.007334	5.498986	3.604242
1	0.030752	-0.009686	5.562324	3.613843
2	0.031516	-0.010166	5.625496	3.620563
3	0.028350	-0.010087	5.692872	3.626612
4	0.027526	-0.009466	5.760172	3.631103
5	0.031726	-0.007003	5.829004	3.636043

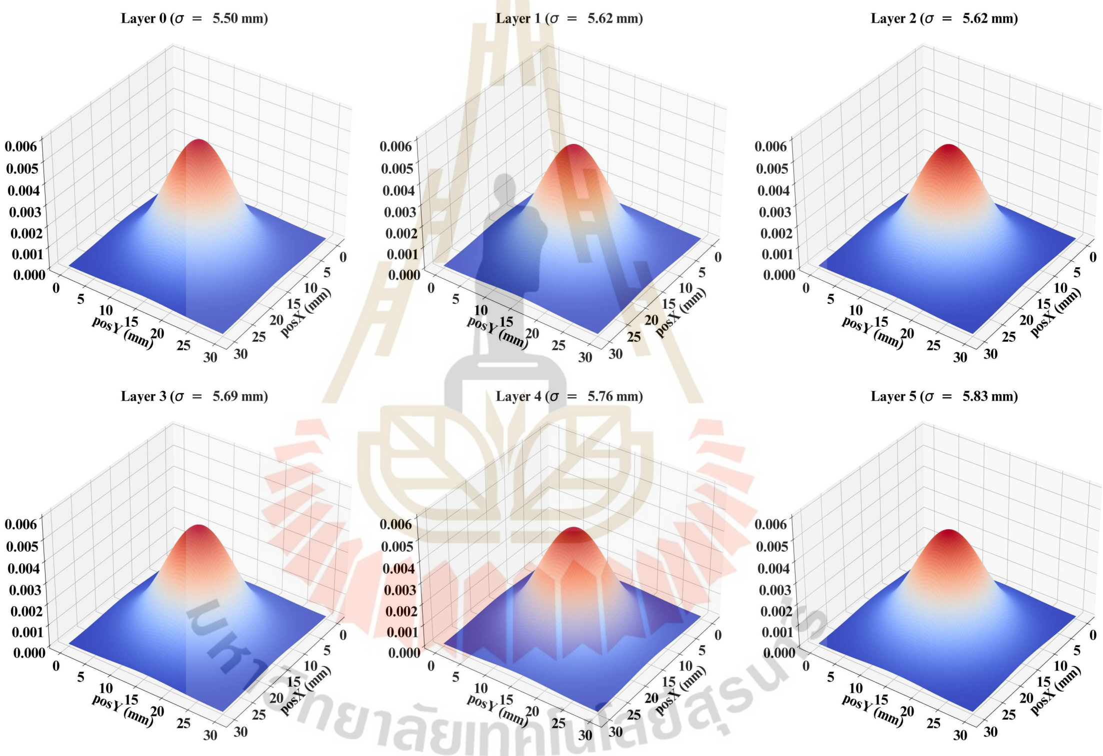

Figure 3.9 The 70 MeV pencil proton beam modeled by Gaussian distribution. The fitting parameters are calculated as shown in Table 3.2.

beam fit of Y axis still mismatch with KCMH data because of losing some hit data in that axis . The ideal beam profile can be represented as shown in Figure 3.11.

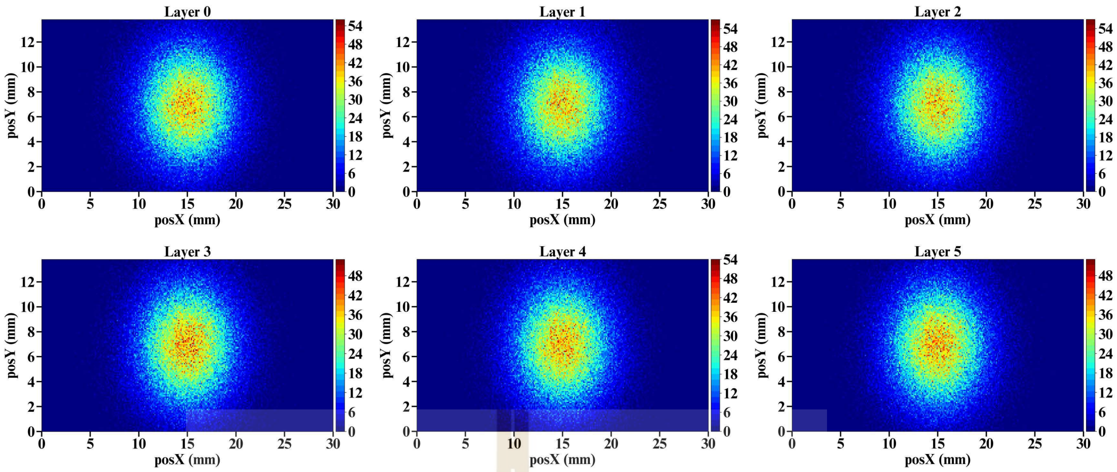

Figure 3.10 The beam profile of 200 MeV pencil proton beam in 200000 events. The color bar of the histogram shows the entries of proton hit on specific point of ALPIDE sensor.

Table 3.3 The simulated beam characteristics of 200 MeV pencil proton beam.

Plane no.	Mean X (mm)	Mean Y (mm)	sigma X (mm)	sigma Y (mm)
0	-0.006722	-0.001962	3.246739	2.919203
1	-0.006517	-0.002003	3.249379	2.920486
2	-0.006570	-0.002322	3.251722	2.921759
3	-0.006691	-0.002437	3.254626	2.922672
4	-0.006516	-0.002126	3.257421	2.923582
5	-0.006387	-0.002503	3.260514	2.924530

3.3.2 Energy deposition

When a high-energy particle travels through a detector, it can cause a chain reaction of secondary particles to deposit energy in the detection material. Physicists can reconstruct the energy and momentum of the original particle by measuring the total energy deposited in the detector. The proton energy source can deposit energy into the material it passes through, as well as secondary particles formed by the interaction of the primary source with matter. The simulation helps to determine the deposited energy in each epitaxial layer of each ALPIDE plane.

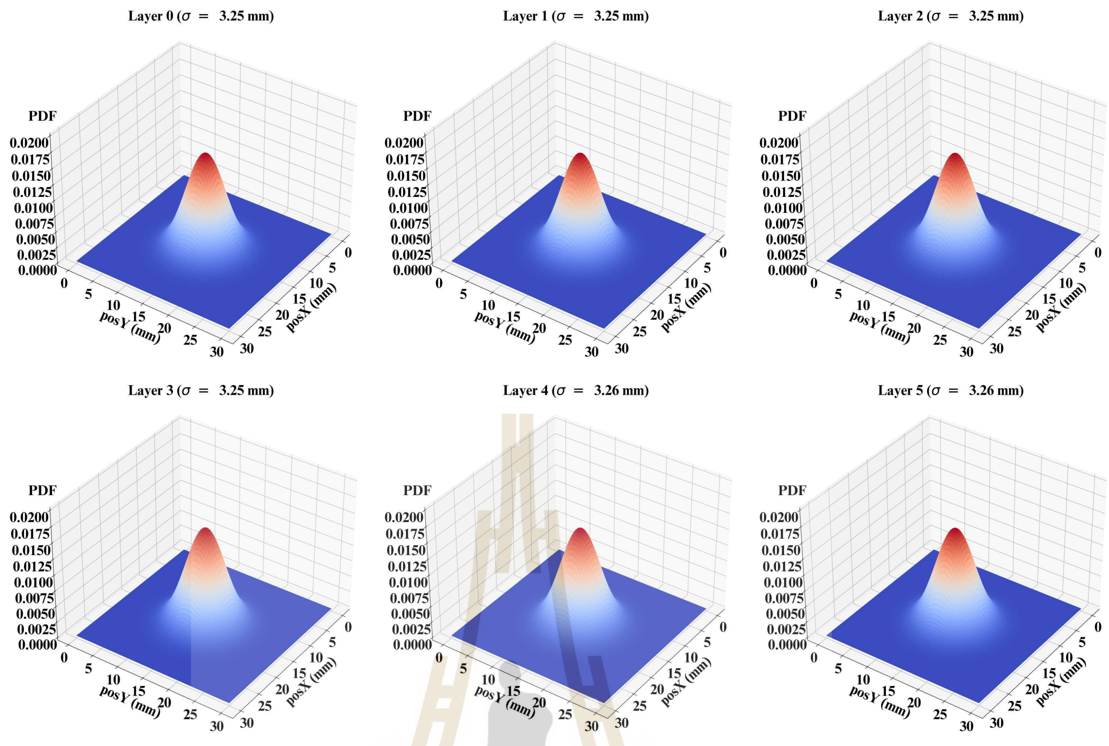

Figure 3.11 The 200 MeV pencil proton beam modeled by Gaussian distribution. The fitting parameters are calculated as shown in Table 3.3.

The deposited energy of protons in the epitaxial layer is determined in the same way as shown in Section 3.2.1. Ionisation of deposited energy produces electron-hole pairs in the epitaxial layer. Electrons move from the valence band to the conduction band, and holes move from the conduction band to the valence band. The phenomena is exploited to create an electrical signal. The number of electron-hole pairs is gathered as an active pixel signal in the ALPIDE sensor, and related to the energy deposition in the epitaxial layer.

In the simulations, pencil proton beams with energies of 70 and 200 MeV are defined as the simulation sources. The pencil proton beam passes through the ALPIDE sensor while transferring some energy to the material layers. Secondary particle creation can occur, and the material layers can receive some deposited energy from those secondary particles. As a result, only proton particle energy deposition is seen using filter Tree hit data with parentID 0 as indicated in Section 3.2.4.

The distribution of energy deposition in each detector plane is similar in both

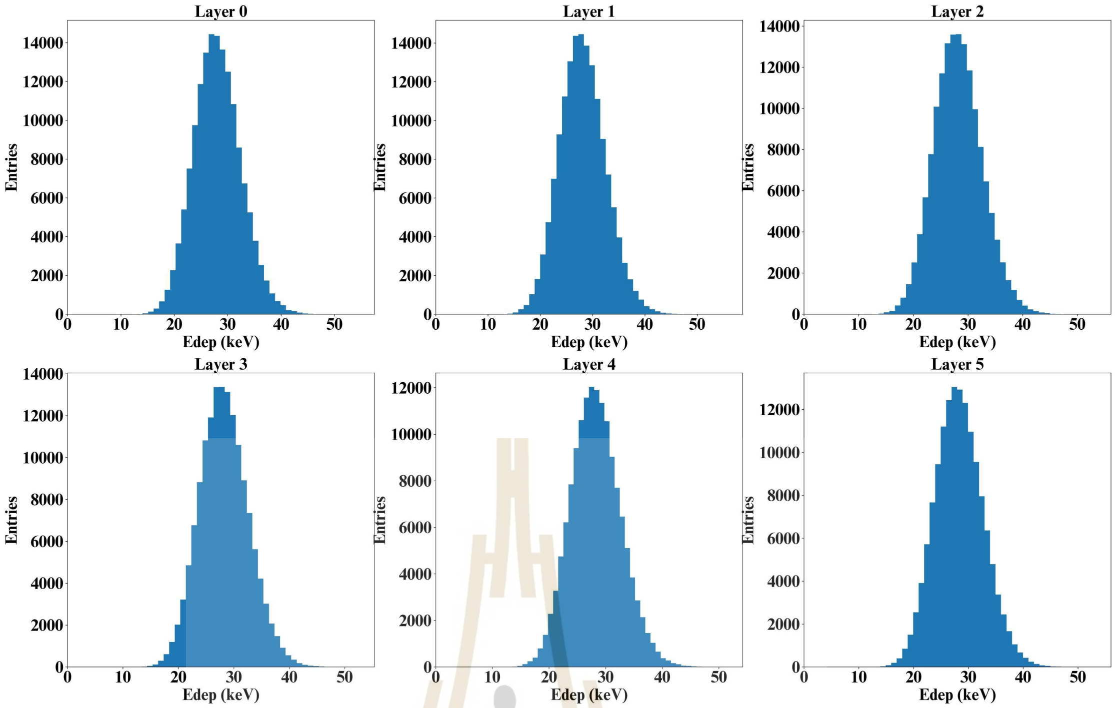

Figure 3.12 The distribution of proton energy deposition in epitaxial layer of ALPIDE sensor with 70 MeV pencil beam source

Table 3.4 The mean and standard deviation (sigma) of proton particles deposit energy in epitaxial layer of ALPIDE sensor.

Plane no.	70 MeV		200 MeV	
	Mean (KeV)	Sigma (keV)	Mean (keV)	Sigma (keV)
0	28.0	4.39	13.0	2.96
1	28.1	4.38	13.0	2.95
2	28.2	4.40	13.0	2.94
3	28.3	4.39	13.0	2.95
4	28.3	4.40	13.0	2.95
5	28.3	4.40	13.0	2.94

70 MeV and 200 MeV, according to Table 3.4. For six ALPIDEs, the average means of deposit energy in epitaxial layer for 70 MeV and 200 MeV proton beams are 28.2 keV and 13.0 keV, and their average sigmas are 4.39 keV and 2.95 keV, respectively. The results reveal that energy deposition is affected by the energy of the beam source.

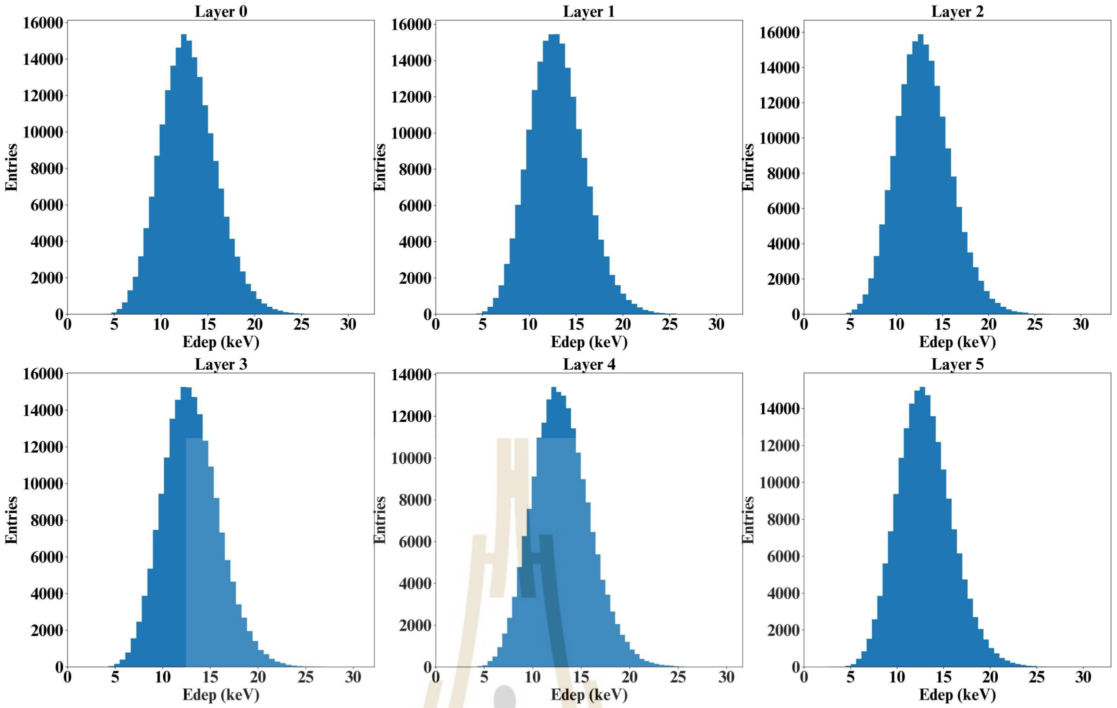

Figure 3.13 The distribution of proton energy deposition in epitaxial layer of ALPIDE sensor with 200 MeV pencil beam source

Lower energy has a higher likelihood of being absorbed by the sensor than high energy. Furthermore, the quantity of energy absorbed in the epitaxial layer reflects the size of the cluster, which is a group of activated pixel neighbors, as mentioned in section 5.4.2.

3.3.3 Proton track

When a charged particle passes through a detector, a trail of ionization or radiation is left behind, it can be picked up and recorded as a series of discrete points or hits. By combining these points or hits, one can determine its trajectory. In addition, a charged particle can also interact with the atomic nuclei or electrons inside the medium, causing its route to deviate from the incoming direction. The magnitude of the deviation is determined by charge and mass of the particle, as well as parameters of the material such as density and thickness.

The simulation data is converted into three-dimensional information for each sensor plane. To be identical with the experimental setup, the beam energies utilized in the simulation for reconstructing the track are 70 MeV and 200 MeV as described in Section 3.2.2. The reconstruction algorithm will search for hits and connect them together to form the path. Because the exact track is collected along with the output data in MC simulation, the comparison between the MC track and reconstructed tracks implies the track reconstruction efficiency of this algorithm and can demonstrate the possibility of using this algorithm in the real experiment shown in chapter V. Three-dimensional hit data from simulations of 70 MeV and 200 MeV are given in Figure 3.14.

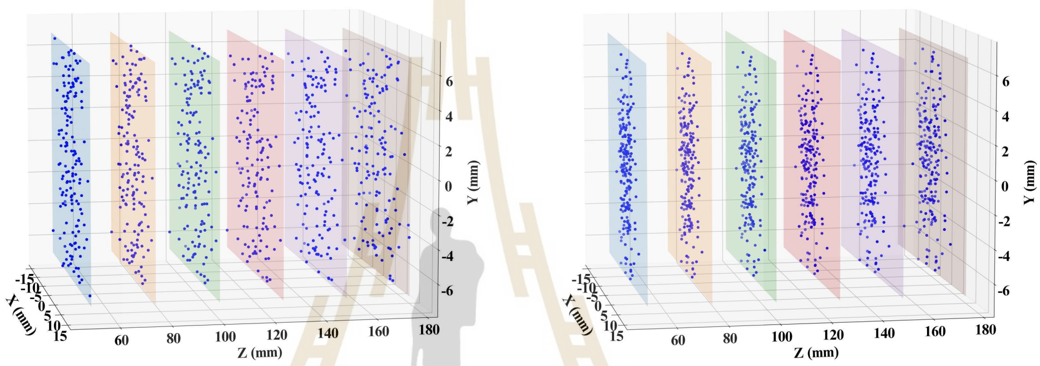

(a) 70 MeV. (b) 200 MeV.

Figure 3.14 3D hit data of simulations.

The track algorithm as described in Section 3.2.5 is applied to 3D hit data of both 70 MeV and 200 MeV. The S_{max} parameter is optimised by observing track efficiency on various primary events used in the simulation. The $\Delta\theta$ value, that is varied to determine the efficiency, is also compared to the σ_{θ_0} from Equation 3.4. According to the pCT prototype of the Loma Linda (Giacometti et al., 2017), the number of protons which are detected by detector per frame are required about 100 protons/frame in 1 cm^2 of sensor area. As reported by ALPIDE sensor area, the active space is 1.38 $\times$ 3.0 cm^2. So 400 primaries are evaluated in track reconstruction of the simulation part.

Figure 3.15 shows the track efficiency of 400 proton particles utilized in GATE/GEANT4 simulation using track efficiency equation 3.7, using 70 MeV and 200 MeV as energy sources. The S_{max} of 70 MeV and 200 MeV enable high efficiency of 80% and 100%, respectively, with a purity of 75%. In high efficiency zones, the cone angles for 70 MeV, and 200 MeV are 10 mrad and 1.5 mrad, respectively. The σ_{θ_0} is calculated using Equation 3.4 and the radiation length values from Table 3.1 of Al + Si materials of single ALPIDE. The figure also demonstrates that at 70 MeV, about $5\sigma_{\theta_0}$ gives great track efficiency and $2\sigma_{\theta_0}$ at 200 MeV.

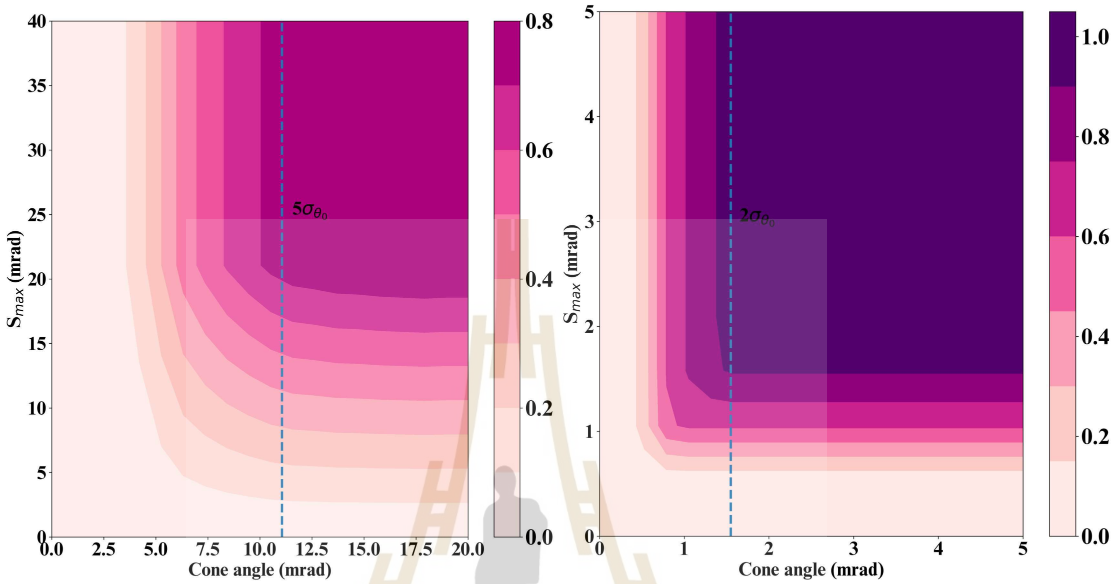

(a) 70 MeV.　　(b) 200 MeV.

Figure 3.15 The contour plot of track efficiency on various S_{max} and cone angle. The color bar of these plots show the reconstruction efficiency of tracking algorithm.

Figure 3.14 shows hit data visualization as 3D visualization. Figure 3.16 displays the track reconstruction result as a track path. The S_{max} and cone angle parameters utilized in the track reconstruction algorithm are taken from Figure 3.15 as 25 mrad of S_{max} and 11 mrad of cone angle for 70 MeV, and 2.0 mrad and 1.5 mrad, respectively, for 200 MeV. As a consequence, all proton tracks from the method applied to 400 simulated primaries are shown. Because the purity is set to 75%, some tracks do not connect candidates as six levels.

Instead of evaluating proton track efficiency based on the search cone angle and S_{max}, track efficiency can be thought of as the number of primary dependencies used in the simulation. The simulation in this section serves as a guideline for the experimental setup, and the simulation results can be used to uncover some requirements. Figure 3.17 depicts the track efficiency at 70 MeV and 200 MeV with different main numbers. When the primary is reduced to 70 MeV, the accuracy rapidly decreases. On the other hand, efficiency is declining slowly.

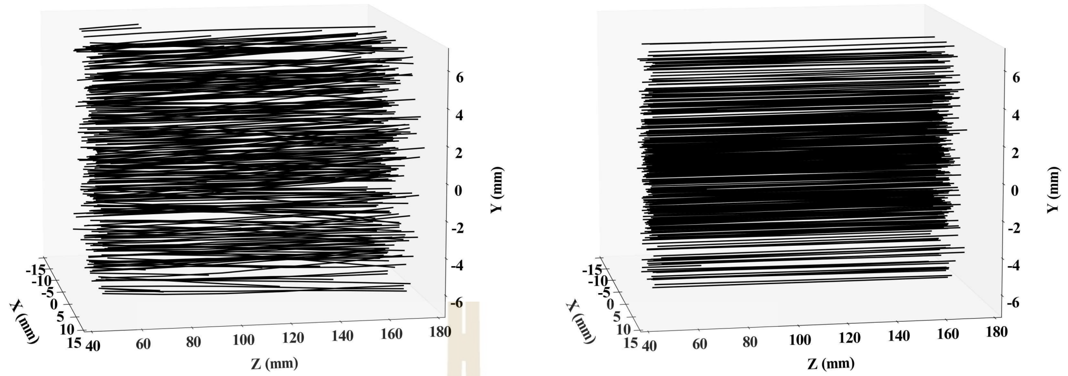

(a) 70 MeV. (b) 200 MeV.

Figure 3.16 GATE/GEANT4 simulation of 400 primary proton track routes. The tracks connect all candidates from layer 0 to the last layer, in which the last candidates of each track are discovered.

3.4 Summary

The simulation part evaluates the algorithm quality of the track reconstruction when applied to 3D hit data from Monte Carlo simulation. The geometry of the simulation model is based on an actual experiment conducted using an operating therapeutic proton beam at King Chulalongkorn Memorial Hospital (KCMH) in Thailand. Pencil Beam Scanning (PBS) is the beam, which can be represented by a two-dimensional Gaussian model. The simulation employs two beam energies. The lowest energy that can be irradiated from the KCMH cyclotron is 70 MeV, and the highest energy that can be evaluated by the transmission process is 200 MeV. For the test, 400 primaries are irradiated to the telescope. The epitaxial layer determines the deposited energy that causes the signal in a sensor. The electron-hole pairs are ionized by the absorbed energy in the material and produce the electrical signal. These signals can be represented as 3D hit data of particles striking a surface. Filtering only proton primary with parentID 0 from Tree hits in the root data file removes the secondary particles. The track efficiencies are estimated based on S_{max} and search cone angle of the reconstruction algorithm. Thus, the track following algorithm performs well in simulation at 20 mrad of S_{max} and

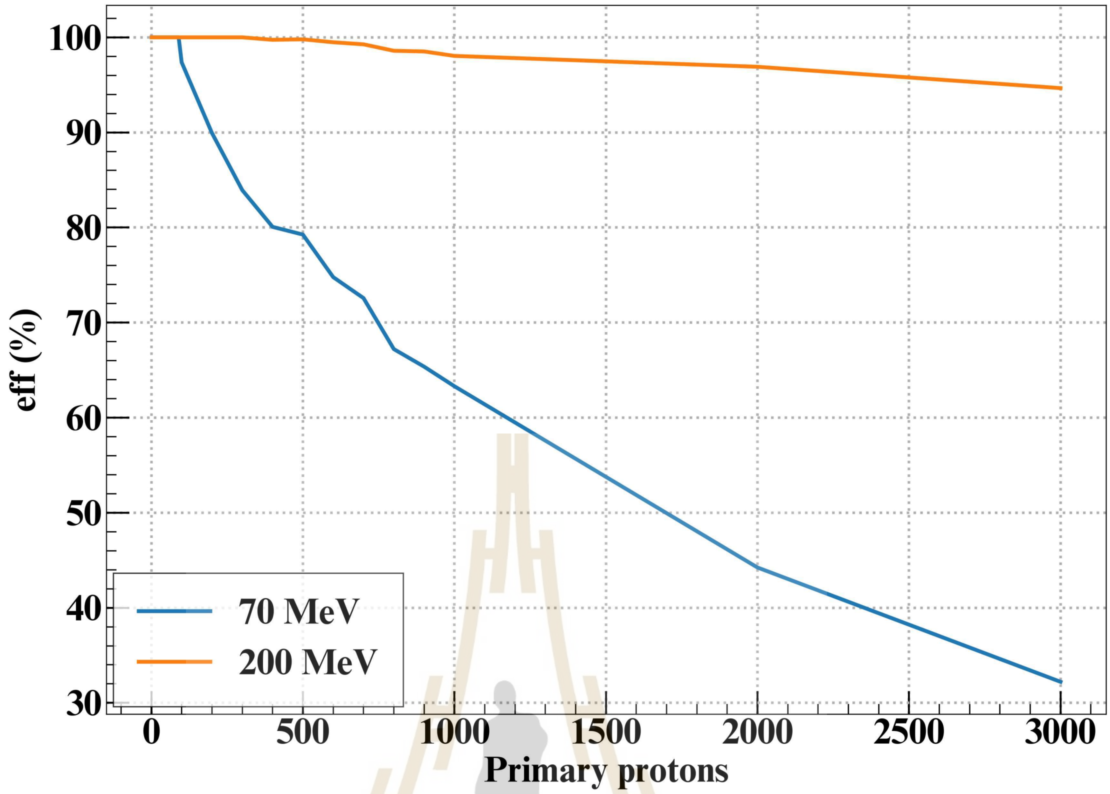

Figure 3.17 The track efficiency for proton sources at 70MeV and 200MeV depends on the number of primary protons employed in the GATE/GEANT4 simulation.

10 mrad of cone angle in 70 MeV and 1.5 mrad of S_{max} and 1.5 mrad of cone angle in 200 MeV. With the σ_{θ_0} calculation from Equation 3.4, the track efficiencies reveal that higher energy has more accurate track reconstruction than lower energy, and the S_{max} and cone angle values are narrower than 70 MeV when compared to σ_{θ_0} values of 200 MeV. Finally, when the number of primary factors affecting track efficiency is seen, a high intensity of the source implies a low efficiency.

CHAPTER IV

PRELIMINARY: THE FPGA TRIGGER CONTROL SYSTEM INTERFACING THE TELESCOPE WITH KCMH BEAM TEST

This chapter describes the telescope construction utilized in the KCMH experiment. It is made up of six ALPIDE monolithic active pixel sensors. The EUDAQ framework is responsible for the telescope's control and data collection. The output data is in the form of a binary or raw file. The purpose of this chapter is to give preliminary results of the KCMH proton beam test with the telescope utilized at SLRI for electron beam testing. This chapter also includes the development of a novel trigger system for sending an external signal for EUDAQ run.

4.1 Introduction

ALICE's inner tracking system (ITS) currently consists of seven layers of Monolithic Active Pixel Sensors centered as a cylinder. By testing the six-plane telescope, we want to determine the treatment proton beam profile. The geometry configuration is comparable to the electron beam test at SLRI, and it includes a new trigger system. The experiment demonstrates proton detection and indicates the best telescope for the pCT prototype.

The telescope's sensor section, which is made up of six ALPIDE planes, can detect particle hits. These 512x1024 pixels serve as an active area for the generation of electronic signals. By collecting numerous frames of hit data, the signal can be quantified as a stack of proton hit signals. The detector must deliver low intensity per frame based on the readout rate of a typical pCT. As previously stated, the excessive number of primary particles used in the track reconstruction technique results in low track efficiency. To make the experiment as similar to the pCT system as possible, we built a module that controls the behavior of ALPIDE sensors in the telescope by sending a signal to a DAQ board linked to the sensor.

4.2 Material and method

4.2.1 Pixel sensor telescope

The majority of ALPIDE prototypes are tested using charged particles with several beam test facilities including CERN (Mager, 2016). In general, a pixel sensor telescope, which consists of seven planes of ALPIDE sensors positioned perpendicular to the particle stream, is used in the measuring setup with one Device Under Test (DUT) placed in the middle (Kaewjai et al., 2019). However, our telescope is made up of six sensor planes, five reference planes, and one Device Under Test (DUT). As illustrated in Figure 4.1, the pixel sensor telescope was situated in the KCMH experiment for sensor evaluating the track reconstruction of the PBS proton beam.

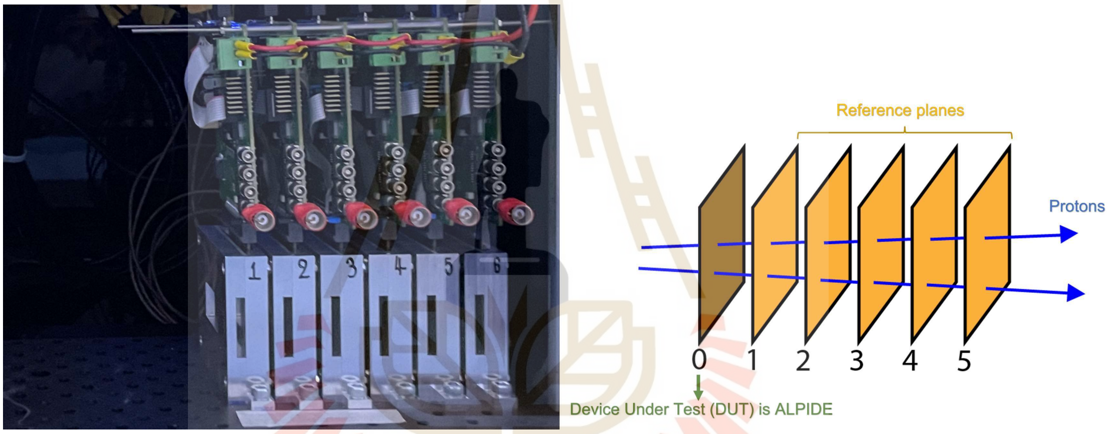

(a) Telescope construction. (b) Telescope layout.

Figure 4.1 The pixel sensors telescope which consists of six ALPIDE sensor and DAQ boards. (a) Each DAQ connects to single ALPIDE chip and wired to external trigger signal and the power. (b) The DUT is set to the layer 0 and the rest are references.

4.2.2 ALPIDE Monolithic Active Pixel Sensor

The pixel matrix and related readout circuits are integrated on a single substrate in a monolithic active pixel sensor (MAPS). This functionality enables MAPS to have greater granularity while using less power. Peripheral circuitry and power supply can also be simplified for MAPS (Abelev and ALICE Collaboration, 2014). Prior to 2006, the European Detector Research and Development towards the International Linear Collider (EUDET) collaboration proposed using MAPS as a sensor plane in the construction of a new generation of high-precision beam telescopes (Haas, 2006). The pixel telescope can benefit from MAPS's outstanding spatial resolution, low material budget, quick readout time, and suitable sensitive area size. The Minimal Ionizing MOS Active sensor (MIMOSA) is used in the construction of EUDET-type telescopes (Hu-Guo et al., 2010). A series of EUDET-type telescopes is in operation around the world, including Advanced European Infrastructures for Detectors at Accelerators at CERN, DATURA and DURANTA at DESY, CALADIUM at the Stanford Linear Accelerator Center (SLAC), and others (Jansen et al., 2016).

ALPIDE is a 1.5×3.0 cm^2 MAPS that reads in binary hit/no-hit mode 512×1024 (row $\times$ column) 28×28 pixels. It combines a continuously active and low-power in-pixel discriminating front-end with a fully asynchronous, hit-driven combining circuit (Mager, 2016). As demonstrated in Figure 4.2, analog biasing, control, readout, and connectivity operations are implemented on a 1.2×30 mm^2 peripheral region (Aglieri Rinella, 2017).

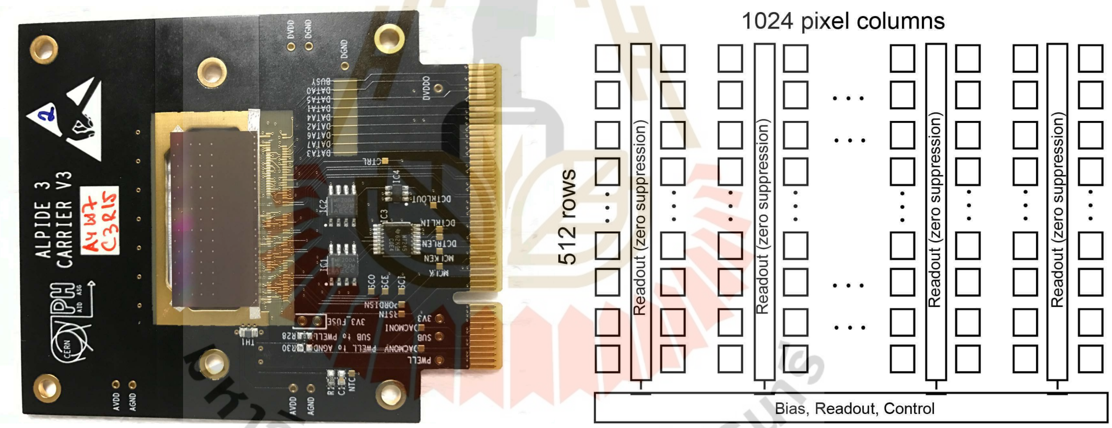

(a) Single ALPIDE chip. (b) Architecture of the ALPIDE chip.

Figure 4.2 The monolithic active pixel sensor ALPIDE.

4.2.3 EUDAQ framework

The Electronic Universal Data Acquisition (EUDAQ) framework is primarily based on the trigger trigger logic unit (TLU). The framework's many modules can run on separate machines and communicate with one another via an Ethernet network utilizing TCP/IP connections. This provides for more flexible DAQ network architecture, which is especially useful for test beams where detectors and users may change often.

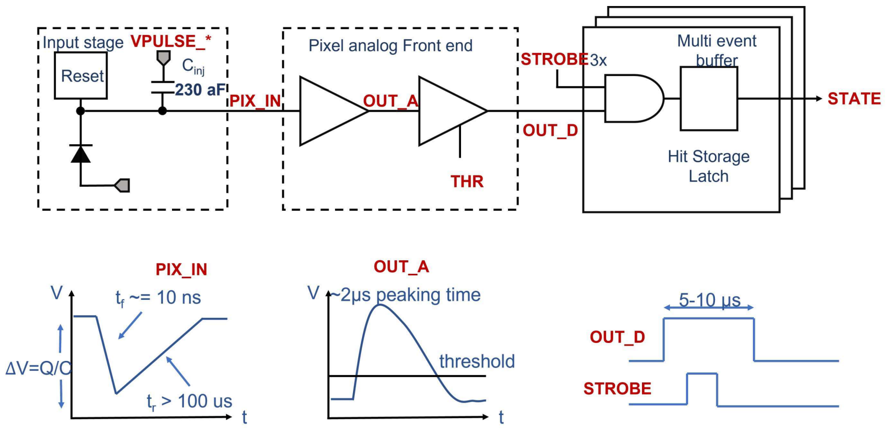

Figure 4.3 Block diagram of the ALPIDE pixel cell.

A typical EUDAQ network is depicted in Figure 4.4. To begin, the EUDET TLU (Cussans, 2009) was employed in conjunction with renowned EUDAQ for the DAQ of EUDET-type Mimosa26 sensing telescopes (Jansen et al., 2016; Hu-Guo et al., 2010).

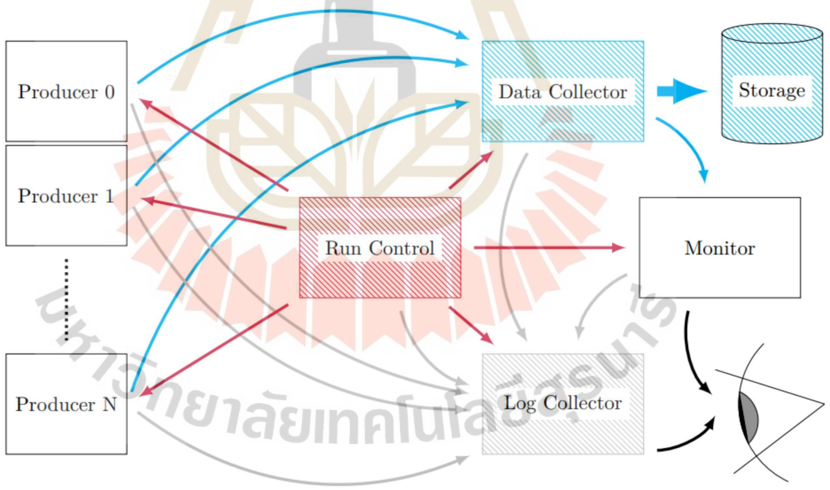

Figure 4.4 The EUDAQ network typically consists of several components, including the central command and control server known as Run Control, the Data Collector, which is responsible for creating global events and storing them on disk, the Log Collector, which manages and displays log messages, and the monitor application, which allows for real-time monitoring of data quality (Spannagel, 2016).

The EUDAQ version 2 is used in this work. The firmware must be installed in the Data acquisition (DAQ) board that contains the Field programmable gate array (FPGA) chip over USB. The configuration files are edited to match the experiment setup, such as the number of sensors, output file path, ALPIDE characteristics, and so on. The Terminal Multiplexer (TMUX) is used to execute the EUDAQ Graphical user interface (GUI) process while waiting for the signal from the trigger to initiate the execute. The GUI interface needs the user to enter the frequency as well as the optional HIGH/LOW signal per pulse. As illustrated in Figure 4.5, the microcontroller accepts the serial signal from the interface and stores user input in another FPGA register for creating a trigger signal to the DAQ.

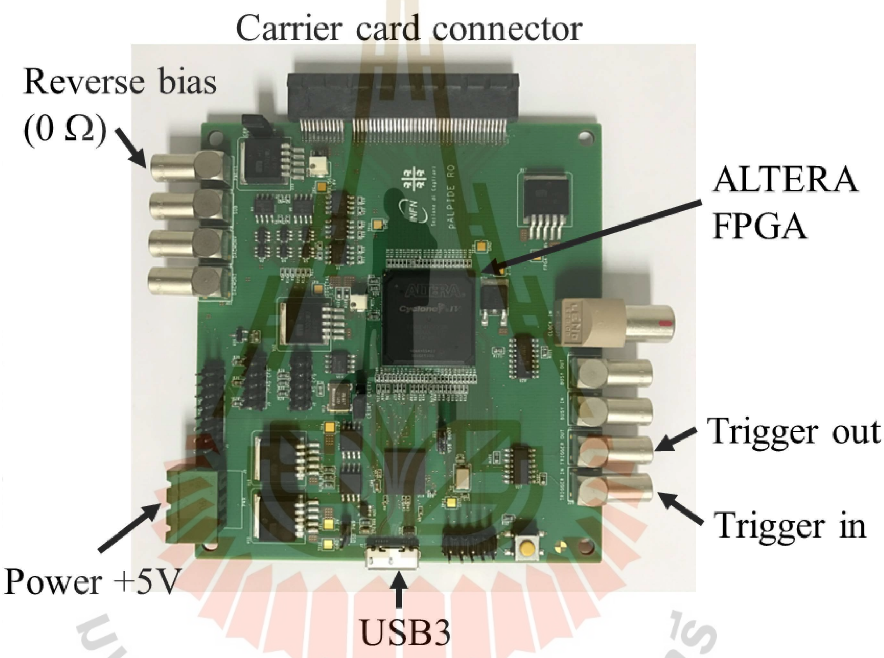

Figure 4.5 This figure shows a board for data collecting. The external signal from the trigger system is received through the trigger-in port. The same signal is used as an output in the trigger-out. The Alterla FPGA is included in the board and is used to operate the EUDAQv2 firmware.

4.2.4 FPGA trigger system

Typically, the EUDAQ architecture collects data from DAQs event by event using an external signal from the trigger system. The square wave signal is ideal for DAQ trigger-in port input. The first generation trigger may also activate telescope DAQs and open the proton beam gate of the KCMH cyclotron. It is constructed with a microcontroller (Arduino) to provide pulses to DAQs and a signal to the KCMH trigger system in the control room in order to operate a proton beam in patient mode. The frequency is approximately 0.2 kHz, which is generated using counting loop logic in C++ Arduino code. The FPGA trigger was constructed with a 100 MHz clock speed to achieve a more reliable and high-speed frequency. The system was designed to be installed in a treatment room and wired with telescopic DAQs because the system's function is to handle only Quality Assurance (QA) mode. The pCT telescope is used in this chapter to measure the QA mode of the KCMH proton beam using an FPGA trigger.

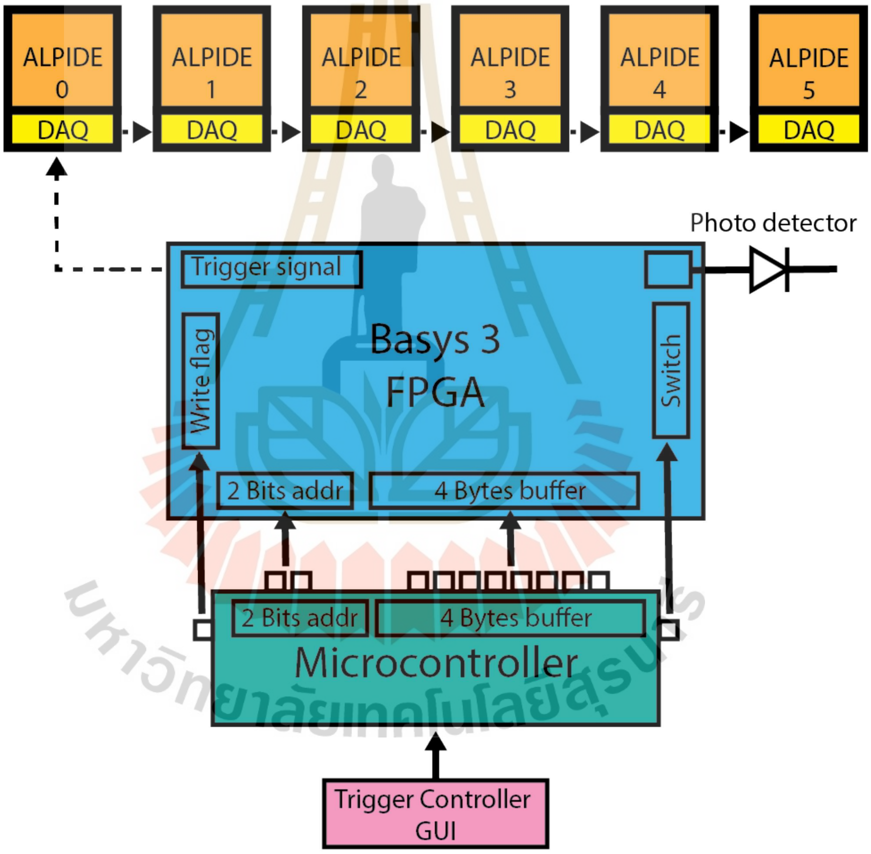

Figure 4.6 The trigger control system scheme for FPGAs. The GUI accepts frequency values from the user. The microcontroller converts frequency to a binary value and sends it to the FPGA along with the register address. Finally, the FPGA sends a trigger signal to the ALPIDEs through the DAQ board.

As seen in Figure 4.6, the GUI communicates with the microcontroller through serial port. The microcontroller converts the frequency to binary and sends it to the FPGA through the buffer address. The GUI can also allow the FPGA to register data and wait signals from the GUI ON signal. The GUI ON signal will activate the FPGA by turning on the Switch flag in the FPGA, indicating that it is ready to generate a trigger signal to the DAQ.

4.2.5 The first generation of trigger

The trigger controller system was designed using the MEGA2560 pro mini as the microcontroller unit. It was linked to the SAMKOON SK-070FE HMI touchscreen through the Universal Asynchronous Receiver/Transmitter (UART) to provide a graphical user interface. The controller's communication used the Modbus protocol via a C language software to send signals to each component. The functionality of the pCT trigger controller was tested by sending programmed signals to the rotational stage and ALPIDE sensor, which were linked to the proton cyclotron at the King Chulalongkorn Memorial Hospital (KCMH) Proton Center for controlling the timing of the proton beam gating. The results showed that the pCT trigger controller was capable of controlling the gating of the proton cyclotron as well as communicating with an ALPIDE sensor for detecting and recording proton positions. At this stage, only one ALPIDE sensor was intended to be employed for testing as the position-sensitive detector.

4.2.6 Basys3 FPGA

Basys3 is created by Digilent Inc. which is a usable digital circuit based on Artix®-7, a Xilinx® Field Programmable Gate Array (FPGA) (XC7A35T1CPG236C). The Basys 3 is compatible with Xilinx's sophisticated Vivado^{TM} Design Suite, which includes a variety of unique tools and design workflows that support cutting-edge design methods. Vivado is more efficient, makes better use of FPGA resources, and allows designers to spend more time investigating design choices. The System Edition (SE) includes an on-chip logic analyzer, a high-level synthesis tool, and other cutting-edge features, but the free WebPACK^{TM} edition allows Basys 3 designs to be created without incurring any additional fees (Xilinx, 2017). Table 4.1 describes the Basys 3 components labeled in Figure 4.7.

The voltage regulator circuits in Linear Technology create the necessary 3.3V, 1.8V, and 1.0V power supplies from the primary power input. In the trigger system, the Pmod component is interfaced with a 3.3V microcontroller through Pmod pins. The 100

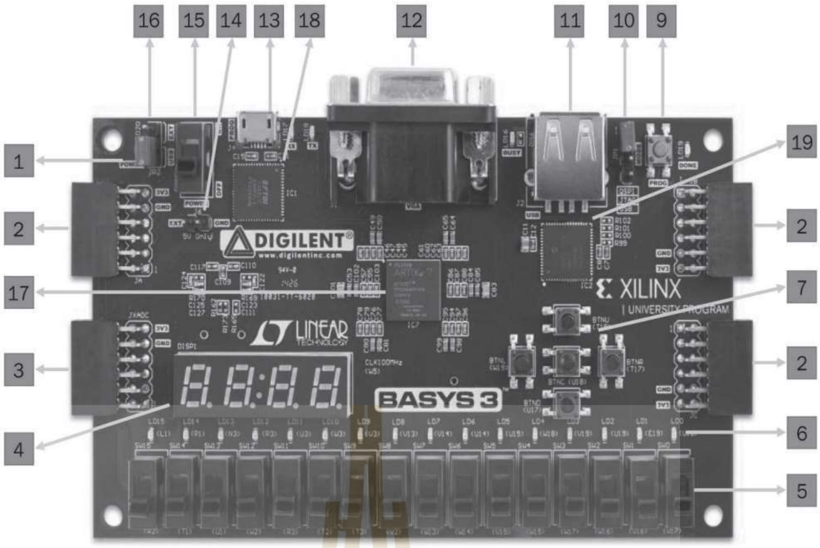

Figure 4.7 The Basys3 board layout and labels

Table 4.1 Basys 3 labeled components and descriptions.

No.	description	No.	description
1	Power good LED	9	FPGA configuration reset button
2	Pmod port(s)	10	Programming mode jumper
3	Analog signal Pmod port (XADC)	11	USB host connector
4	Four digit 7-segment display	12	VGA connector
5	Slide switches (16)	13	Shared UART/ JTAG USB port
6	LEDs (16)	14	External power connector
7	Pushbuttons (5)	15	Power Switch
8	FPGA programming done LED	16	Power Select Jumper

MHz clock from the Basys 3 oscillator, which is linked to pin W5, is divided by Resistor Transistor Logic (RTL) to generate a trigger signal for the DAQ board.

4.2.7 Signal amplification

The standard voltage levels of the Basys3 FPGA, according to section 4.2.6, are 3.3V, 1.8V, and 1.0V. The DAQ board, on the other hand, requires 5V to generate the run event for the EUDAQv2 run control. In this work, the IC SN74HC08N Quad 2-

input AND gate (DIP) was coupled to a trigger signal created by an FPGA as an input AND gate. Voltage Common Collector (VCC) provides another input, and the amplified trigger pulse is obtained from the output of two inputs.

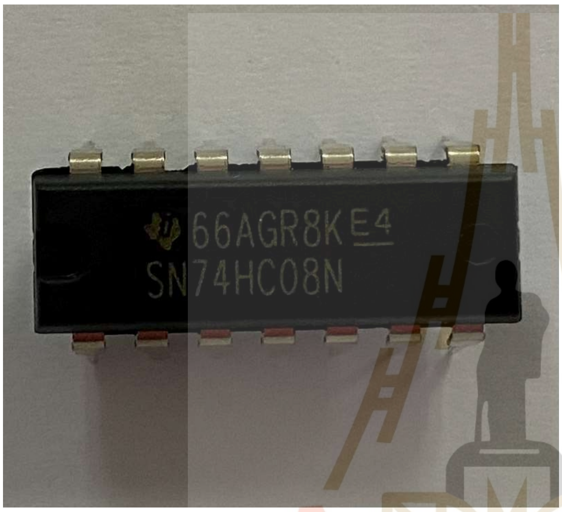

(a) SN74HC08N IC component.

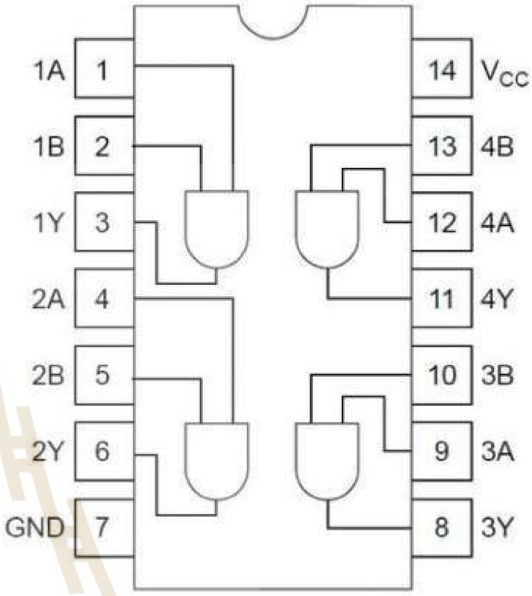

(b) The AND logics of SN74HC08N IC.

Figure 4.8 SN74HC08N.

4.2.8 Microcontroller

Section 4.2.6 states that the operational voltage levels that can be coupled with the FPGA portion are 3.3V, 1.8V, and 1.0V. In contrast, the most popular Microcontroller board, the Arduino Uno R3, operates at 5.0V, which can damage FPGA boards if they are coupled. As a result, by using Logical Voltage Conversion 3.3V-5V, the Uno R3 can be safely linked. Fortunately, there is a 3.3V Arduino board named the Arduino Pro Mini 328 - 3.3V/8MHz. It has an 8MHz clock speed and no USB programmable port. As shown in Figure 4.9, the Pro Mini 328 must connect Data Terminal Ready (DTR), Transmit Data (TXO), Receive Data (RXI), VCC, and ground connector to USB CH340 in order to program the board with Arduino Integrated Development Environment (IDE).

Analog and digital pins are directly wired to Basys3 FPGA. From the Table 4.2,

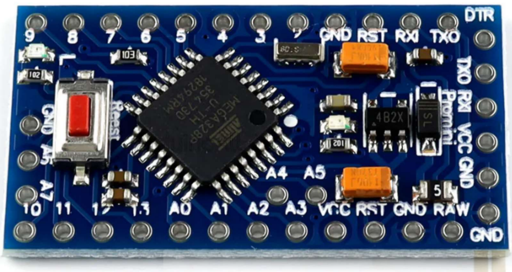

(a) Pro Mini 328(3.3V/8MHz).

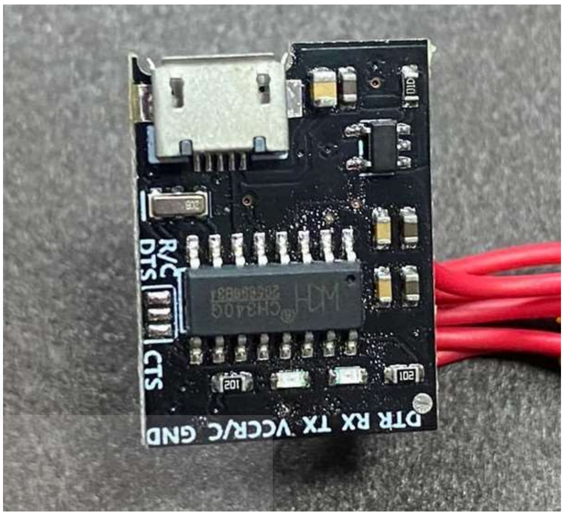

(b) USB CH340 module.

Figure 4.9 The microcontroller part that consists of Pro Mini 328 board and USB programming module.

the Pro Mini 328 pins used for the connection are shown. The write flag means the signal that allow binary data from Arduino transferred to FPGA along its bits address. The switch flag is ON when the FPGA is ready to generate the trigger signal to the DAQ.

Table 4.2 Arduino Pro Mini 3.3V (3.3V/8MHz) pins connecting to Basys3 FPGA and the usages.

Pro Mini pins	Basys3 pins	Usage
2 - 9	K3, J3, M3, L3, M1, M2, N1, N2	8 bits data
10 - 11	H1, J1	2 bits address
12	K2	Write flag
13	L2	Switch flag

4.2.9 GUI interface

The Graphical User Interface (GUI) was created using the Python programming language in conjunction with the PyQt5 package. The GUI needs the user to enter a frequency value before sending it to the microcontroller via serial connection. Signal pulse width and module value are optional fields. The frequency input is used to generate the generic square wave. In the GUI, there are three push buttons, each of which has a particular function. To communicate all parameters in the fields to the microcontroller, the *set* button must be pressed. When the *run* button is pressed, a 1-bit signal is sent to the FPGA through the microcontroller to release the trigger signal to the telescope. Finally, the *stop* button must be pressed to stop the trigger generating signal. The backend of the trigger program is also written in Python and uses Pyserial. Figure 4.10 depicts the GUI for the trigger system controller.

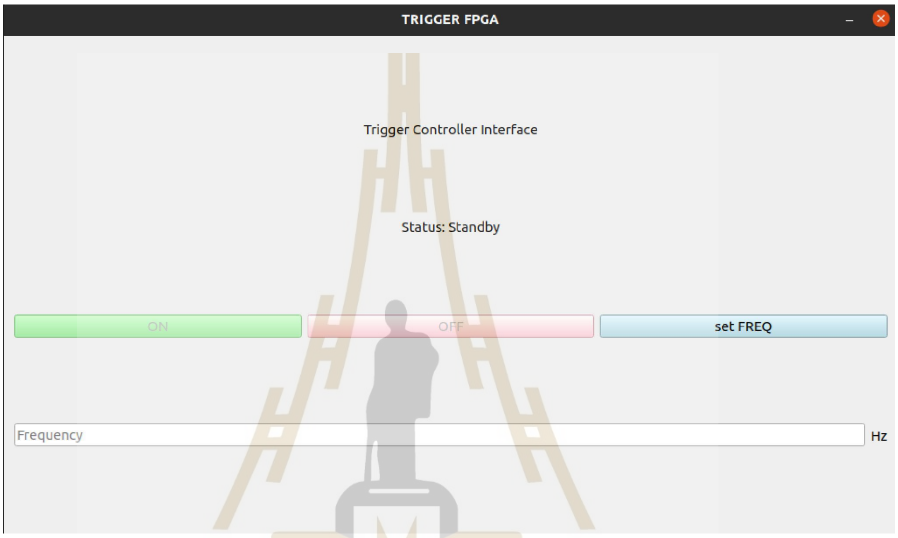

Figure 4.10 The Graphical User Interface (GUI) of FPGA trigger.

4.2.10 Signal operation

The data from the microcontroller is stored in the trigger generator's buffer. To generate a wide range of trigger frequency values, data must be provided simultaneously with the address of the FPGA buffer. When all data in the data buffer is fully occupied, the microcontroller will transmit the ready signal to the GUI, informing the user that the trigger system is ready to send a signal to the sensor. The ALPIDE sensor, which is linked to the DAQ board, can measure proton hit from numerous frames. The trigger system regulates the readout rate. The trigger signal is a periodic square wave generated by FPGA programming's clock divider logic. The Basys3 provides a 100MHz programming clock from the W5 pin. However, the maximum frequency that the DAQ board can discern is around 9.5 kHz. So, in this experiment, we set the trigger to maximum and the amount of occurrences to 5000. The sensor waited for the proton beam from the KCMH cyclotron to be irradiated before storing the detection data at the trigger on signal.

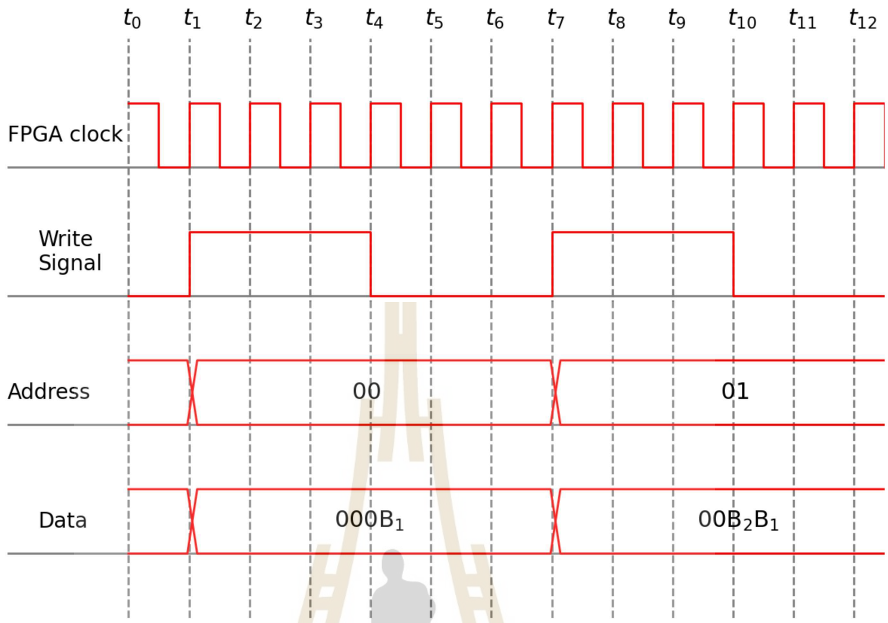

Figure 4.11 FPGA trigger operational signal of registering the frequency value to FPGA buffer along its 2-bit address.

The interface sends the GUI ON signal to the microcontroller, which turns on the Switch signal. As shown in Figure 4.12, the divided clock signal is created as a trigger signal. When the GUI is turned off, the trigger signal is reset.

4.2.11 Varian ProBeam proton PBS system

king chulalongkorn memorial hospital (KCMH) had installed the proton therapy machine since 2019 and started treatment in 2020. It is a cyclotron based accelerator by Varian named the ProBeam Compact proton therapy system with single Grantry. The intensity of the proton beam is controlled by the cyclotron. The beam intensity is checked again when it exits the cyclotron. The proton energy can be continuously modified between 70 and 240 MeV, and between 240 and 250 MeV in 1 MeV increments. The beam automatically turns off if the intensity is deemed too high. The switching of beams between treatment rooms during a patient's therapy can be pre-planned, minimizing the time required to move between patients. The system's parameter control can be divided into devices and sections, allowing machine maintenance to be done

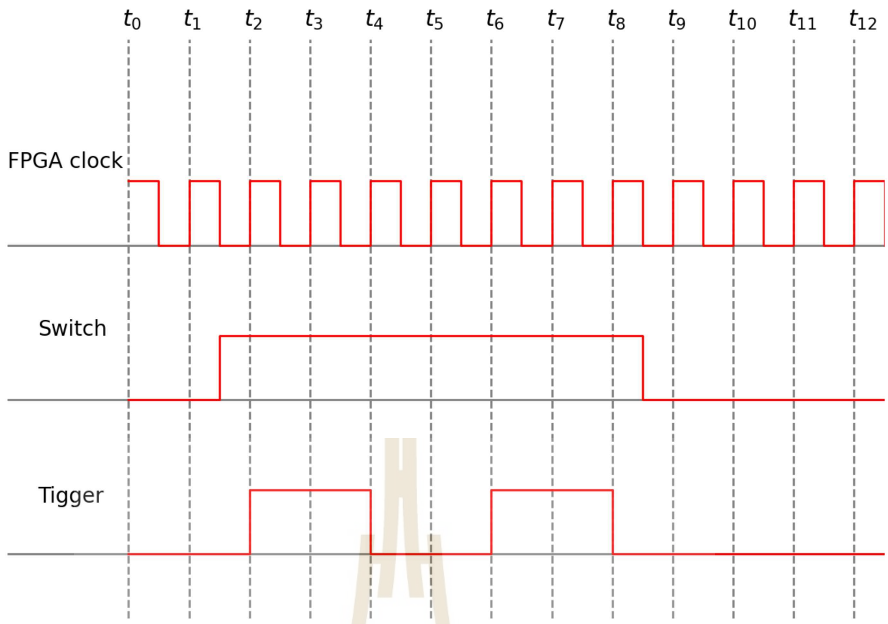

Figure 4.12 FPGA trigger operational signal with turning ON Switch signal.

in sections and preventing failures from affecting the entire machine. Remote beam diagnostics are also an option.

Treatment room

The treatment room consist of gantry and the treatment table to ensure that proton beam can be delivered to precise position of the tumor volume in a patient. The treatment room is essentially a 3.5-meter-long, cylindrical tube with an inner diameter of around 5 meters and an enclosing that is patient-friendly. It offers sufficient room for the table to be positioned in any recommended therapeutic position. A customized workflow engine guides the user through the process via the Proton Treatment Console system. It starts with identifying the patient and the patient-specific equipment before guiding the user through position verification, treatment, and report production. The system is designed as a client-server application, allowing two persons to operate simultaneously - one in the therapy room prepping the patient and the other in the control room setting up the treatment. The QA mode of proton beam was used in this experiment. Figure 4.13, the experimental setup is shown as it is in the treatment room.

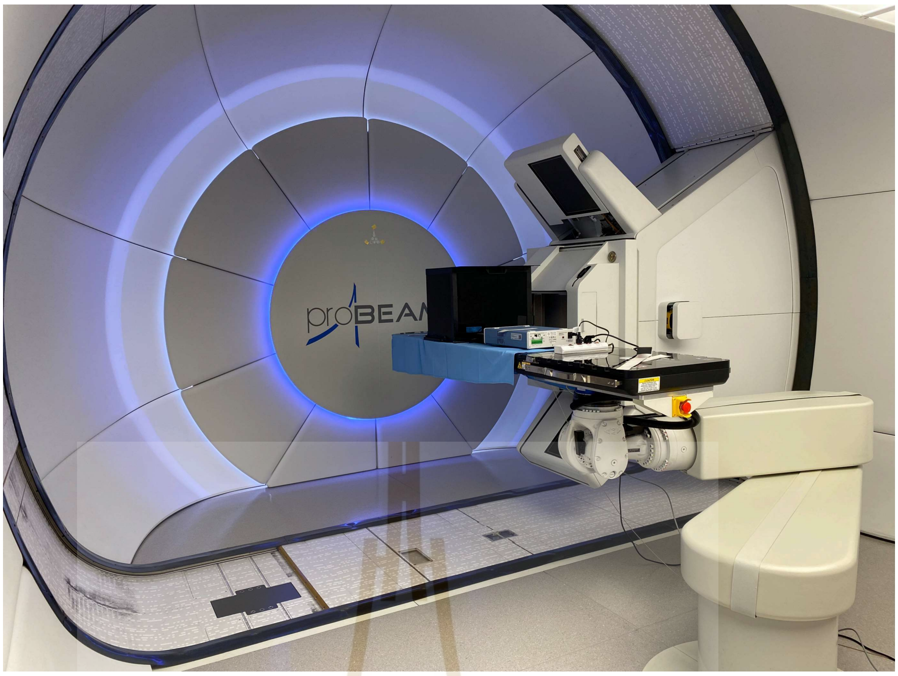

Figure 4.13 The treatment room at KCMH where the experiment setup is placed.

Control room

The Proton Treatment Console system employs a customizable workflow engine that directs the user through the process. The control room consists of the Proton Treatment Console (PTC) which is the front end of the proton machine. Control of the treatment is handled by a dialog screen. It displays the dose rate, the MUs, and the proton energy. Throughout all work processes, the PTC shows the patient's picture and data along with system and machine status information and the beam waiting time. The beam parameters can be optimized by the PTC in the room. In this experiment, the QA mode of proton beam was used. The beam parameters and patient bed position are configured by the monitor in the control room as show in Figure 4.14.

Proton beam in QA mode

Quality assurance (QA) is used to guarantee that accurate input data for treatment machine setup in a therapy planning system, appropriate dosimetry equipment is needed for base data measurements. It requires specialized sensors and dosimetry equipment. Dosimetry equipment for scanned proton beams is comparable to that

Figure 4.14 The control room has monitors for requiring users to adjust patient bed position, parameterise proton beam and creating treatment plan.

used in photon treatment, with the extra requirement of meeting longer operational ranges, particularly in terms of time duration and dose rates, as well as better spatial resolution. Based on its knowledge, Varian can assist each customer in selecting appropriate dosimetry equipment from third-party providers. The beam current of various beam energies provided by the KCMH technician are shown in Table 4.3.

Table 4.3 Proton beam parameters in Quality Assurance (QA).

Beam energy (MeV)	Current (nA)
70	300
100	200
120	160
150	150
180	50
200	10

PBS beam

As already described in Section 3.2.2 about KCMH beam spot sigma, the beam shape can be represented as Gaussian model that is spreading along the traveling path because of the scattering with air. In the simulation section, the curve fit achieved for optimising beam spot at Nozzle position of 42.1 cm apart from ISOCENTER and the beam energies was use of 70MeV and 200MeV. In Table 4.4, the spot sigma data are shown in various energies of the source with the distance apart from ISOCENTER point measured by Lynx PT from IBA dosimetry.

Table 4.4 Lynx PT measured the proton spot size (sigma, mm) of the KCMH proton center from IBA dosimetry.

Distance from ISOCENTER (cm)	-20	-10	0	10	20
Energy (MeV)	σ (mm)	σ (mm)	σ (mm)	σ (mm)	σ (mm)
70	7.10	6.45	5.95	5.45	5.00
100	5.65	5.20	4.95	4.65	4.35
120	5.05	4.70	4.50	4.35	4.15
150	4.45	4.30	4.15	4.00	3.85
180	4.20	3.95	3.80	3.80	3.55
200	3.95	3.75	3.65	3.60	3.50
220	3.80	3.70	3.50	3.50	3.40

4.2.12 Experiment setup

The components of the experiment are outlined in Chapter IV's content. The ALPIDEs telescope, EUDAQv2 software, FPGA trigger, and its GUI serially interfaced with the microcontroller comprise the experiment setup. As shown in Figure 4.15, a dark box contains practically all of the experiment setup to limit light source detection in the treatment room. The dark box was put on the patient's bed, and the bed was adjusted to align the telescope's orientation with the proton beam nozzle.

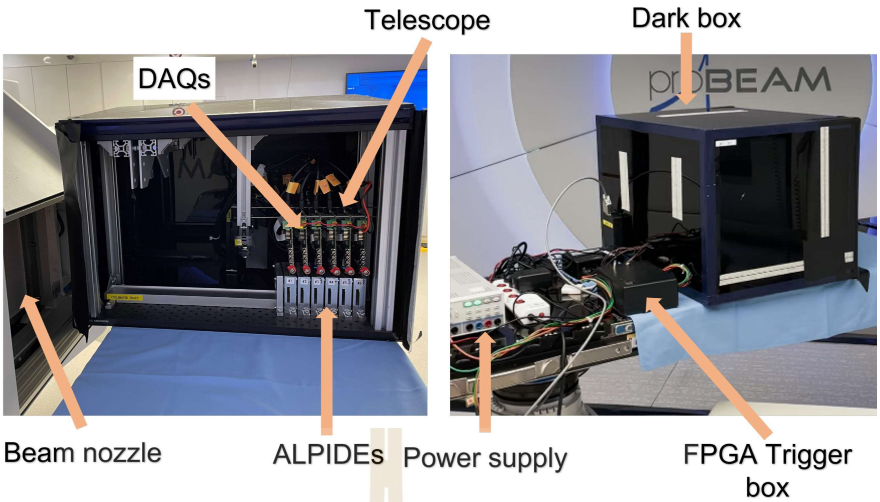

Figure 4.15 For the KCMH beam test, the experiment configuration of the FPGA trigger controlling system interfaced with ALPIDEs telescope. While the telescope was inside, the power source and trigger were wired out of the dark box. The telescope was likewise linked to the power supply.

4.3 Results and Discussion

4.3.1 Trigger signal

The Basys3 FPGA was programmed using Vivado ML Edition 2021.2 to serve as the Telescope's trigger. To configure the logic blocks of an FPGA, the Verilog language is written as RTL. The Verilog module requires four input variables: switch, write flag, write address, and write data value, as shown in Table 4.2 in section 4.2.6, which demonstrates the implementation of FPGA PINs on their operations. Figure 4.16 depicts the FPGA writing procedure in the Vivado signal simulation.

Figure 4.17 displays the operational signal of the FPGA trigger in Vivado software simulation after the frequency value of the trigger is registered to the FPGA trigger register. The frequency of 9.5 kHz is chosen as the maximum value to which the Telescope's DAQ can respond.

Figure 4.18 shows the WaveRunner 8254 oscilloscope, which provides an amazing user experience as well as a wide range of capabilities to speed up the debugging process. The oscilloscope has unrivaled touch capabilities in the market, allowing for maximum efficiency in operation. The device has a wide bandwidth ranging from

Figure 4.16 The simulation signal used to write a frequency value to an FPGA register. A particular address is assigned to each of the various 1-bit input values.

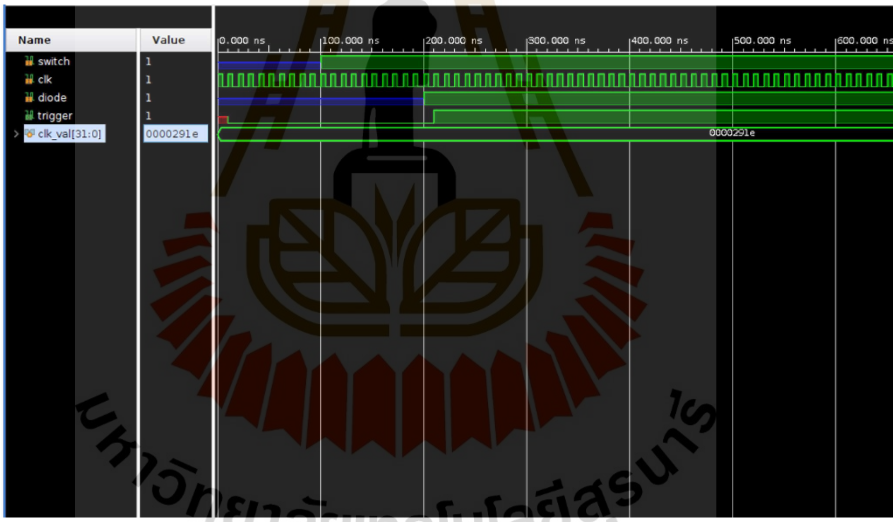

Figure 4.17 The generating trigger simulation signal. The frequency is set to 291E of Hexadecimal.

500 MHz to 2.5 GHz, a sample rate of 20 GS/s, and a large memory. The WaveRunner 8254 is a highly powerful instrument that is also incredibly user-friendly, thanks to MAUI's innovative user interface and a flexible range of capabilities.

The Waverunner 8254 was utilized to measure the FPGA trigger signal. According to Section 4.19, the 3.3V output of Basys3's trigger signal is shifted to 5V by

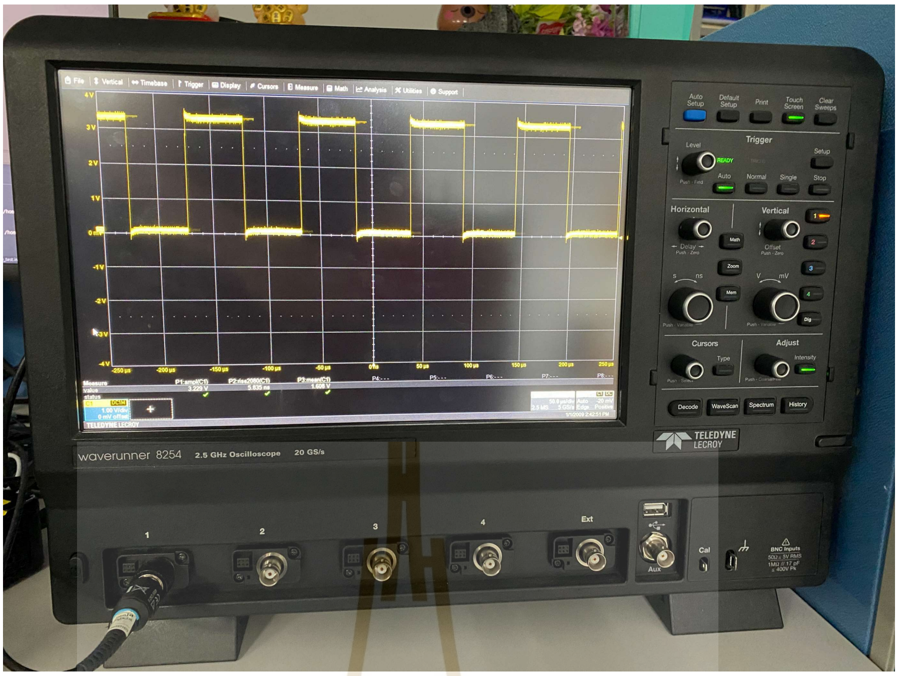

Figure 4.18 The WaveRunner 8254 oscilloscope.

using the IC SN74HC08N in the amplifier circuit. Figure 4.19 depicts the outcome of the Trigger signals.

4.3.2 Background measurement

The new trigger was first tested with EUDAQv2 by sending a 9.5 kHz trigger signal to the first DAQ board. The RUN's STROBE was set to 100 cycles. The output data was collected from the EUDAQv2's binary RAW format and exported in ROOT format. As shown in Figure 4.20, the background data was calculated as the mean of activated pixels on each ALPIDE layer. The first plane, which serves as the reference layer, has an extremely low background since its mean is close to zero. However, the background signal was discovered to be approximately 3.1 in the layer 4 as a mean of activated pixels in multiple event detection as the strongest signal when compared to the remainder layers.

Figure 4.21 shows the total number of active pixels for each occurrence. There are 6907 events that take place on the RUN. The average number of activated pixels on each layer was 6.518 pixels, with a standard deviation of 1.957 pixels.

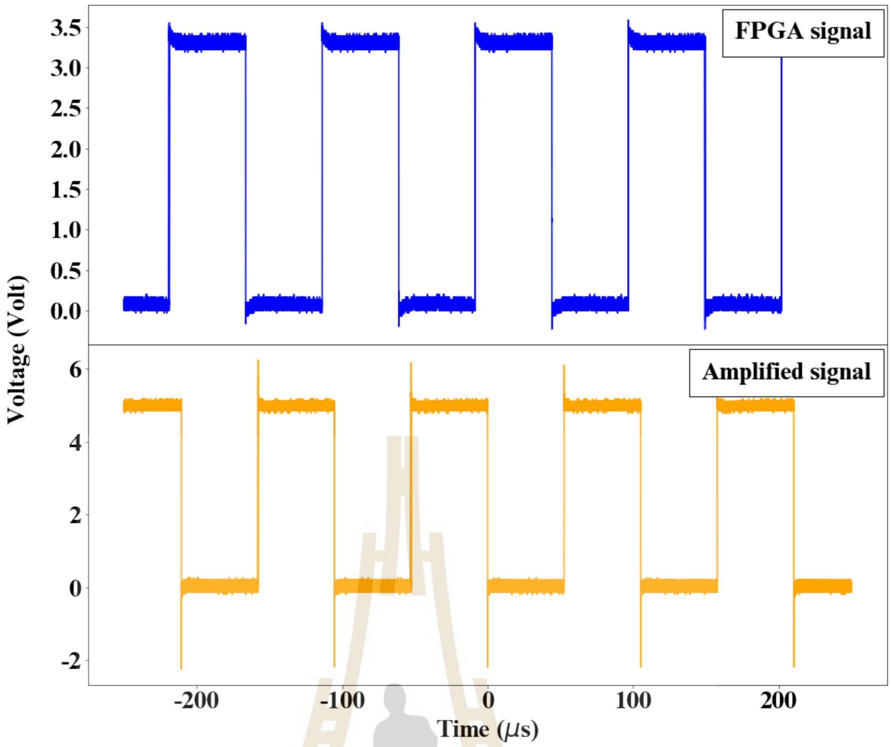

Figure 4.19 The FPGA trigger pulses of regular and amplified signals measured by the Waverunner 8254.

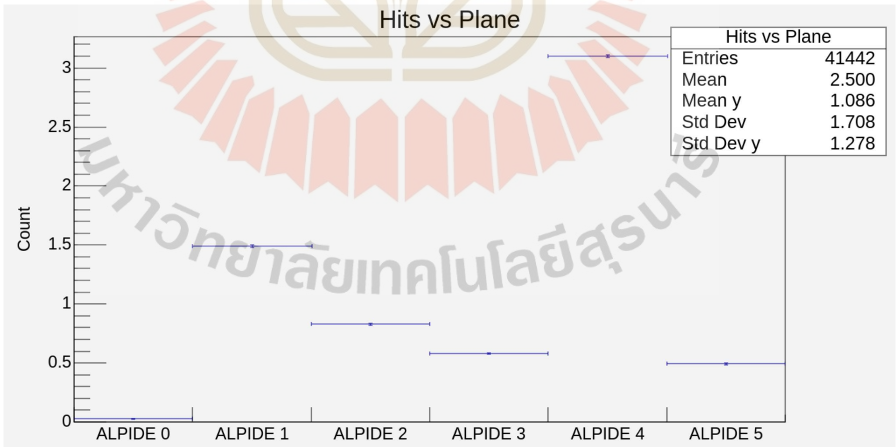

Figure 4.20 The mean of activated pixels of background measurement in 6907 events.

4.3.3 KCMH beam test

The first test for KCMH proton beam detection used the same setup as the background measurement detailed in section 4.3.2. In a configuration file, the number

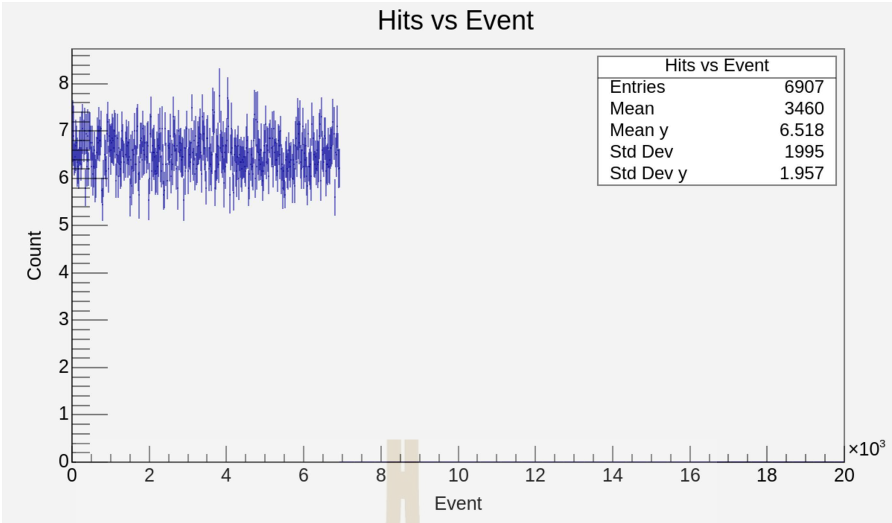

Figure 4.21 The number of activated pixels of individual event that is provided FPGA trigger as pulse signal.

of RUN events was set to 5000. Figures 4.22 and 4.23 illustrate the results of proton detection at 70 MeV and 200 MeV, respectively.

The hitmap findings show that the beam profile of 70 MeV is wider than the result of the simulation section. When comparing the first layer, the mean and standard deviation in the X axis of the beam profile for the 70 MeV beam are 516.1 and 213.4 pixels, respectively, while the 200 MeV beam has 506.7 and 143.5 pixels. Because to the overflow of source size, the Y axis is omitted. Another beam test result is the number of activated pixels on event number, as shown in Figure 4.24.

Unfortunately, the default histogram is provided by the event-hit result of raw data from EUDAQv2 by optimizing the bins. The total number of activated pixels given in the event-hit result is not the same as the result from the raw 2D hitmap presented in Figures 4.22 and 4.23. By observing individual event in EUDAQ data, the mean and standard deviation of activated pixels are shown instead of exact number of pixels as shown in hitmap results.

4.4 Summary

This section describes the configuration of six ALPIDEs telescopes and the FPGA trigger system used to send additional signals to the DAQ boards coupled with

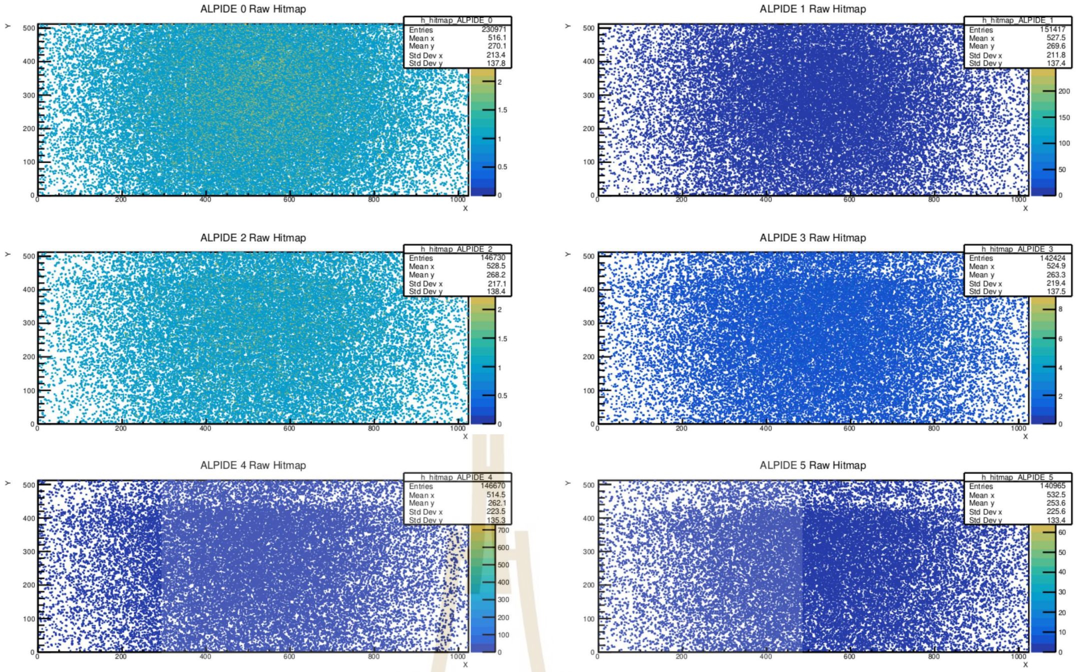

Figure 4.22 The 2-dimensional hitmap of six ALPIDE planes with 70 MeV proton source in 10 MU by applying 10000 events of trigger.

ALPIDEs. As a result, the FPGA trigger can send square waves to the telescope for background and real-beam testing. The output is pure RAW data generated from the EUDAQv2 software via image snapping. Multiple events are used to calculate the total number of active pixels. As a result, the method of selecting a single event to get individual EUDAQv2 result data must be implemented for analyzing data as event by event, as described in the following section.

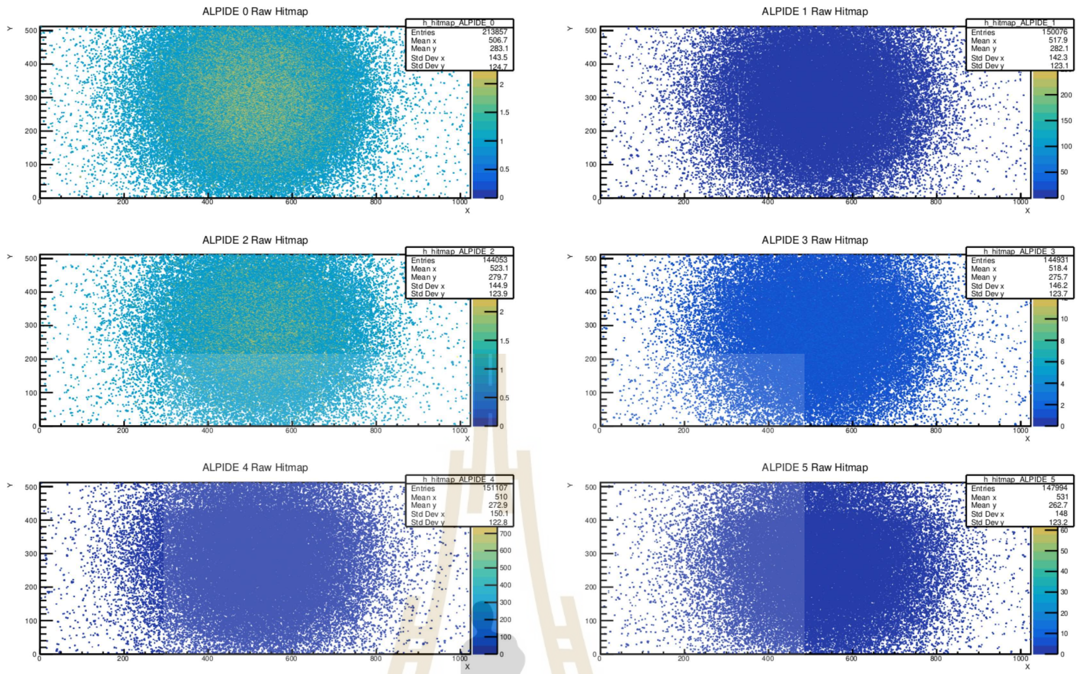

Figure 4.23 The 2-dimensional hitmap of six ALPIDE planes with 200 MeV proton source in 10 MU by applying 10000 events of trigger.

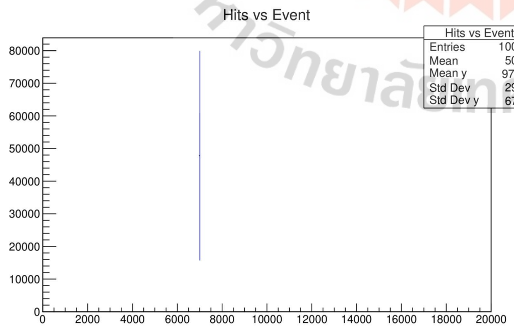

(a) 70 MeV.

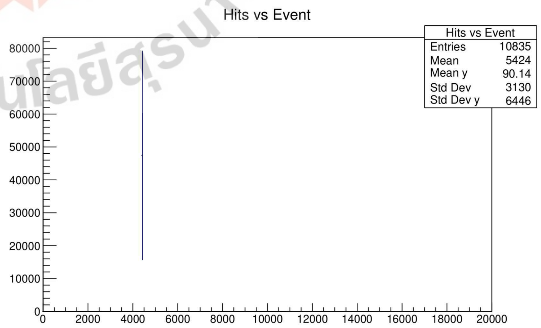

(b) 200 MeV.

Figure 4.24 The histogram of EUDAQv2 output for 70 MeV and 200 MeV of KCMH proton beam on 10000 trigger events.

CHAPTER V
DESIGN STUDY OF PCT TELESCOPE WITH TRACK RECONSTRUCTION

5.1 Experimental Setup

Utilizing the MAPS telescope and the KCMH proton beam, experiments were carried out to reconstruct the proton tracks. While conducting the experiments, an acrylic collimator was used as the beam aperture to eliminate the lateral beam from the proton source. King Chulalongkorn Memorial Hospital hosts the pCT-telescope experiment using a pencil proton beam. The pCT prototype was set up on the patient bed in the treatment area. Figure 5.1 provides an illustration of the experimental setup. The first layer of sensors is situated 5 cm after the isocenter, which is located 42.1 cm from the nozzle. Each sensor in the telescope is separated by a 2.5-cm gap and connected to six DAQ boards. An acrylic collimator that is 36 cm long is placed in front of the first sensor.

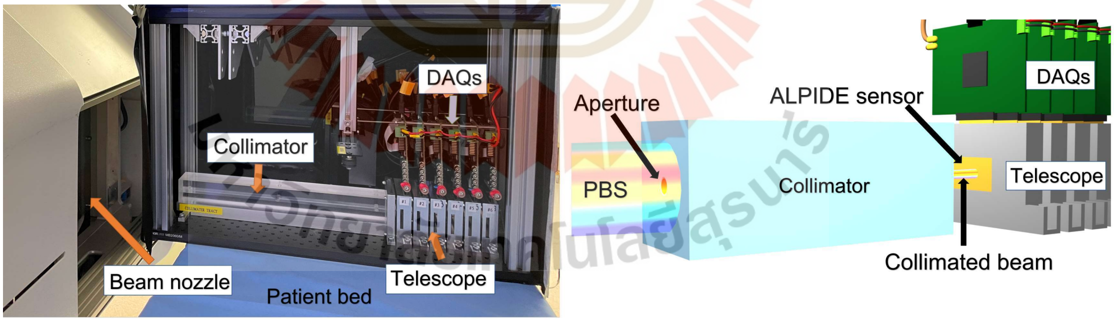

(a) Experiment construction (b) Experiment model

Figure 5.1 a) the KCMH telescope test with a collimator in the treatment room with its b) schematic picture.

The focused proton beam used in therapy is intended to only influence the tumor location while limiting harm to nearby healthy cells. In order to lessen the lateral intensity dispersion, depending on how many protons are needed, a collimation aperture is used. Polymethyl methacrylate (PMMA), also known as acrylic glass, was used as a collimator with a length of 36 cm, a surface area of 5 $\times$ 5 cm^2 and an aperture diameter of 1.0 mm, to remove the lateral penumbra from the tracking telescope's beam. The photograph of the acrylic collimator is shown in Figure 5.2.

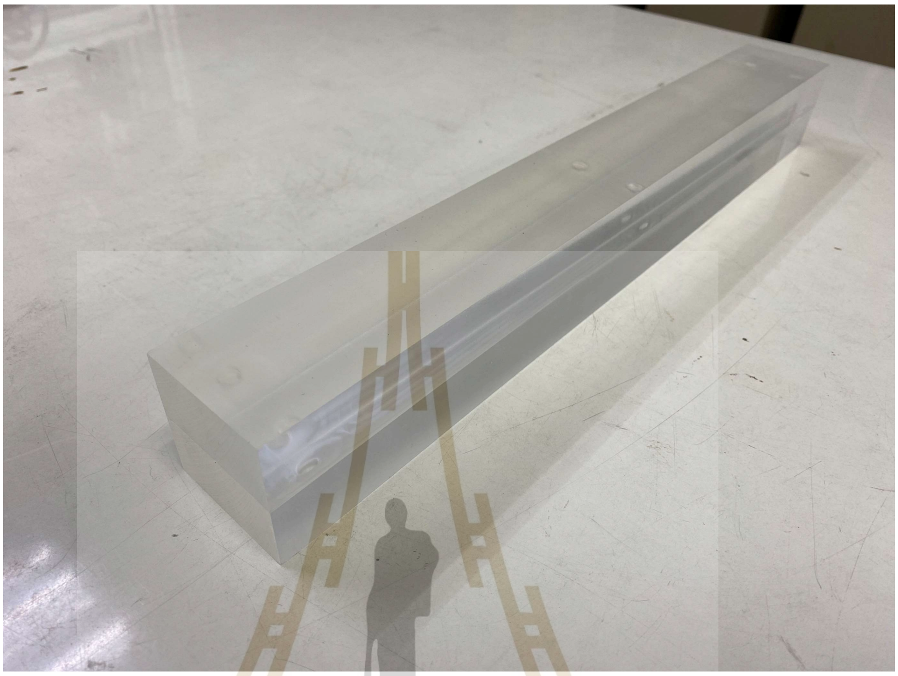

Figure 5.2 The 36 cm acrylic collimator.

5.2 Beam setup

The QA mode of KCMH proton beam has already been described in Section 4.2.11. Table 5.1 shows the specific proton beam parameters used in our experiments. The numbers of events which are evaluated with the data analysis are also shown in the table.

Table 5.1 Proton beam parameters in Quality Assurance (QA).

Energy (MeV)	MU	Events
70	1000	2525
200	500	1400

5.3 Data readout and conversion

Data exports were obtained using the EUDAQv2 program. All events are represented as binary files. It is difficult to extract the output file as there are multiple root files with information of all events. However, the binary files can be extracted to produce a root file that resembles a Hits Tree as previously mentioned in section 3.2.4

The EUDAQv2 output as binary data in RAW format indicates that the telescope's hit data is recorded event by event. The EUDAQv2 mornitor can be used to export RAW to ROOT format by utilizing a command line mode. Unfortunately, exporting more than one event for a RAW to a ROOT file results in the merger of all events into one. So during this process, in the event of collecting data, a software for RAW to ROOT conversion was developed. Every proton event has a unique impact. The application was created using a multi-threaded Python script with a worker thread assigned to export a single file having the main thread for observing the ROOT event in the RAW file output as represented in Figure 5.4's flowchart.

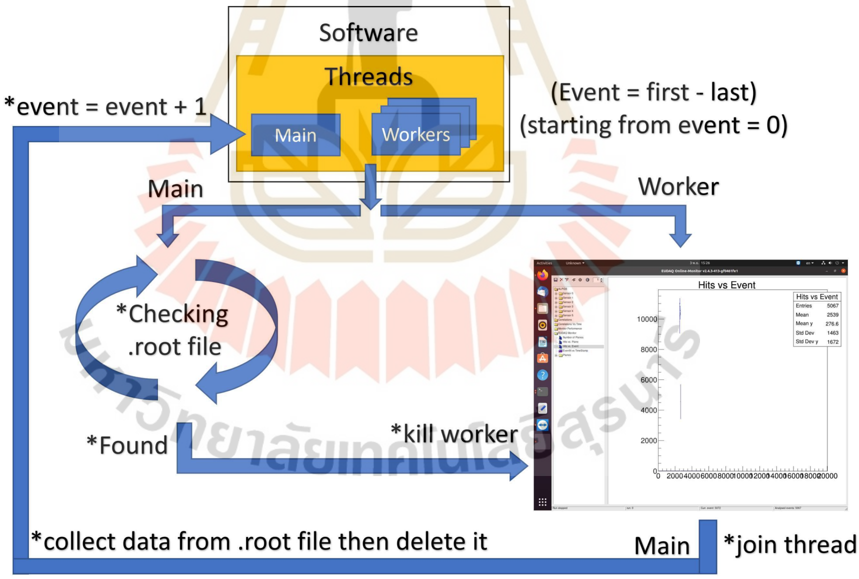

Figure 5.3 The flowchart demonstrates how multi-threading software works. The Software runs from interested event 0 to interested event n. The central theme monitors the export's.root file in an endless loop. Upon finding the main thread .root file, the main thread will compel the worker thread to terminate EUDAQv2 monitor. Finally, the exporting program gathers all ROOT files before repeating the process. The last task is to repeat the procedure while increasing the number of events.

5.4 Data analysis

The hit collections obtained from individual EUDAQv2 events must be processed in accordance with section 5.3 by erasing the background information and gathering cluster hits. Then, the information can be used for track reconstructions.

5.4.1 Noise and background

Firstly, a test is carried out in the dark to measure noise signals in the telescope placed in the treatment room at KCMH. Several events were gathered to establish background noise before the beam test starts. Both noise and beam events are recorded in the EUDAQ raw file, and the hot pixels are visible. The background results indicate that the noise pixels are created at random and often have cluster sizes of 1-2 pixels. Even though the hot pixels are randomly generated, they only group together for single hits. Single and two-pixel clusters contribute to the noise pattern during a fake hit run according to research on the ALPIDE sensor's noise (Mager and ALICE Collaboration, 2022). As a result, any collection of active pixels that is smaller than three pixels is considered as noise in our work.

5.4.2 Clusterization

A collection of active pixels, that are connected to one another by the charge diffusion from the activated pixel to its nearby pixels, can be used to represent the proton hit. A recursive technique that gathers all nearby pixels is utilized to retrieve the hit's cluster data. This technique collects all activated pixels that are joined in the row and column of the current pixel, transforms the current pixel to those neighbors, and then checks to see if any activated pixels are present. The cluster's size is determined by the number of pixels in the region, and the pivot stands in for the actual hit location.

5.4.3 Track reconstruction

The output from EUDAQv2 must first be preprocessed by separating out individual events, removing background noise, and grouping clusters as previously discussed in sections 5.3, 5.4.1, and 5.4.2, respectively, before the track can be calculated from the output data. The EUDAQv2 data has been preprocessed and is now ready to be used in the reconstruction procedure as outlined in section 3.2.5 of the simulation.

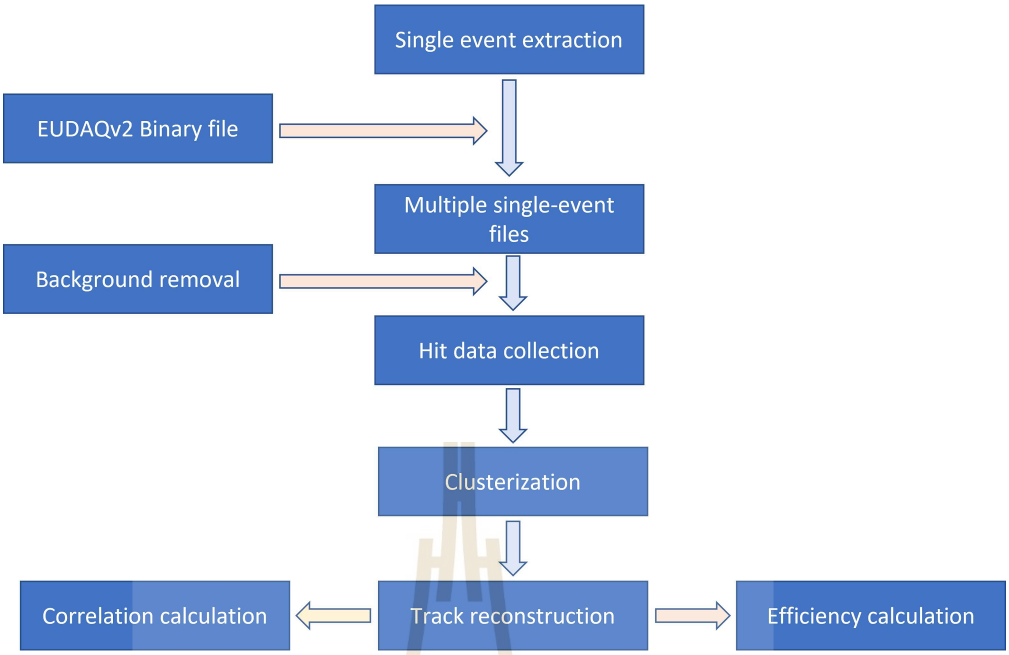

Figure 5.4 The flowchart of the track reconstruction process that the track following algorithm description can be found in section 3.2.5, the track efficiency was calculated as track survival in section 5.4.4, and the correlation of the reconstruction definition will be mentioned in Section 5.4.5.

5.4.4 Survival tracks

Based on impact information, tracks can be reconstructed using a detector geometry made up of several layers of silicon sensors. The number of accurately reconstructed tracks that match the original simulated data divided by the total number of simulated tracks is used to assess the simulation's track efficiency (CMS, 2010). The original tracks in experiments are unknown, but the longevity of the reconstructed tracks can be evaluated by counting the hits accumulated on a single track. All protons pass through all of the stacked sensors when a proton beam with an energy between 70 and 200 MeV is directed at the KCMH telescope. A proton track should have six hits from six sensor layers. The experiment's dead tracks are categorized as algorithmic failures.

5.4.5 Correlation

The telescope is initially pre-aligned by calculating correlations between each layer and the reference plane. The acquired differences are then centered at zero by modifying the individual layers' position in the global x and y coordinates. Tracking is possible because to the first pre-alignment and a flexible matching criterion (Dannheim et al., 2021).

5.5 Results

The outcomes of this section display the KCMH trials' noise and background, beam profile, cluster distribution, track reconstruction, and correlation.

5.5.1 Noise and background

The dark test condition indicated in section 5.4.1 can be used to determine the noise and background signal from ALPIDE sensors in the telescope.

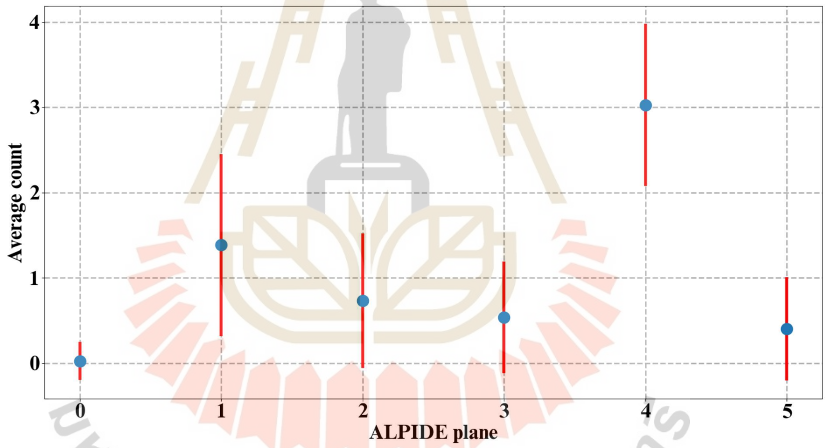

Figure 5.5 The illustration of average activated pixel count of each event for every ALPIDE planes in the telescope during the dark test. The red line indicates the standard deviation of activated pixels.

The EUDAQv2's 50000 events are used to measure the noise and background. The 3952 samples of ROOT hit data are obtained with the average activated pixel values as shown in Figure 5.5 and the cluster size distribution is given in Figure 5.6 .

Every ALPIDE layer's noise count is calculated using the number of noise clusters identified as outlined in section 5.4.2. Only the ALPIDE in layer number 4 is found with one and two pixel clusters, as seen in Figure 5.6. So, to prepare the data for

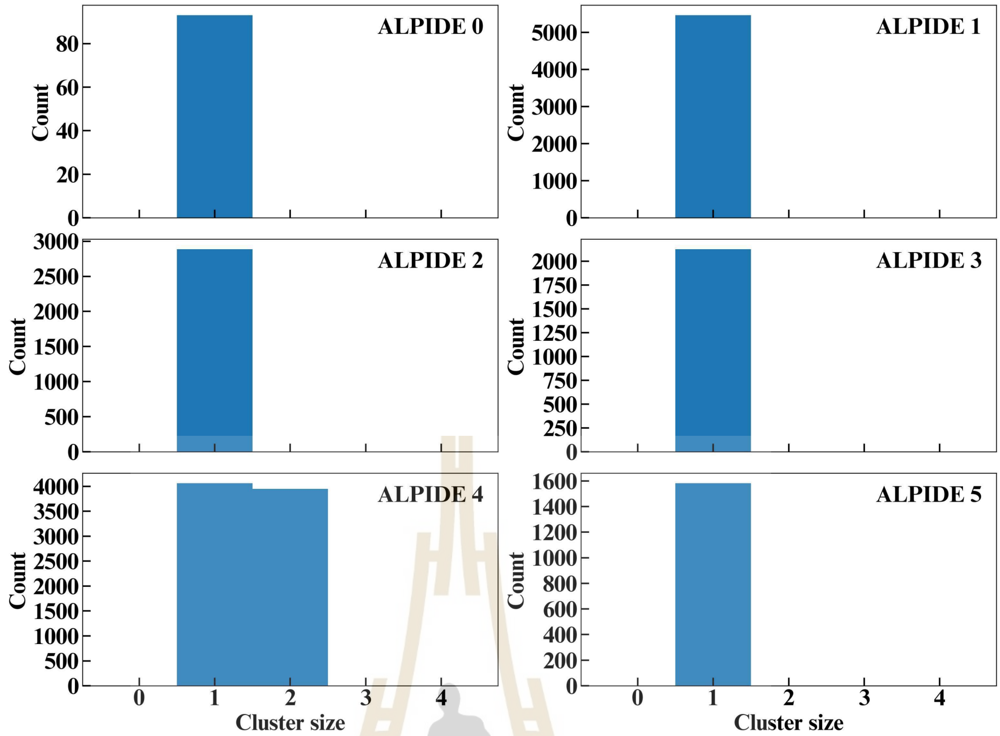

Figure 5.6 The cluster size distribution of every ALPIDE layers which generate noise and background signal in the dark test.

the track reconstruction, the noise and background must be removed by subtracting the one-pixel and two-pixel values.

Based on the information of the pixel numbers that are active during the dark run, the background and noise caused by oversensitive pixel can be identified. We use these information to locate those pixels in each layer that was triggered throughout the test with entries that were 50% greater than the mean of activated pixels. This information is provided in Table 5.2. It is interesting to note that the 5th plane has the most noise and background pixels (16) whereas the first layer has the fewest noise and background pixels (3).

5.5.2 Beam profile

Generally, there are approximately 10^9 particles per second for the proton beam to be effective in the cancer treatment. Since this is such a high flux, it is difficult to count the precise number of impacts in a single cluster as there are many clusters overlapping. The subsequent experiments were planned to address this issue. At the

Table 5.2 The pixel numbers that are activated with 50% of the dark test entries.

ALPIDE layer	Pixel numbers	Total entries
0	309555, 459156, 487717	93
1	148649, 162205, 207597, 211801, 250549, 305779, 332696, 360963, 405989, 442122, 501462	5464
2	106187, 125144, 167402, 249603, 302114, 361127, 408008, 438522	2886
3	44424, 100084, 341439, 387475, 475996, 484290, 507905	2125
4	160569, 247721, 258687, 262190, 280699, 351638, 351852, 360671, 361695, 393439, 416917, 441413	11967
5	37640, 182686, 218738, 224635, 244777, 283809, 303255, 307263, 311834, 361292, 393523, 395461, 492432, 522648	1582

KCMH hospital, by using a collimator, we are able to reduce the the number of proton in the pencil beam. As a result, the number of activated pixels also decreased since there are smaller number of pixels in ALPIDE being activated, as seen in Figure 5.7.

The 2D collimated beam profile was fitted with a Gaussian distribution, and the lateral 70 MeV protons were removed using an acrylic collimator. The collimated and noisy Gaussian distributions were used to optimize the beam fitting models for the treatment beam with the energy ranging from 120 to 200 MeV. A circular zone is designed with a 2-sigma aperture profile as a constraint for information extraction from the collimated data. Based on the mean and sigma values obtained from the Gaussian fit, only the filtering areas were chosen.

The beam sigma on each telescope layer after the collimator are shown in Figure 5.8a. For track reconstruction, the wider (70 MeV) and narrower (200 MeV) beam profiles were taken into consideration. The total number of activated pixels on each sensor plane that were filtered by the 2-sigma fields of 70 MeV and 200 MeV for each collectable event are shown in Figure 5.8b.

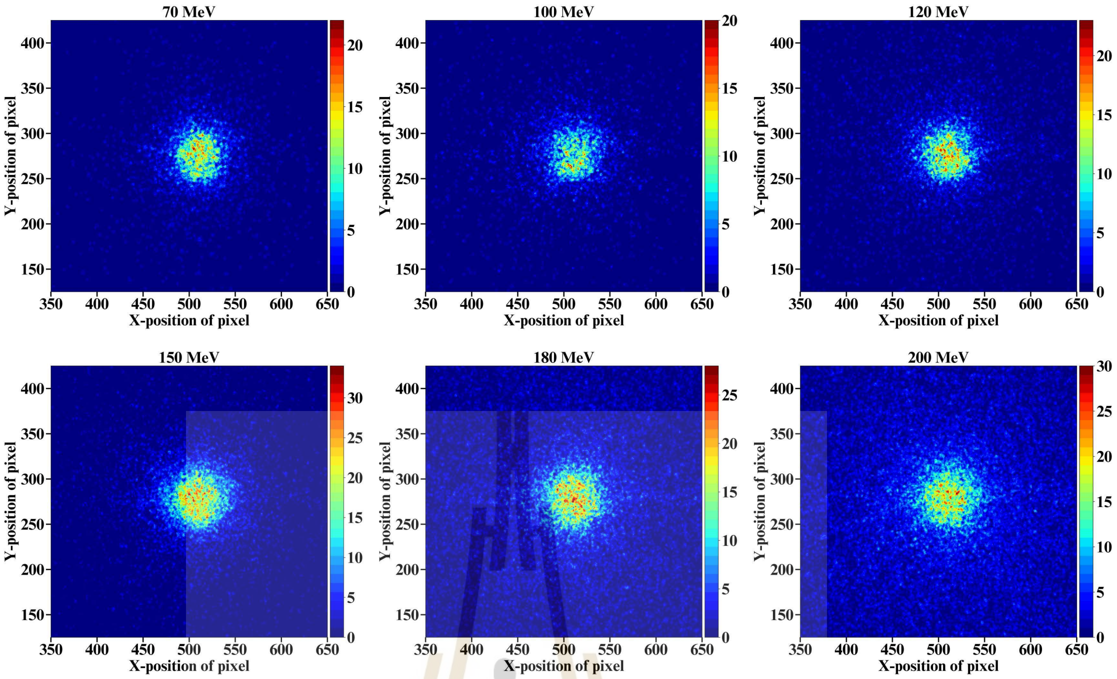

Figure 5.7 These histograms represent the distribution of pixel activations from the initial sensor layer, positioned 5 cm behind the isocenter. The treatment beam passes through an acrylic collimator.

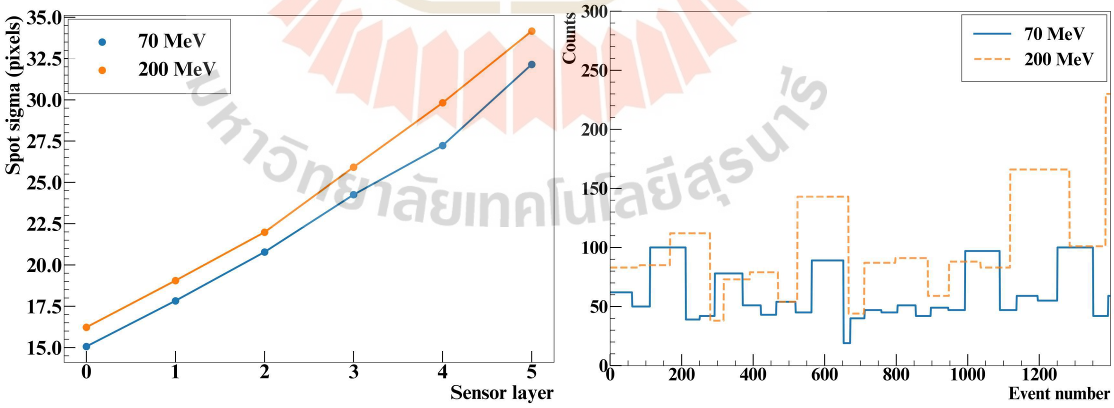

(a) Spot sigma (b) Total activated pixels

Figure 5.8 The figure shows a) the spot sigma of six ALPIDEs and b) the number of activated pixels from all ALPIDEs.

5.5.3 Cluster distribution

This part displays the hit data cluster from the our acrylic collimator. The cluster as a collection of adjacent pixels can be assessed using Section 5.4.2. The 2-sigma constraint on the hit data of the collimator experiment is as stated in section 5.5.2. Figures 5.9 and 5.10 show the 9-sampling cluster morphologies of 70 MeV and 200 MeV, respectively.

At the KCMH facility, information on proton energy values was gathered, and the cluster size of six irradiation ALPIDE chips was assessed. Collimated proton beams with energy ranging from 70 to 200 MeV were used to test these chips. Particle data from the ALPIDE chips were carefully chosen inside a circular region distant from the average positions in order to exclude extraneous data resulting from background noise. The cluster size distribution and statistical data that are shown in Figure 5.11 are demonstrated as the variation in cluster size while utilizing different levels of energy for the reconstruction. The cluster size distributions are collected from six ALPIDEs of the telescope. The 2-peak in Figure 5.11b can be assumed that the characteristics of each sensor is slightly dissimilar. Cluster size and energy deposited on the ALPIDE chips were shown to be correlated with energy deposition values generated from Monte Carlo simulation using the GATE software and the QGSP_BIC_EMY physics lists package. The results are shown in Figure 5.12, which shows an decrease in the average cluster size when the energy of the proton beam focused on the ALPIDE increases. Notably, the mean cluster size was found to be at its smallest at a proton beam kinetic energy of 200 MeV, whereas greater cluster sizes were seen as the proton beam's energy values decreased.

5.5.4 Track reconstruction

After background and noise removal, clustering, and other preprocessing techniques have been applied to the hit data, the hitmaker determines the central positions of the clusters created and translates their local coordinates within each chip to the telescope's overall frame of reference. The proton tracks in the telescope are then located using the track reconstruction algorithm described in section 3.2.5.

The data from the experiment has already been filtered by 2-sigma area of the aperture on the collimator. Therefore, the reconstructed tracks are constrained to certain area. The S_{max} parameter is modified to reach the maximum of efficiency and the correlation of hit position is found as a factor for optimizing the cone as shown in

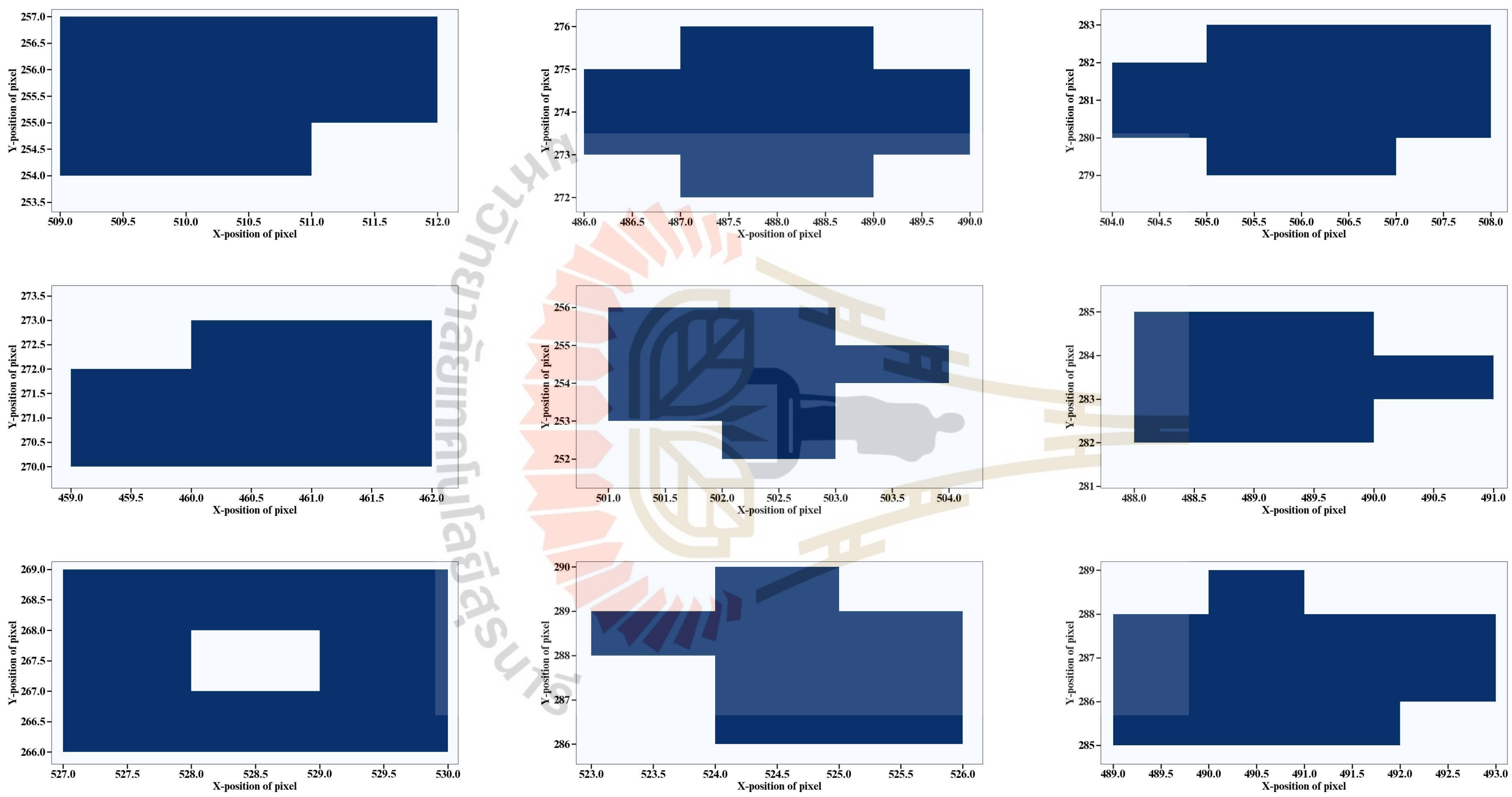

Figure 5.9 The illustration of cluster size samples which can be detected by the telescope with 70 MeV of proton energy.

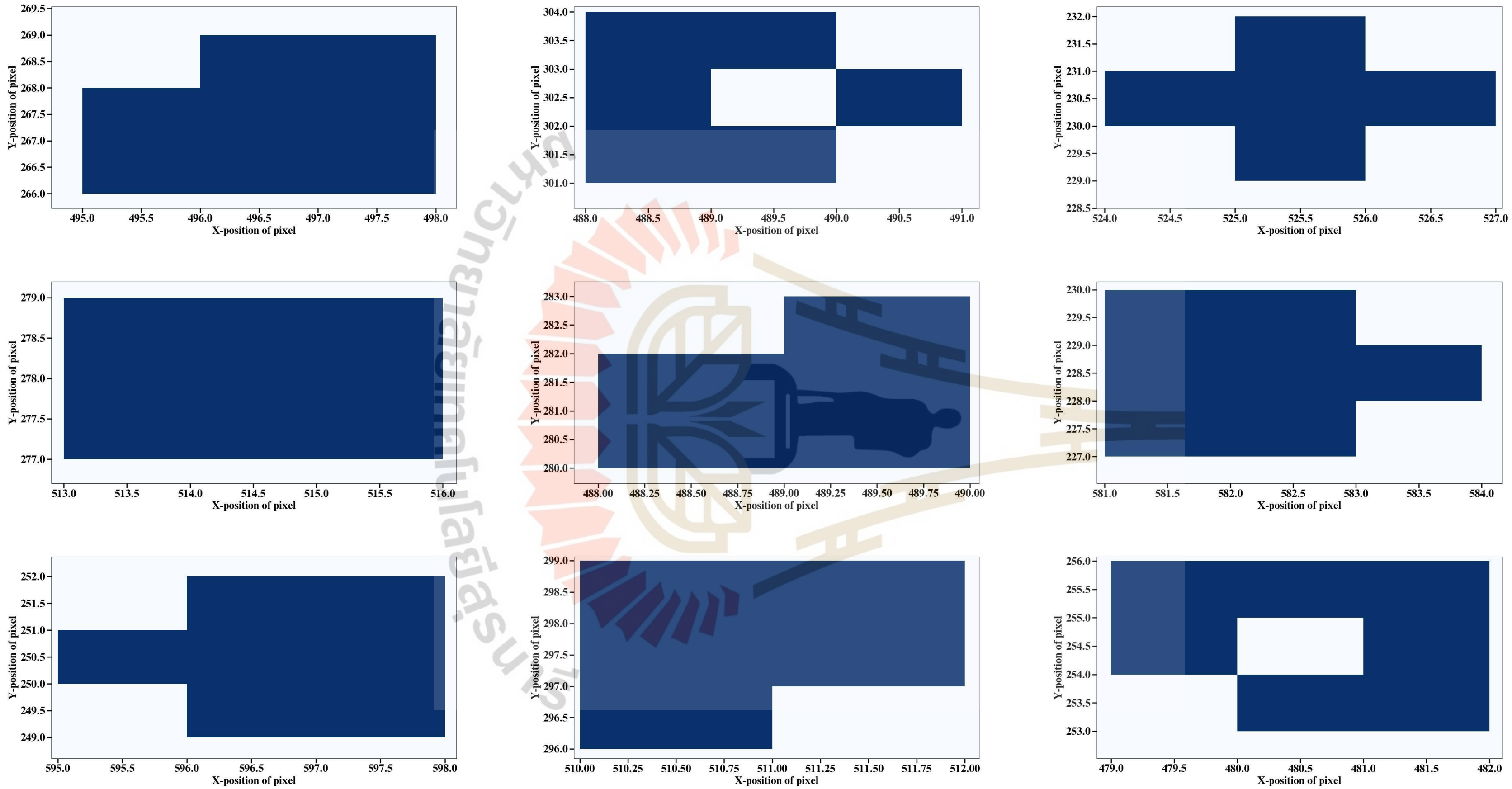

Figure 5.10 The illustration of cluster size samples which can be detected by the telescope with 200 MeV of proton energy.

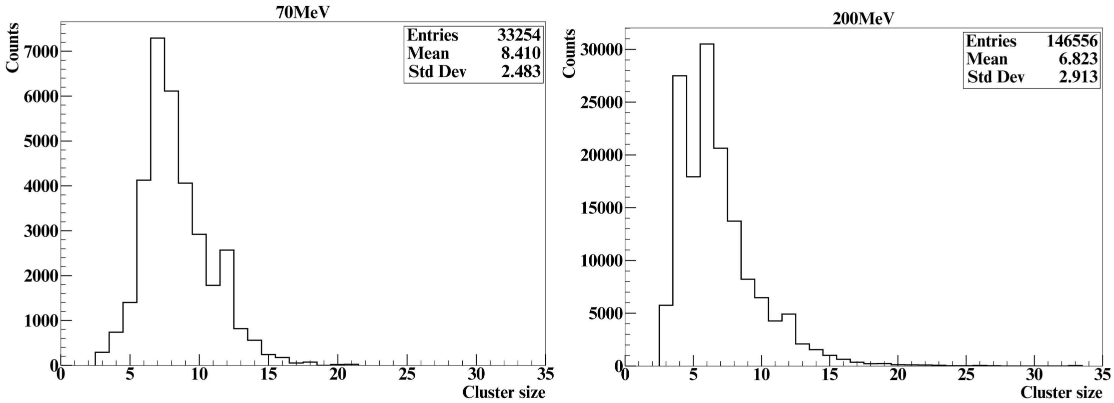

(a) 70 MeV (b) 200 MeV

Figure 5.11 The distribution of cluster sizes for collimated beam energies of 70 MeV and 200 MeV. These distributions were observed across 6 ALPIDE chips. In the top right corner of each figure, you can find the mean and standard deviation values for the cluster size distribution.

the Figure 5.13. This is due to misalignment in the experiment resulting to incorrect cone search calculation.

Using the output of Figure 5.13, it is possible to determine the S_{max} values of proton at the energy of 70 MeV and 200 MeV. The S_{max} at 200 mrad in 70 MeV of proton energy delivers the highest efficiency at around 72%, and S_{max} at 250 mrad in 200 MeV of proton energy delivers the best efficiency at 76%. As shown in Figure 5.14, both S_{max} that offer the maximum track survival at different proton energy are employed to optimize the track algorithm's cone search.

As in the result of Figure 5.14, the cone angle which provides a saturated curve at 70 MeV of proton energy is 45 mrad. To evaluate the search angle in 200 MeV of proton energy, it is difficult for only determining the 0-5 entries curve. However, in the Equation 3.4 with energy dependence, the angle at higher energies have to be smaller than that of at lower energies. By observing the curve that the $\Delta\theta$ is less than 45 mrad of saturated curve in 70 MeV, the $\Delta\theta$ of 200 MeV was choosen as 40 mrad.

The number of reconstructed tracks in the telescope's multiple events test-beam with the KCMH source are spread as shown in Figure 5.15. The histogram shows that the frequency is highest at single track for 70 MeV, and at three tracks for 200 MeV.

Eventually, the tracks produced by the track-following algorithm may be seen in Figures 5.16 and 5.17 for a single event and ten events from a total of 2525 and 1400

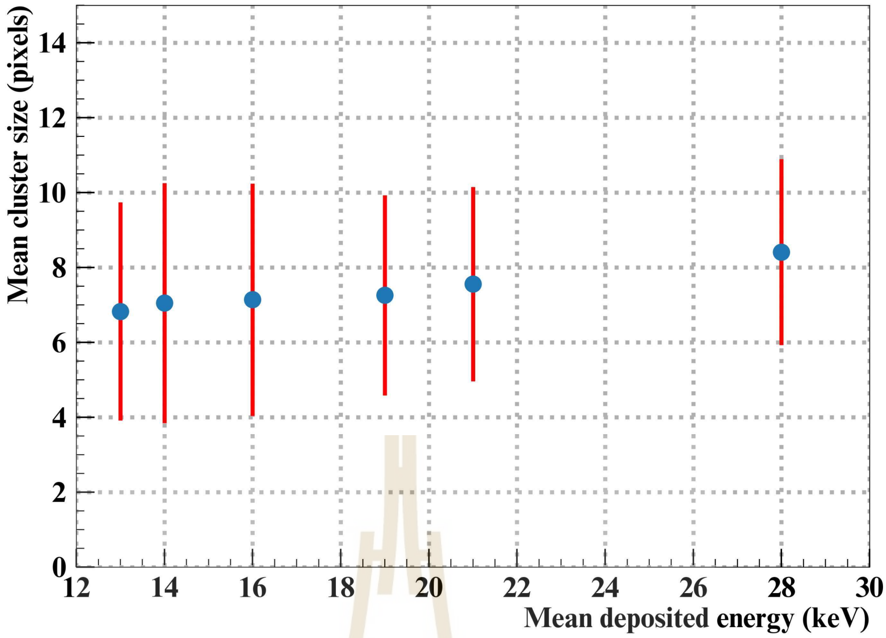

Figure 5.12 The correlation between the typical cluster size of proton beams traveling through the collimator and the typical energy deposited in the ALPIDE chip is illustrated graphically. The graphic contains information for proton beam kinetic energies between 70 MeV and 200 MeV. The mean cluster size values on the plot are surrounded by error bars that show the standard deviation of the cluster size distribution.

events, respectively, of 70 MeV and 200 MeV proton energy.

5.6 Summary

The 36-cm-long acrylic collimator was located in front of the telescope for particle reduction. Individual ALPIDE, which was contained in the telescope, detected only the apertured part of the proton source. The Gaussian model was applied to filter the collimated beam as 2-sigma area. Multiple events in default output of EUDAQv2 was exported to several ROOT files as a file per event by the Python automation. The noise of the telescope was measured by running the dark test. The 5^{th} ALPIDE has highest noise signal among all layers, and only two-pixel clusters were found in 5^{th} layer, while the rest show only one-pixel size. The data was subtracted by noise and background and collected as Pandas Dataframe to be used to calculate the cluster size and the track path. The 70 MeV and 200 MeV of proton energy were used as

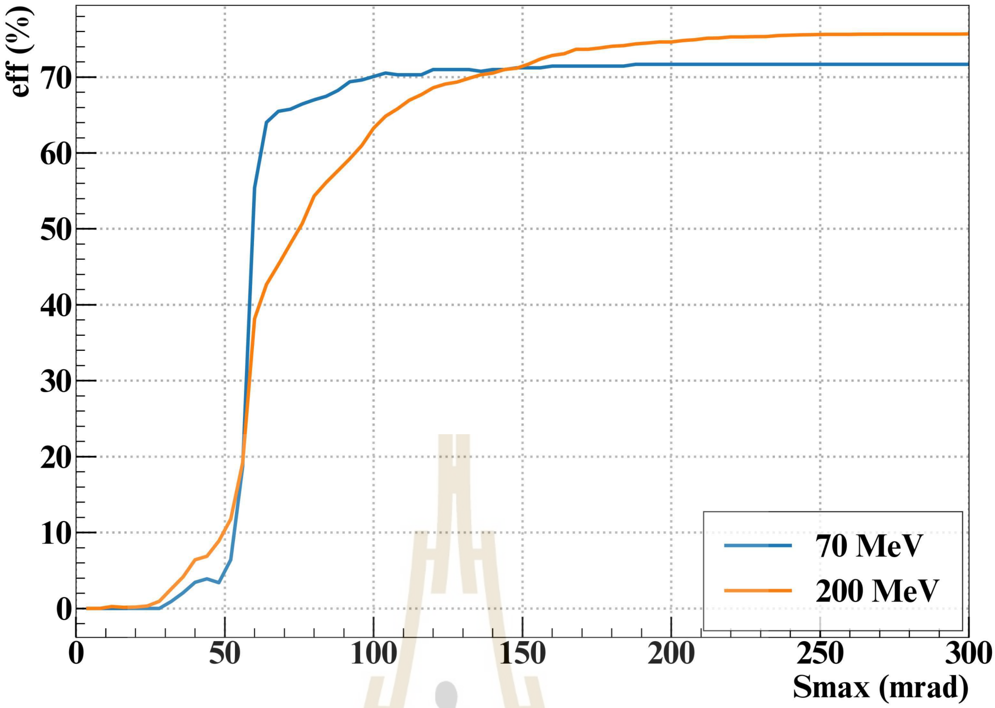

Figure 5.13 Illustration of the reconstruction efficiency of various S_{max} values.

particle sources for analyzing the particle tracks. The mean cluster size of 70 MeV was measured as 8.4, while 6.8 of mean cluster size was found in 200 MeV. The high energy source indicates low deposited energy absorbed in the material and causes small size of clusters. The center point of cluster is called hitmarker that is represented particle hit position. All hitmarker were stored as 3D information for being used with track reconstruction algorithm. The S_{max} parameter of 70 MeV and 200 MeV of proton energy were optimized by considering the track efficiency at 200 mrad and 250 mrad, respectively. The searching cone angle of 70 MeV and 200 MeV of proton energy were 45 mrad and 40 mrad, respectively, for the determined correlation. The results show that the telescope with track following algorithm can reconstruct the tracks from detection signal by irradiating with the KCMH proton beam.

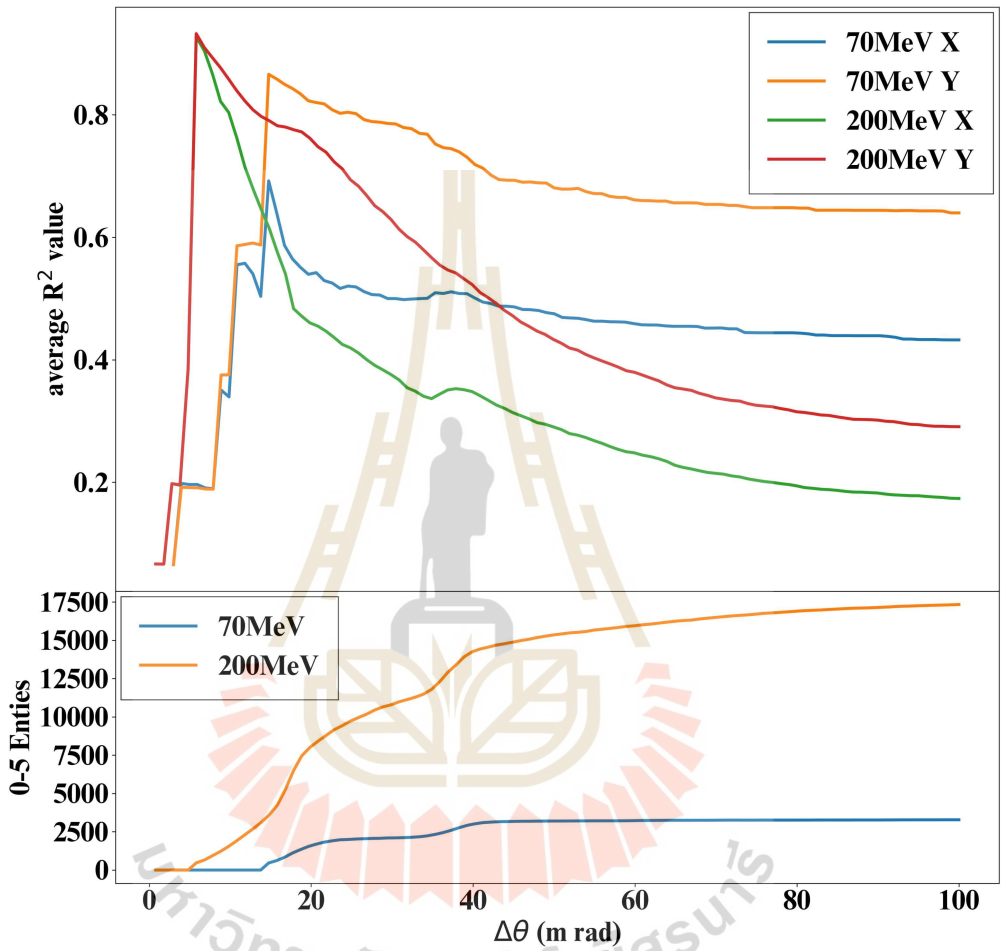

Figure 5.14 The averaged R^2 value of track reconstruction using a cone search angle of $\Delta\theta$ (upper) after fitting the location correlation of hit data on each ALPIDE layer in the telescope. The saturated curve (lower) is found by determining the average correlation of the X and Y axes between the first layer and the last layer.

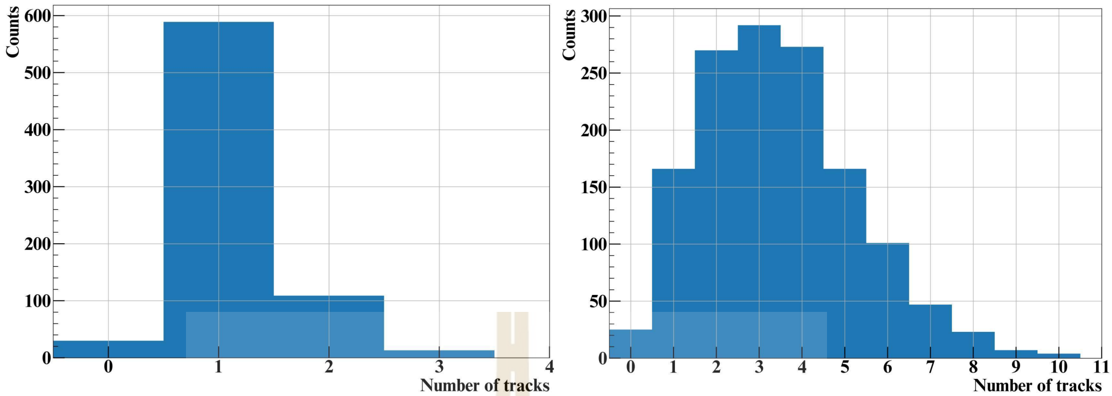

(a) 70 MeV (b) 200 MeV

Figure 5.15 The distribution of the number of reconstructed tracks in the telescope.

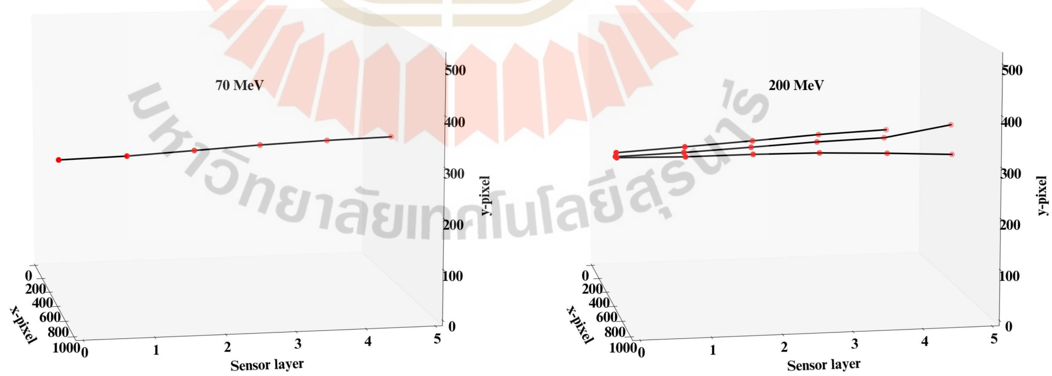

(a) 70 MeV (b) 200 MeV

Figure 5.16 The visualization of track reconstruction from the experiment with the acrylic collimator in 70 MeV and 200 MeV of proton energy within single event.

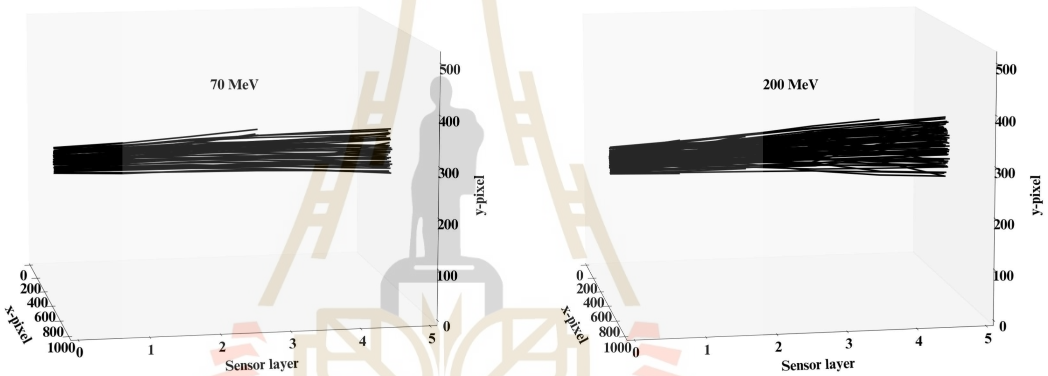

(a) 70 MeV (b) 200 MeV

Figure 5.17 The visualization of track reconstruction from the experiment with the acrylic collimator in 70 MeV and 200 MeV of proton energy. The number of events which are chosen from the total data events is 10 events.

CHAPTER VI
SUMMARY AND CONCLUSION

The track following algorithm is utilized to reconstruct proton tracks. The MAPS telescope simulation demonstrates how particle impacts are recorded as 3D data, forming tracks. The MC simulation employed beam profiles of 70 MeV and 200 MeV of proton energy as sources. These sources were modeled using a 2-dimensional Gaussian, commonly used in proton therapy centers. To achieve optimal results, the algorithm's searching angle and S_{max} parameters must be calibrated. The interaction of particles with material was assessed using Highland's equation, and the resulting scattering angles were compared to cone angles. In high-energy sources, the searching angle and calculated scattering angle values are more comparable than those in low-energy sources due to the lower energy deposited by the primary particle in the material. By optimizing the number of primaries in the simulation model, the efficiencies of track reconstruction were determined. However, increasing the number of primaries in low-energy beams significantly reduces the accuracy of the algorithm. The pCT prototype of Loma Linda (Giacometti et al., 2017) requires an ALPIDE sensor to detect fewer than 400 particles per frame in each plane. Hence, the telescope consisting of six ALPIDE layers, should adhere to this criterion.

The beam test facility (BTF) at the Siam Research Light Institute (SLRI) served as a model for this telescope. It was employed to test the pCT development with the Proton cyclotron (Varian ProBeam Compact Therapy System), utilizing its electron detection capabilities. The telescope comprises six ALPIDE sensors, with each single chip containing 512 $\times$ 1024 pixels. The electronic readout is connected to each layer through the DAQ board. The telescope's operation is facilitated by the EUDAQv2 software, implemented using the C++ programming language. The output of the EUDAQv2 run is generated as event-by-event data in the form of a RAW binary file. Each event corresponds to a detection frame, which is defined by an external input known as the "trigger" signal. The trigger signal originates from the trigger controller system, which utilizes the MEGA2560 pro to control the SAMKOON SK-070FE HMI touchscreen and generate the trigger pulses. To ensure reliability, the trigger system was developed using the Basys3 FPGA, which provides the divided 100 MHz FPGA clock as the trigger input. The Pro Mini 328 microcontroller manages the data flow from the Python GUI to the Basys3 FPGA. The trigger frequency was set to 9.5 kHz to maximize the frame rate of the telescope operation. A dark test condition was conducted to verify the trigger signal. In the preliminary test, the proton beam energies from the KCMH sources at 70 MeV and 200 MeV were measured.

Proton therapy is a form of radiation therapy that employs a focused stream of protons to target and eliminate cancerous cells. In order to achieve an adequate dosage, the rate at which the beam delivers protons needs to be approximately 10^9 protons/s. Unfortunately, the telescope cannot detect the therapeutic beam with a high number of protons per frame. So, the acrylic collimator was used to reduce the large number of protons by eliminating the lateral dose from the Gaussian beam. The 36 cm acrylic collimator transports some proton particles through a 1 mm hole to the ALPIDE sensor in the telescope. The collimated beam is filtered by new Gaussian model to obtain only the particles that propagate along the aperture. The background and noise of sensor are measured in the dark run and they are removed by considering the cluster size of signal and the statistics of activated pixels. According to unextractable data of EUDAQv2 output, the automation which is implemented by Python programming language was used to generate multiple event data as multple .root files. The cluster size of the sources were evaluated for preparing hitmarker as prepossessing data which is used in the reconstruction algorithm. The correlations of X and Y direction on each sensor layer pair of reconstructed tracks imply the alignment of detector setup in the telescope. By optimizing the S_{max} and cone angle in the reconstructed algorithm, proton tracks were discovered by calculating the experimental data as the multiple events.

The results show that the reconstruction efficiency of the telescope demonstrates a 70% survival rate for both 70 MeV and 200 MeV of proton energy tracks. This finding holds promise for potential enhancements and future applications in the development of the pCT prototype.

REFERENCES

REFERENCES

Abelev, B. and ALICE Collaboration (2014). Technical design report for the upgrade of the alice inner tracking system. *Journal of Physics G: Nuclear and Particle Physics*, *41*(8), 087002.

Aglieri Rinella, G. (2017). The ALPIDE pixel sensor chip for the upgrade of the alice inner tracking system. *Nuclear Instruments and Methods in Physics Research Section A: Accelerators, Spectrometers, Detectors and Associated Equipment*, *845*, 583–587.

Agostinelli, S., Allison, J., Amako, K., Apostolakis, J., Araujo, H., Arce, P., Asai, M., Axen, D., Banerjee, S., Barrand, G., Behner, F., Bellagamba, L., Boudreau, J., Broglia, L., Brunengo, A., et al. (2003). Geant4—a simulation toolkit. *Nuclear Instruments and Methods in Physics Research Section A: Accelerators, Spectrometers, Detectors and Associated Equipment*, *506*(3), 250–303.

ALICE Collaboration (2008). The alice experiment at the cern lhc. *Journal of Instrumentation*, *3*, S08002.

ALICE Collaboration (2012). Upgrade of the inner tracking system conceptual design report. *Technical Reports*, *CERN-LHCC*(LHCC-P-005).

ALICE Collaboration (2014). Technical design report for the upgrade of the alice inner tracking system. *Journal of Physics G: Nuclear and Particle Physics*, *41*.

Alme, J., Barnaföldi, G., Barthel, R., Borshchov, V., Bodova, T., Brink, A., Brons, S., Chaar, M., Eikeland, V., Feofilov, G., Genov, G., Grimstad, S., Grøttvik, O., Helstrup, H., Herland, A., et al. (2020). A high-granularity digital tracking calorimeter optimized for proton CT. *Frontiers in Physics*, *8*, 460.

Aplin, S., Engels, J., Gaede, F., Graf, N., Johnson, T., and McCormick, J. (2012). LCIO: A persistency framework and event data model for HEP. *2012 IEEE Nuclear Science Symposium and Medical Imaging Conference Record (NSS/MIC)*, 2075–2079.

Bethe, H. (1930). Zur theorie des durchgangs schneller korpuskularstrahlen durch materie. *Annalen der Physik*, *397*(3), 325–400.

Bloch, F. (1933). Zur bremsung rasch bewegter teilchen beim durchgang durch materie. *Annalen der Physik*, *408*(3), 285–320.

Bohr, N. (1915). Lx. on the decrease of velocity of swiftly moving electrified particles in passing through matter. *Philosophical Magazine Series 1*, *30*(178), 581–612.

Box, G. E. P. and Muller, M. E. (1958). A Note on the Generation of Random Normal Deviates. *The Annals of Mathematical Statistics*, *29*(2), 610–611.

Braccini, S., Ereditato, A., Kreslo, I., Moser, U., Pistillo, C., Studer, S., Scampoli, P., Coray, A., and Pedroni, E. (2010). First results on proton radiography with nuclear emulsion detectors. *Journal of Instrumentation*, *5*(09), P09001.

Bragg, W. H. and Kleeman, R. (1905). On the α particles of radium, and their loss of range in passing through various atoms and molecules. *Philosophical Magazine Series 1*, *10*(57), 318–340.

Britannica The Editors of Encyclopaedia (2024). Cyclotron. *Encyclopedia Britannica*, https://www.britannica.com/technology/cyclotron.

Brun, R. and Rademakers, F. (1997). ROOT–An object oriented data analysis framework. *Nuclear Instruments and Methods in Physics Research Section A: Accelerators, Spectrometers, Detectors and Associated Equipment*, *389*(1), 81–86.

CMS (2010). Measurement of tracking efficiency. *CMS Physics Analysis Summary - preliminary results*, *CMS-PAS-TRK-10-002*(CMS-PAS-TRK-10-002).

Cormack, A. M. and Koehler, A. M. (1976). Quantitative proton tomography: preliminary experiments. *Physics in Medicine & Biology*, *21*(4), 560.

Cussans, D. (2009). Description of the jra1 trigger logic unit (TLU), v0.2c. *EUDET-Memo-2007-02*.

Dannheim, D., Dort, K., Huth, L., Hynds, D., Kremastiotis, I., Kröger, J., Munker, M., Pitters, F., Schütze, P., Spannagel, S., Vanat, T., and Williams, M. (2021). Corryvreckan: a modular 4D track reconstruction and analysis software for test beam data. *Journal of Instrumentation*, *16*(3), P03008.

Dorokhov, A., Bertolone, G., Baudot, J., Colledani, C., Claus, G., Degerli, Y., Masi, R. D., Deveaux, M., Dozière, G., Dulinski, W., Gélin, M., Goffe, M., Himmi, A., Hu-Guo, C., and Jaaskelainen, K. (2011). High resistivity cmos pixel sensors and their application to the star pxl detector. *Nuclear Instruments and Methods in Physics Research Section A: Accelerators, Spectrometers, Detectors and Associated Equipment*, *650*(1), 174–177.

Durante, M. and Stöcker, H. (2012). Relativistic protons for image-guided stereotactic radiosurgery. *Journal of Physics: Conference Series*, *373*(1), 012016.

Giacometti, V., Bashkirov, V. A., Piersimoni, P., Guatelli, S., Plautz, T. E., Sadrozinski, H. F.-W., Johnson, R. P., Zatserklyaniy, A., Tessonnier, T., Parodi, K., Rosenfeld, A. B., and Schulte, R. W. (2017). Software platform for simulation of a prototype proton ct scanner. *Medical Physics*, *44*(3), 1002–1016.

Gottschalk, B. (2010). On the scattering power of radiotherapy protons. *Medical physics*, *37*, 352–367.

Greiner, L., Anderssen, E., Matis, H., Ritter, H., Schambach, J., Silber, J., Stezelberger, T., Sun, X., Szelezniak, M., Thomas, J., et al. (2011). A maps based vertex detector for the STAR experiment at RHIC. *Nuclear Instruments and Methods in Physics Research Section A: Accelerators, Spectrometers, Detectors and Associated Equipment*, *650*(1), 68–72.

Haas, T. (2006). A pixel telescope for detector R&D for an international linear collider. *Nuclear Instruments and Methods in Physics Research Section A: Accelerators, Spectrometers, Detectors and Associated Equipment*, *569*(1), 53–56.

Hanson, K. (1979). Proton computed tomography. *IEEE Transactions on Nuclear Science*, *26*, 1635–1640.

Hanson, K. M., Bradbury, J. N., Cannon, T. M., Hutson, R. L., Laubacher, D. B., Macek, R. J., Paciotti, M. A., and Taylor, C. A. (1981). Computed tomography using proton energy loss. *Physics in Medicine & Biology*, *26*(6), 965.

Hanson, K. M., Bradbury, J. N., Koeppe, R. A., Macek, R. J., Machen, D. R., Morgado, R., Paciotti, M. A., Sandford, S. A., and Steward, V. W. (1982). Proton computed tomography of human specimens. *Physics in Medicine & Biology*, *27*(1), 25.

Highland, V. L. (1975). Some practical remarks on multiple scattering. *Nuclear Instruments and Methods*, *129*(2), 497–499.

Hong, L., Goitein, M., Bucciolini, M., Comiskey, R., Gottschalk, B., Rosenthal, S., Serago, C., and Urie, M. (1996). A pencil beam algorithm for proton dose calculations. *Physics in Medicine & Biology*, *41*(8), 1305.

Hu-Guo, C., Baudot, J., Bertolone, G., Besson, A., Brogna, A., Colledani, C., Claus, G., De Masi, R., Degerli, Y., Dorokhov, A., Doziere, G., Dulinski, W., Fang, X., Gelin, M., Goffe, M., et al. (2010). First reticule size maps with digital output and integrated zero suppression for the eudet-jra1 beam telescope. *Nuclear Instruments and Methods in Physics Research Section A: Accelerators, Spectrometers, Detectors and Associated Equipment*, *623*(1), 480–482.

International Commission on Radiation Units and Measurements (1993). Stopping powers and ranges for protons and alpha particles. *International Commission on Radiation Units and Measurements*, *ICRU-49*(TRN:94), 014557.

Jan, S., Santin, G., Strul, D., Staelens, S., Assié, K., Autret, D., Avner, S., Barbier, R., Bardiès, M., Bloomfield, P. M., Brasse, D., Breton, V., Bruyndonckx, P., Buvat, I., Chatziioannou, A. F., et al. (2004). GATE: a simulation toolkit for PET and SPECT. *Physics in Medicine & Biology*, *49*(19), 4543–4561.

Jansen, H., Spannagel, S., Bulgheroni, A., Claus, G., Corrin, E., Cussans, D., Dreyling-Eschweiler, J., Eckstein, D., Eichhorn, T., Goffe, M., Gregor, I., Haas, D., Muhl, C., Perrey, H., Peschke, R., and others. (2016). Performance of the EUDET-type beam telescopes. *EPJ Techniques and Instrumentation*, *3*, 1–20.

Kaewjai, J., Kobdaj, C., and Kittimanapun, K. (2019). Upgrade of pixel sensor telescope for the characterization of ALPIDE sensor. *Journal of Physics: Conference Series*, 1380(1), 012126.

Kittimanapun, K., Chanlek, N., Juntong, N., Cheedket, S., Klysubun, P., Krainara, S., Sittisard, K., and Supajeerapan, S. (2017). Improvement of electron intensity reduction system at SLRI beam test facility. *International Particle Accelerator Conference*, 528.

Koch, N. C. and Newhauser, W. D. (2010). Development and verification of an analytical algorithm to predict absorbed dose distributions in ocular proton therapy using monte carlo simulations. *Physics in Medicine & Biology*, *55*(3), 833.

Kofarago, M. (2015). Upgrade of the inner tracking system of alice. *Proceeding of science*, *VERTEX2015*, 009.

Landau, L. D. (1944). On the energy loss of fast particles by ionization. *Journal of physics*, *8*, 201–205.

Leo, W. R. (1994). Techniques for nuclear and particle physics experiments: a how-to approach. *Springer*, https://books.google.co.th/books?id=W7vHQgAACAAJ.

Leo, W. R. and Haase, D. G. (1990). Techniques for nuclear and particle physics experiments. *American Journal of Physics*, *58*(01), 1216–1217.

Li, T., Liang, Z., Singanallur, J., Satogata, T., Williams, D., and Schulte, R. (2006). Reconstruction for proton computed tomography by tracing proton trajectories: A monte carlo study. *Medical physics*, *33*, 699–706.

Mager, M. (2016). ALPIDE, the monolithic active pixel sensor for the ALICE ITS upgrade. *Nuclear Instruments and Methods in Physics Research Section A: Accelerators, Spectrometers, Detectors and Associated Equipment*, 824, 434–438.

Mager, M. and ALICE Collaboration (2022). Noise performance of the ALPIDE-based ALICE inner tracking system. *Journal of Physics Conference Series*, *2374*, 012062.

Maxim, V., Frandeş, M., and Prost, R. (2009). Analytical inversion of the compton transform using the full set of available projections. *Inverse Problems*, *25*(9), 095001.

McKinney, W. (2010). Data structures for statistical computing in python. *SciPy*, *445*, 56–61.

Naimuddin, M., Coutrakon, G., Blazey, G., Boi, S., Dyshkant, A., Erdelyi, B., Hedin, D., Johnson, E., Krider, J., Rukalin, V., Uzunyan, S., Zutshi, V., Fordt, R., Sellberg, G., Rauch, J., et al. (2016). Development of a proton computed tomography detector system. *Journal of Instrumentation*, *11*(02), C02012.

Newhauser, W. D. and Zhang, R. (2015). The physics of proton therapy. *Physics in Medicine & Biology*, *60*(8), R155.

Pedroni, E., Scheib, S., Böhringer, T., Coray, A., Grossmann, M., Lin, S., and Lomax, A. (2005). Experimental characterization and physical modelling of the dose distribution of scanned proton pencil beams. *Physics in Medicine & Biology*, *5*(3), 541.

Pettersen, H. E. S., Meric, I., Odland, O. H., Shafiee, H., Sølie, J. R., and Röhrich, D. (2020). Proton tracking algorithm in a pixel-based range telescope for proton computed tomography. *arXiv preprint arXiv:2006*, 09751.

Poludniowski, G., Allinson, N. M., Anaxagoras, T., Esposito, M., Green, S., Manolopoulos, S., Nieto-Camero, J., Parker, D. J., Price, T., and Evans, P. M. (2014). Proton-counting radiography for proton therapy: a proof of principle using CMOS APS technology. *Physics in Medicine & Biology*, *59*, 2569–2581.

Presti, D. L., Bonanno, D., Longhitano, F., Pugliatti, C., Aiello, S., Cirrone, G. A. P., Giordano, V., Leonora, E., Randazzo, N., Romano, F., Russo, G. V., Sipala, V., Stancampiano, C., and Ventura, C. (2014). A real-time, large area, high space resolution particle radiography system. *Journal of Instrumentation*, *9*(06), C06012.

Sadrozinski, H.-W., Johnson, R., Macafee, S., Plumb, A., Steinberg, D., Zatserklyaniy, A., Bashkirov, V., Hurley, R., and Schulte, R. (2013). Development of a head scanner for proton CT. *Nuclear Instruments and Methods in Physics Research Section A: Accelerators, Spectrometers, Detectors and Associated Equipment*, *699*, 205–210.

Saraya, Y., Izumikawa, T., Goto, J., Kawasaki, T., and Kimura, T. (2014). Study of spatial resolution of proton computed tomography using a silicon strip detector. *Nuclear Instruments and Methods in Physics Research Section A: Accelerators, Spectrometers, Detectors and Associated Equipment*, *735*, 485–489.

Satz, H. (2011). The quark-gluon plasma: A short introduction. *Nuclear Physics A*, *A862-863*(BI-TP-2011-02), 4–12.

Scaringella, M., Bruzzi, M., Bucciolini, M., Carpinelli, M., Cirrone, G. A. P., Civinini, C., Cuttone, G., Presti, D. L., Pallotta, S., Pugliatti, C., Randazzo, N., Romano, F., Sipala, V., Stancampiano, C., Talamonti, C., et al. (2014). A proton computed tomography based medical imaging system. *Journal of Instrumentation*, *9*(12), C12009.

Schaffner, B. (2008). Proton dose calculation based on in-air fluence measurements. *Physics in Medicine & Biology*, *53*(6), 1545.

Schambach, J., Anderssen, E., Contin, G., Greiner, L., Silber, J., Stezelberger, T., Sun, X., Szelezniak, M., Videbaek, F., Vu, C., et al. (2015). A MAPS based micro-vertex detector for the STAR experiment. *Physics Procedia*, *66*, 514–519.

Schneider, U. and Pedroni, E. (1994). Multiple coulomb scattering and spatial resolution in proton radiography. *Medical Physics*, *21*(11), 1657-1663.

Schneider, U., Pedroni, E., and Lomax, A. (1996). The calibration of ct hounsfield units for radiotherapy treatment planning. *Physics in Medicine & Biology*, *41*(1), 11.

Schulte, R., Bashkirov, V., Klock, M., Li, T., Wroe, A., Evseev, I., C Williams, D., and Satogata, T. (2005a). Density resolution of proton computed tomography. *American Association of Physicists in Medicine*, *32*, 1035–1046.

Schulte, R., Bashkirov, V., Li, T., Liang, Z., Mueller, K., Heimann, J., Johnson, L., Keeney, B., Sadrozinski, H.-W., Seiden, A., Williams, D., Zhang, L., Li, Z., Peggs, S., Satogata, T., et al. (2004). Conceptual design of a proton computed tomography system for applications in proton radiation therapy. *IEEE Transactions on Nuclear Science*, *51*(3), 866–872.

Schulte, R. W., Bashkirov, V., Loss Klock, M. C., Li, T., Wroe, A. J., Evseev, I., Williams, D. C., and Satogata, T. (2005b). Density resolution of proton computed tomography. *Medical Physics*, *32*(4), 1035–1046.

Schulte, R. W., Penfold, S. N., Tafas, J. T., and Schubert, K. E. (2008). A maximum likelihood proton path formalism for application in proton computed tomography. *Medical Physics*, *35*(11), 4849–4856.

Spannagel, S. (2016). Test beam measurements for the upgrade of the cms pixel detector and measurement of the top quark mass from differential cross sections. *Doctoral dissertation (DESY)*, *CMS-TS-2016-010*(CERN-THESIS-2016-059), 275.

Strandlie, A. and Frühwirth, R. (2010). Track and vertex reconstruction: From classical to adaptive methods. *Reviews of modern physics*, *82*(2), 1419.

Taylor, J., Allport, P., Casse, G., Smith, N., Tsurin, I., Allinson, N., Esposito, M., Kacperek, A., Nieto-Camero, J., Price, T., et al. (2015). Proton tracking for medical imaging and dosimetry. *Journal of Instrumentation*, *10*(02), C02015.

Uzunyan, S. A., Blazey, G., Boi, S., Coutrakon, G., Dyshkant, A., Erdelyi, B., Hedin, D., Johnson, E., Krider, J., Rykalin, V., Zutshi, V., Ford, R., Sellberg, G., Rauch, J. . E., Roman, M., et al. (2016). A new proton CT scanner. *arXiv:1409*, 0049.

Vavilov, P. (1957). Ionization losses of high-energy heavy particles. *Journal of Experimental and Theoretical Physics*, *5*.

Weber, Uli, Kraft, and Gerhard (2009). Comparison of carbon ions versus protons. *The Cancer Journal: The Journal of Principles & Practice of Oncology*, *15*, 325–32.

Williams, D. C. (2004). The most likely path of an energetic charged particle through a uniform medium. *Physics in Medicine & Biology*, *49*(13), 2899.

Xilinx (2017). Basys 3 reference manual. https://digilent.com/reference/programmable-logic/basys-3/reference-manual.

Yang, C., Feng, C., Liu, J., Teng, Y., Liu, S., An, Q., Sun, X., and Yang, P. (2019). A prototype readout system for the ALPIDE pixel sensor. *IEEE Transactions on Nuclear Science*, *66*(7), 1088–1094.

Zygmanski, P., Gall, K. P., Rabin, M. S. Z., and Rosenthal, S. J. (2000). The measurement of proton stopping power using proton-cone-beam computed tomography. *Physics in Medicine & Biology*, *45*(2), 511.

CURRICULUM VITAE

Name : Mr. Arnon Songmoolnak

Date of Birth : April 11, 1993

Place of Birth : Khon Kaen, Thailand

Education :

2012 - 2016 Bachelor of Science, Department of Physics, Faculty of Science, Khon Kaen university, Thailand

2016 - 2023 Doctor of Philosophy, School of Physics, Institute of Science, Suranaree University of Technology, Thailand

Publications :

1. Alme, J., Barnaföldi, G. G., Richter, M., Röhrich, D., Samnøy, A. T., Barthel, R., Borshchov, V., Bodova, T., van den Brink, A., Brons, S., Chinorat, K., Setterdahl, L., Shafiee, H., Skjolddal, Ø. J., **Songmoolnak, A.**, et al. (2020) A High-Granularity Digital Tracking Calorimeter Optimized for Proton CT. *Frontiers in Physics* (published)

2. Pettersen, H. E. S., Volz, L., Sølie, J.R., Alme, J., Barnaföldi, G.G., Barthel, R., van den Brink, A., Borshchov, V., Chaar, M., Eikeland, V., Genov, G., Grøttvik O., Kobdaj, C., **Songmoolnak, A.**, Röhrich, D., et al. (2021) Helium radiography with a digital tracking calorimeter—a Monte Carlo study for secondary track rejection. *Physics in Medicine & Biology* (published)

3. Pettersen, H. E. S., Aehle, M., Alme, J., Barnaföldi, G. G., Borshchov, V., van den Brink, A., Chaar, M., Eikeland, V., Feofilov, G., Garth, C., Gauger, R. N., Genov, G., Kobdaj, C., **Songmoolnak, A.**, Röhrich, D., et al. (2021) Investigating particle track topology for range telescopes in particle radiography using convolutional neural networks. *Acta Oncologica* (published)